The Dynamics of Ultra-Thin Polymer Films in Different Confinements Studied by Resonance Enhanced Dynamic Light Scattering

Dissertation

zur Erlangung des Grades

“Doktor der Naturwissenschaften”

im Promotionsfach Physikalische Chemie

am Fachbereich Chemie, Pharmazie und Geowissenschaften

der Johannes Gutenberg-Universität Mainz

Fan-Yen Lin

geboren in Yi-Lan, Taiwan

Mainz, April 2015

Abstract

The controversy about the glass transition on the nanoscale, e.g., the glass transition temperature (T_g) of polymer thin films, is not fully resolved. The nanoscale dynamic behavior is strongly affected by the boundary conditions of the samples. Polymer thin films are ideal systems to study the dynamics of polymer chains under different confinements, which I varied in this thesis to gain more and better insight into this problem.

Resonance Enhanced Dynamic Light Scattering (REDLS) is a marker-free method and used to investigate the dynamics of polymer thin film of which the dynamics of capillary wave is the most prominent. Via the coupling of these to the mechanical properties of the film, e.g. the dynamics of hidden layers, the confinement effects from the substrate can be studied.

Therefore, dynamics of thin, liquid polybutadiene (PB) films on solid substrates have been studied at temperatures far above the glass transition temperature T_g. The capillary wave dynamics are the stronger suppressed by the substrate, the thinner the film is. We find a molecular weight independent film thickness below which the dynamics change dramatically – the viscosity increases by orders of magnitude. This change is not related to $3R_g$ as postulated in theory and claimed in some experimental findings, but rather to a fixed distance from the polymer/glass interface. Part of our observations we attribute to a compared to bulk polymer less mobile viscoelastic layer near the substrate, and part to a more mobile layer at the liquid- gas interface. Thus, the overall behavior of the dynamics can be explained by a "three layer" model, the third layer having bulk behavior in between the above two layers.

Second, polystyrene/polynorbornene (PS/PN) bilayers are measured at temperatures close to T_g to observe the capillary wave of PS at the interface of PS/ PN. Because the capillary wave of PS is strongly suppressed by the glassy PN layer, other modes of dynamic behavior are accessible; they are vanishing in the noise, i.e. they are much smaller than the noise of the strong capillary mode. The strongly suppressed capillary wave and a new mode found show Arrhenius, i.e. thermally activated behavior above T_g which is an indication for strongly localized processes or dynamical modes.

Third, the PS thin film is anchored to Au by thiol group in order to enhance the confinement from the substrate. This creates artificially a less mobile layer and we gained insight into the role of such a layer. In addition to the capillary wave, there is a local motion found existing at the surface of PS thin film. Since the enhanced confinement from the substrate, the thickness of so-called less mobile layer near the substrate is enlarged and makes the viscosity of the PS thin film higher the bulk by half an order of magnitude. In my thesis I have shown how changing confinement can influence the dynamics of polymer thin films.

Zusammenfassung

Die Kontroverse über den Glasübergang im Nanometerbereich, z. B. die Glasübergangstemperatur T_g von dünnen Polymerfilmen, ist nicht vollständig abgeschlossen. Das dynamische Verhalten auf der Nanoskala ist stark von den einschränkenden Bedingungen abhängig, die auf die Probe wirken. Dünne Polymerfilme sind ideale Systeme um die Dynamik von Polymerketten unter der Einwirkung von Randbedingungen zu untersuchen, wie ich sie in dieser Arbeit variiert habe, um Einblick in dieses Problem zu erhalten.

Resonanzverstärkte dynamische Lichtstreuung ist eine Methode, frei von z.B. Fluoreszenzmarkern, die genutzt werden kann um in dünnen Polymerfilmen dynamische Phänomene , von denen Kapillarwellen die am ausgeprägtesten sind, zu untersuchen. Über die Kopplung dieser mit den mechanischen Eigenschaften des Films können Rückschlüsse auf die Dynamik des innenliegenden Polymers und die durch das Substrat hervorgerufenen Confinement-Effekte gezogen werden.

Die Dynamik von dünnen, flüssigen Polybutadien (PB) Filmen auf festen Substraten wurde bei Temperaturen weit oberhalb der Glasübergangstemperatur T_g untersucht. Je dünner der Film, umso stärker sind die Kapillarwellen unterdrückt. Es existiert jeweils eine vom Molekulargewicht unabhängige Schichtdicke, unterhalb derer sich die Dynamik dramatisch verändert - die Viskosität ist um Größenordnungen erhöht. Anders als durch die Theorie vorausgesagt, und in einigen experimentellen Befunden festgestellt, hängt diese Veränderung nicht vom dreifachen Gyrationsradius R_g ab, sondern vielmehr vom Abstand zur Substrat/Polymer-Grenzfläche. Einen Teil unserer Beobachtungen führen wir auf eine im Vergleich zum Polymer im Volumen weniger mobilen an das Substrat angrenzende viskoelastische Schicht zurück und einen weiteren Teil auf eine mobilere Schicht an der Flüssig-Gas-Grenzfläche jeweils verglichen mit der Mobilität des Volumensystems. Somit kann das dynamische Gesamtverhalten mit einem „Drei-Schichten-Modell“ erklärt werden, wobei das Volumen zwischen den obigen beiden Schichten die dritte Schicht darstellt.

Zweitens wurden Polystyrol/Polynorbornen(PS/PN)-Doppelschichten bei Temperaturen nahe T_g untersucht um die Kapillarwellen des PS an der PS/PN-Grenzfläche zu beobachten. Da die Kapillarwelle des PS stark von der glasigen PN-Schicht unterdrückt wird, sind weitere Modi der Dynamik zugänglich; sie verschwinden sonst im Rauschen der starken Kapillarwellenmode. Die stark unterdrückt Kapillarwelle und die neue Mode zeigen Arrheniusverhalten, d.h. oberhalb T_g ist das Verhalten thermisch aktiviert und weist damit auf stark lokalisierte Prozesse bzw. dynamische Moden hin.

Drittens wurden die PS-Filme mit Polymeren die als Endgruppe Thiolgruppen enhalten an der Goldschicht verankert um die Anbindung an das Substrat zu verbessern. Dies erzeugt künstlich eine weniger bewegliche Schicht die einen Einblick in die Rolle einer solchen gewährt. Neben Kapillarwellen wurde eine lokale Bewegung an der Oberfläche des PS-Film festgestellt. Durch das verstärkte Confinement durch das Substrat und die Ankermoleküle wird die Dicke der sogenannten weniger mobilen Schicht am Substrat vergrößert und die Viskosität der dünnen PS-Schicht erhöht sich im Vergleich zum Polymer im Volumen um eine halbe Größenordnung. In meiner Doktorarbeit habe ich gezeigt wie Änderungen von Confinements sich auf die Dynamik von Polymerfilmen auswirken.

Contents

Chapter 1

Introduction

The dynamics of polymer thin films contains important implications for phenomena such as lubrication, adhesion, friction, dewetting, etc.. In addition to this, the thin film dynamics is relevant for several commercial applications such as photo-resists, inks, and coatings. A fundamental question remaining unclear is, how the substrate affects the dynamics of polymer chains in the thin film at different length scales. This question is indeed of vital importance, as is clear from the fact that it has stimulated a number of theoretical [1-6] and experimental [7-15] studies. However, some controversial debates on the reduction of glass transition (T_g) are still not fully resolved. One hypothesis for the reduction of T_g has been attributed to the presence of a few nanometer thick polymer layer at the polymer-gas interface with higher mobility than the bulk polymer[16]. This, compared to bulk, more mobile layer is expected to have enhanced dynamics of the polymer-segments and to reduce the viscosity locally, thus leading to a reduced average viscosity of the whole film. In experiments not spatially resolving this layer typically the average dynamics or average viscosity of the film as a whole is observed. The existence of a more mobile layer was shown in experiments[12,17] using the mobility of fluorescent markers. Here this more mobile layer was followed up to temperatures a few degree above T_g; for higher temperatures it could not be resolved.

As such, it is highly required to measure the surface dynamics of a thin polymer film directly. Direct evidence like the reduction of the glass transition temperature T_g or viscosity η could be used to prove the presence of a more mobile layer. Moreover, they show how the more mobile layer and the confinement from the substrate compete to affect the dynamics of thin films.

In the following, I briefly review the controversies of this more mobile layer and the effective length scale of confinement from the substrate. Then, the theoretical models explaining the reduction of T_g are introduced.

1.1 Mobile layer at the surface

This surface dynamics is not only reflected by shear waves in the bulk, but also by surface and capillary waves[18,19]. A capillary wave model was developed by Jäckle[20] to interpret how viscoelastic and hydrodynamic effects influence capillary waves. The effects on dynamic properties and thus the T_g of thin films of a more mobile layer at the liquid-gas interface are considered by Herminghaus[2]. From ellipsometric measurements[8], the T_g of polystyrene (PS) films was shown to be lower than the bulk value if the film thickness $h \leqq 40$ nm. The reduction of T_g was closely related to the segmental length of polymer chains[21]. A more mobile layer was claimed to exist near the surface, the thickness is supposed to be constant and of the order of 10 nm[22]. The free surface or interface plays a crucial role for the more mobile layer[23,24]. The more mobile layer was considered with the remained bulk part of thin film to form a two-layer model to explain the reduction of T_g.[25]

Atomic force microscopy (AFM)-based[10,15,26] experiments demonstrated an enhanced surface dynamics relative to the bulk in both entangled and not entangled polymer thin films. Fluorescence-based spectroscopy[9] not only showed the reduction of T_g with decreasing film thickness, but also a distribution of T_g in the thin film to confirm the prediction[1] that T_g is a local property depending on position or height in a thin film. Another fluorescence-based spectroscopy experiment[12,17] claims the existence of the more mobile layer and show that it disappears a few degree in temperature above T_g – the bulk dynamics takes over. For stepped films, via monitoring a flow with the tendency to level the steps, the existence of this more mobile layer on top of PS was shown[15]. Similar surface melting phenomena were also shown in dewetting[27] and Nuclear Magnetic Resonance (NMR) experiments[28].

On the other hand, detailed ellipsometry, broadband dielectric spectroscopy, X-ray reflectometry, alternating current, and differential scanning calorimetry experiments[11,29,30] showed the T_g difference between thin polystyrene film and the bulk not to be bigger than ±3K. Moreover, the T_g of thin film was found to be independent of the film thickness and the molecular weight (M_w), and then the existence of the more mobile layer was excluded. X-ray photon correlation spectroscopy (XPCS) experiments [7,13,14] showed the in-plane surface dynamics to be dependent on the film thickness, and affected by the substrate in different length scale. The XPCS measurements are in good agreement to the capillary wave model[2,20], they did not show any difference in viscosity between thin film and bulk polymer. However, by using Au nanoparticles as markers in the XPCS experiments[31], a lower viscosity at the surface was reported when the measuring temperature much higher than the T_g. This lower surface viscosity was attributed to the reduced entanglement at the surface.

1.2 Confinement by the Substrate

Another controversy is about the influence of the solid substrate on the conformation of the polymer and thus on the density. In multiscale molecular dynamic simulation[32,33], a change of density was observed for the case of polystyrene on gold. The case of polybutadiene (PB) on Graphite was studied by computer simulation [3,4]. Here a slow component of the dynamics adjacent to the solid substrate was found and the polymer dynamics away from the substrate was somewhat faster than bulk. Some of these simulation results on PB were compared with dielectric spectroscopy results[34] on *cis*-polyisoprene (PI) with the conclusion, the segmental relaxation in the mean relaxation rate and in its spectral width does not depend on the thickness of the polymer layer for the films thicker than 7 nm, but a 1-2 nm thick layer adjacent to the substrate can induce a shift of the peak frequency of the α-process of the glass transition. Most works[3,4,32,33,35-38] showed there was a dense layer adjacent to the substrate. Furthermore, there were density fluctuation[32,33,36], and multi-mode motions found in the dense layer[4].

From these results, the shift of T_g was attributed to the packing effects and intramolecular rotation barriers[3]. Compared to the thinner film, the mobility of polymer chains adjacent to the substrate in the thicker film was much slower than the remained bulk part[37].

A less mobile viscoelastic layer was induced by the confinement imposed by the substrate[39,40]. The thickness of this less mobile layer was more than 5 nm. The thickness of the dense layer was related to the radius of gyration (R_g) of polymer chains[14,41]. The less mobile viscoelastic layer appeared within the $3R_g$ region. The dynamics of polymer chains were also affected by the interaction between the polymer and the substrate [23,42,43]. Both of the less mobile viscoelastic layer and dense layer were induced by the confinement from the substrate. The dense layer would enhance the small percolation domains of slow dynamics due to free volume decreasing [35,44]. However, the length scale of less mobile viscoelastic layer as explained above was larger than the dense layer.

The influence of confinement was claimed to range from 3 to 14 times the size of R_g[45]. Another study claims the long-range motions of polymer chains to be suppressed by a "viscoelastic" layer[46] with hindered dynamics.

We believe there should be a more dense layer of a few nm adjacent to the substrate. Here the following questions emerge. How does the dense layer expands its influence to form the less mobile viscoelastic layer? How does the less mobile layer affect the surface dynamics of thin films? We will address these questions in the thesis.

1.3 Models for the reduction of T_g

The sliding model[1] was proposed by de Gennes to describe the more mobile layer (**FIG. 1.3.1**). In this theory, the dynamics of polymer chains is a competion by two types of motions. In the entangled and high molecular weight (M_w) polymer, there are free ends of polymer chains near the surface. When the film thickness is thinner than the size of the coil which polymer chains typically form, these free ends of polymer chains will be according to this

model out of the surface and enhance the surface dynamics to form a more mobile layer. When the film thickness is close to the bulk, the motions of free ends were hindered and decided by the free volume.

However, experiments[26,44] showed the reduction of T_g for the small M_w polymer. The reduction of T_g did not only occur at a surface as well as in the bulk of free-standing thin films[47]. This is in contradiction with the assumption of the sliding mode proposed by de Gennes[1]. Long and Lequeux[44] introduced a model based on the thermally induced density fluctuation to explain the reduction of T_g. In the bulk, the T_g is a 3 dimensional entity and is controlled by small percolation domains of slow dynamics. Considering the thin film to be a quasi-2 dimensional case, the small domains of slow dynamics are percolating at a lower temperature than the bulk T_g. When the film thickness decreases from bulk to thinner film, T_g is dominated by a transition from 3 dimensional to quasi-2 dimensional percolation domains. This transition leads to the reduction of T_g.

The model introduced by Long and Lequeux[44] shown here could be applied to any M_w of polymer, and is compatible with the sliding mode proposed by de Gennes. This sliding model and the model proposed by Long and Lequeux[44] both probably cause a reduction of T_g. This idea was supported by the experimental evidence of two separate mechanisms occurring simultaneously[48].

There are experimental results [10,12,15,17,26,49-52] reporting the multi modes of polymer chains motions observed at the same time. Above T_g, these multi modes would disappear and merge into a single mode. Mirigian and Schweizer[53] proposed a force-level model to explain the mobility gradients (**FIG. 1.3.2**). In this model, the polymer chains motions are regarded as particles moving within the neighboring particles. This model could be explained by different depth of films: (i) in the bulk part of film, particles had to overcome local barrier to hopping. (ii) Particles near the surface would be less confined due to the reduced caging constraints. And then

oscillate locally. (iii) Particles close to the substrate would be confined like the bulk. But particles would oscillate locally unlike hopping in the bulk.

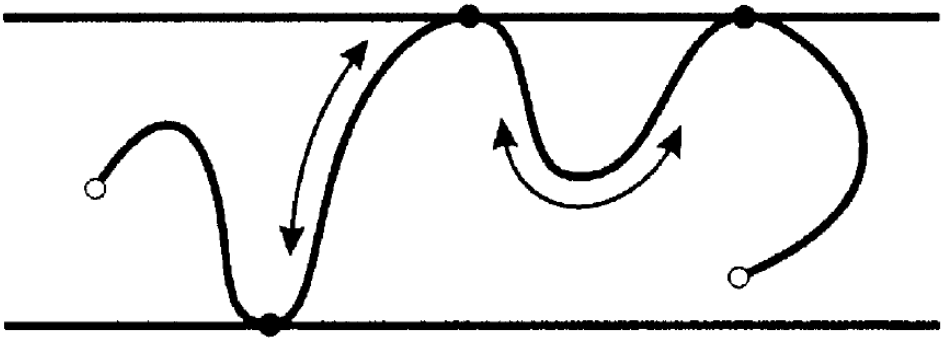

FIG. 1.3.1 The sliding model proposed by de Gennes[1] to explain the more mobile layer in the high Mw regime. Reprinted from Advances in Colloid and Interface Science, Vol. 94, James A. Forrest and Kari Dalnoki-Veress, The glass transition in thin polymer films, Pages No. 189, Copyright (2015), with permission from Elsevier.

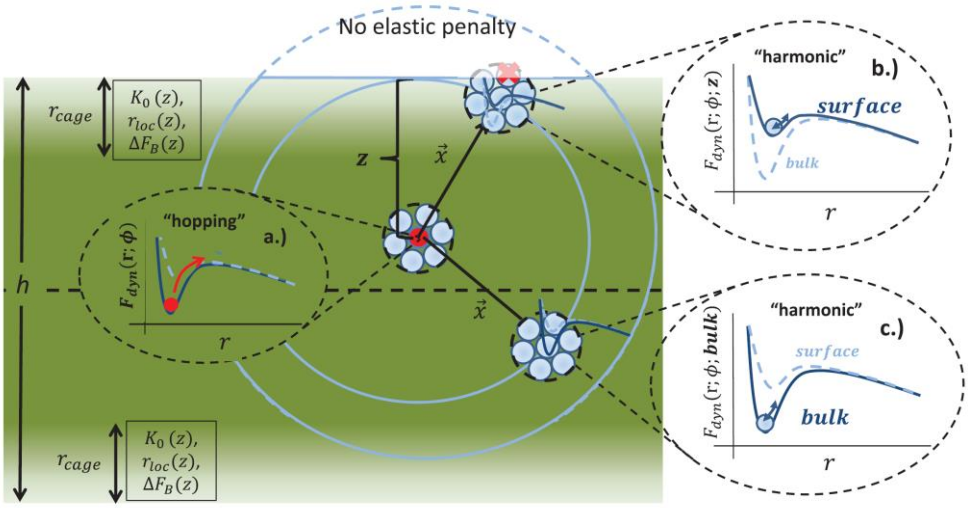

FIG. 1.3.2 The schematic shown to explain the model proposed by Mirigian and Schweizer. Here, h is film thickness, z is the distance away from the surface of film, r is particle displacement, and $F_{dyn}(r)$ is the dynamic free energy. $F_{dyn}(r)$ includes the barrier for local cage re-arrangement, Δ-F_B, transient localization length, r_{loc}, barrier location, r_B. Reprinted with permission from The Journal of Chemical Physics, Vol. 141, Stephen Mirigian and Kenneth S. Schweizer, Communication: Slow relaxation, spatial mobility gradients, and vitrification in confined films, Page No. 161103-2. Copyright [2015], AIP Publishing LLC.

1.4 Outline of the thesis

In the introduction, outlined here, there are still many contradictory experimental results to account for the reduction of T_g, and the relation between the T_g and so-called more mobile layer. The effective length scale of the confinement from the substrate gives rise to the complicated interpretation of the experimental results. So far, there were not so many choices of experimental techniques that can probe the dynamics of polymer adjacent to the substrate. Thus, the related experimental results are not so abundant.

In this thesis, we use the recently developed technique of Resonance Enhanced Dynamic Light Scattering (REDLS)[54-56] to study the motions of polymer chains in different regions of thin films by changing the probing length scale via the film thickness and the inverse probing length by changing the scattering vector. In Sulivan D.B. Vianna's PhD thesis[57], the capillary waves of PS thin films were studied close to T_g. Based on the study of these viscoelastic films (PS thin film measured close to Tg), we want to go beyond and measure the polymer thin film changing the confinement and in different elastic modulus region e.g., viscous and liquid-like thin film, and provide new insights for the nanoscale polymer dynamics.

In Chapter 2, I first give a phenomenological introduction to the liquid-glass transition. The theory of capillary wave for the phenomena we observe is introduced. The technique we used, REDLS, is a combination of the surface plasmon polariton (SPP) and dynamic light scattering (DLS) experiments. The background and experimental setups of SPP, DLS is also briefly presented.

In Chapter 3, sample preparation methods and the detailed setup and operation sequences of REDLS are introduced. All the data can be extracted from the correlation functions. Hence, the fitting methods can also be essential for interpreting the experimental results. Thus, possible fitting schemes and their applicability and variability are discussed. Since the machine, REDLS,

is custom-made, the method of estimation of the errors is quite important for the credit of data and will be shown.

In Chapter 4, the results and discussion are presented. In **Section 4.1**, the results of polybutadiene (PB) are presented. In contrast to most other studies we are not exploring a temperature range close to T_g but work at about 125K above T_g. At this measuring temperature, PB behaves like a Newtonian liquid and is used to verify the capillary wave model. We observe the confinement from substrate in different thickness of thin films. A three layer model is applied to explain the results from PB films.

In **Section 4.2**, polystyrene/polynorbornene (PS/PN) bilayers are used to observe what happens to the dynamics of capillary waves when suppressed. Other modes of the motions of polymer chains possibly present at the PS/PN interface or the PS/substrate interface are expected to be observed after the capillary wave is suppressed. The samples of PS/PN also allowed us to measure the thermal behavior for temperatures from T_g-30K to T_g+30K. The activation energy and fragility index help us to estimate the dimension of the constraint space for the motions of polymer chains under strong confinement.

In **Section 4.3**, results for polystyrene thin films anchored to Au substrate by thiol group are reported. The confinement from the substrate is enhanced and suppresses the capillary wave strongly. This system proves that there are multi-modes of motions of polymer chains existing at the polymer/air interface.

Finally, the conclusions and a perspective of future or further experiments on polymer thin film are presented in Chapter 5.

Chapter 2

Theoretical Background

In this thesis, what is explored is the dynamic properties of polymer thin films of which a mayor contribution is attributed to capillary waves. The dynamics is studied by the recently developed technique, Resonance Enhancement Dynamic Light Scattering (REDLS)[54-56]. In the setup of REDLS, surface plasmon polaritons (SPP) are adopted to be the coherent light source for a dynamic light scattering (DLS) experiment in order to measure the dynamics of capillary waves. In this chapter, I will briefly introduce the phenomenological features of the liquid-glass transition and the controversy about T_g existing for ultra-thin polymeric films. An introduction to the theory of capillary waves, and the experimental methods SPP, and DLS as basis of REDLS will be given as well.

2.1 Phenomenological introduction of the liquid-glass transition

For many organic and inorganic materials with increasing temperature the dynamics undergoes the transition from an amorphous, glass-like state to an amorphous liquid-like state. This transition is called glass transition and the temperature threshold where the glass transition occurs is called glass transition temperature (T_g).

T_g characteristics of the polymer dynamics of the bulk are thermo-dynamical discontinuities to be observed in the heat capacity and thermal expansion below and above T_g. The viscosity and relaxation time of the segmental motion of polymer chains, the α-relaxation, exhibits highly non-Arrhenius temperature dependent behavior[58] during the temperature variation (**FIG. 2.1.1**).

This non-Arrhenius thermal behavior can be described by the empirical Vogel-Fulcher-Tammann (VFT) equation [59-62]:

$$\tau = \tau_0 exp \frac{B}{(T-T_0)} \quad (2.1.1)$$

Here, τ_0, B, T_0 are the pre-exponential factor, Vogel activation energy and Vogel temperature, respectively. τ is the relaxation time of the segmental motion of polymer chains. It should be noted, that the VFT equation is mathematical identical to the WLF[63] (Williams-Landel-Ferry) equation sometimes cited in the literature.

When the temperature is far above T_g, the temperature dependent viscosity or relaxation time can cross over to show an Arrhenius behavior, i.e., the dynamics of the α-process is an only thermally activated process:

$$\tau = \tau_A exp\left(\frac{E_A}{k_B T}\right) \quad (2.1.2)$$

Here, τ_A is the parameter for the Arrhenius equation, E_A is the activation energy and k_B is Boltzmann constant.

In addition to the α-relaxation which shows non-Arrhenius behavior, there is so-called β-relaxation in the amorphous polymers. This β-relaxation shows the Arrhenius behavior (**FIG. 2.1.1**) and is referred to the localized motions of polymer chains[58,64].

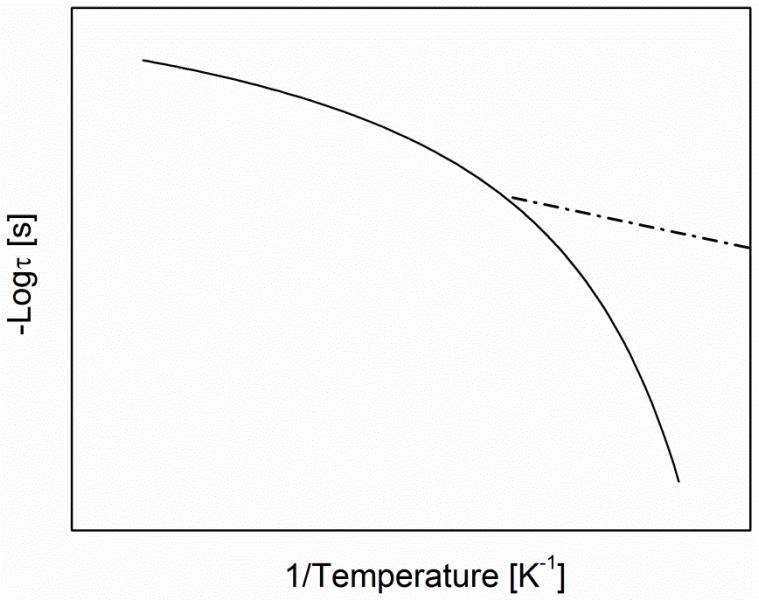

FIG. 2.1.1. Activation plot for the non-Arrhenius thermal behavior (solid line) described usually by the VFT or WLF equations for the α-relaxation and the Arrhenius thermal behavior (dash-dot line) for the so called β-relaxation.

The glass transition dynamics can be described by the idea of co-operative rearranging regions (CRR). This idea was introduced by Adam and Gibbs[65]. The CRR were defined as the number of monomeric segments moving together like a group in a specific region. The size of the CRR was found to be correlated with the so called fragility index[66,67], and the activation energy is calculated by using the Arrhenius plot[68]. In terms of the fragility concept[69,70], the glass forming materials can be classified: one extreme is the "strong" glass materials which show almost Arrhenius behavior and they are found to have a smaller size of the CRR with the variation of temperature. The other extreme is the "fragile" glass materials which show strong non-Arrhenius behavior and are referred to have a larger size of the CRR near T_g.

So far, many studies have focused on the bulk properties as described above. In contrast, little is known about the glass transition in the nanoscale under some kind of confinement and the relation between this dynamics and the bulk properties. Polymer thin films are suitable systems for us to observe the nanoscale dynamic behavior under confinement and build the connection with the bulk dynamics by changing the thin film thickness.

However, boundary effects play a crucial role in the properties of thin films and as a result they affect the thin film dynamics strongly. At substrate/polymer interfaces, confinement from the substrate can suppress the long-range motions of polymer chains[46]. At the polymer/air interface, a more mobile layer compared to bulk dynamics is found[16]. This results in the broad T_g distribution[9] shown in the thin films and fitted the prediction of theory[1] demonstrating that T_g as inferred from the dynamics of the segmental motion might not be a good reporter of dynamic length scale in the thin films in contrast to the bulk[16,71].

Recently, Forrest and Dalnoki-Veress[71] showed that typical dilatometric measurement of the glass transition thus not necessarily show a real glass transition by using a model calculation based on the so-called rheological temperature[72] The rheological temperature was defined as a temperature which exhibits the same dynamics as the bulk. For example, let's think about the polymer film which exhibits the dynamics of the mobile layer at 326 K being the same as the bulk dynamics at 356 K. Then, the rheological temperature of the more mobile layer was defined as 356K. The rheological temperature is assumed to vary with the depth of the thin films. At the polymer/air interface, there was a more mobile layer and its rheological temperature has the highest value across the thin film. The rheological temperature was close to the bulk temperature when the point of measurement in the polymer thin film is close to the substrate. Moreover, they also assumed a temperature dependent length scale $\xi(T)$ is defined as the length scale to exhibit a transition from surface-like to bulk-like. This $\xi(T)$ is related to the CRR shown in the glass transition of bulk. Both, the rheological temperature and $\xi(T)$ were used to build a model to simulate the reduction of T_g with decreasing film thickness. They found that the dilatometric T_g did not couple with the dynamics of polymer chains in the thin films. This indicates that the dilatometric T_g of the thin film was not a good indicator to report the glass transition in the thin film. We have to find a more direct method to characterize a T_g which corresponds to the nanoscale dynamics in the future.

2.2 Capillary waves

In the last century, the liquid surfaces have attracted tremendous interests[73]. As surface waves, capillary waves were first predicted by Smoluchowski in 1908[74]. Thermally activated capillary waves were applied by Mandelstam[75] to describe the interface roughness. Levich and Krylov[76] indicated the capillary wave may occur when the surface tension varies locally on the surface, so-called surface tension fluctuation.

When the temperature of a polymer thin film is higher than T_g, the thin film can be thought of as a general liquid on top of a substrate[39]. This cooperative motion induces the local density fluctuation. That means the molecules in a liquid will not disperse uniformly.

When molecules are at the liquid/air interface, one side is other liquid molecules as neighbors, and the other side is gas. The force acting on the molecules at the liquid/air interface is not as balanced as in bulk. Thus, this will create density fluctuations which will induce waves at the liquid/air interface to re-distribute the molecules to minimize the surface energy (**FIG. 2.2.1**).

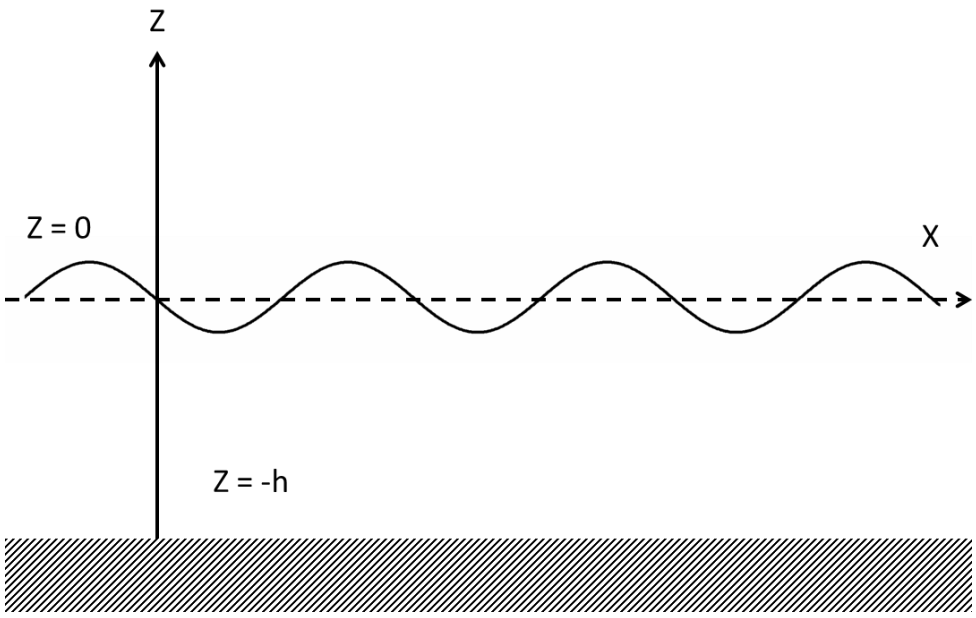

FIG. 2.2.1. Schematics for a thermally activated capillary wave of a thin film of thickness h on a solid substrate. The position of the capillary wave in the z-axis is 0, and propagates along the x-axis. The substrate locates at–h in the z-direction.

Capillary waves prevent the surface of liquids from being extremely flat, and thus are one source for it to have a certain roughness. The liquid surface can be described by the height fluctuation induced by the thermally activated capillary wave. Capillary waves are strongly affected by the boundary condition e.g., the confinement from the substrate for thin films. Capillary waves are influenced by the substrate effect with changing liquid film thickness. Thus, the capillary wave was found to be more suitable than van der Waals's theory to describe the surface structures[77]. This height fluctuation was discussed more detailed in the literatures[19,78].

Based on the height fluctuation, capillary waves have been observed by diffuse x-ray scattering and reflectivity to measure surface roughness of liquids [79-83]. These measurements of surface roughness are time averaged and cannot supply dynamic information of capillary waves. However, it is possible e.g., to monitor the height variation with time evolution by XPCS, and apply height-height correlation functions to probe the dynamics of capillary wave [7,84-88].

Jäckle[20] proposed the first general formula to describe the spectrum of surface waves on viscoelastic liquids of arbitrary depth. Jäckle discussed the spectrum of surface waves in different limiting cases. For shallow liquids, the lubrication approximation[89] was used to solve the Navier-Stokes equation. One has to note, contributions from the elastic high-frequency waves are missing by using the lubrication approximation.

Herminghaus[2], based on the idea of a polymer freezing or melting due to memory effects, proposed another model to describe the capillary wave, and showed how a free surface or mobile interface affects the strain relaxation behavior in a viscoelastic material.

Next, the memory effect from this work will be briefly introduced. Due to strain the polymer coil can deform into e.g. ellipsoidal form. The polymer chains tend to go back to the form of Gaussian coil if they are annealed over their characteristic reptation time. This process, how a Gaussian coil relaxes to the final stretched state of polymer chains which are spin-coated on the substrate and after annealing is called memory effect[2].

The results by Jäckle and Herminghaus are similar. We give here the derivation by Herminghaus[2].

The strain of the final stretched state is described by a tensor field, S(r). The strain of polymer chains is relaxed when the temperature is high enough. This relaxation may proceed by the diffusion within the individual polymer coil which is shown as:

$$\partial_t S = -\omega_0 S \tag{2.2.1}$$

Here, the ∂_t is the time derivative, and ω_0 is the slowest Rouse relaxation rate[90,91]. Note that this Rouse relaxation rate is much slower than the α-relaxation. Only a single relaxation rate is considered here for simplifying the problem. Besides, S(r) may decay by rearranging the polymer chains and moving the center-of-mass of the polymer coils. The decay of S(r) may arise from the fluctuation of the polymer coil motions as well as the flow of the polymer chains in the melt.

The interfacial eigenmode spectrum of the viscoelastic polymer melt is considered[5]. This spectrum can be applied to all the possible boundary conditions such as slipping, free-standing, and free surface can be discussed within the same framework. The discussion is restricted to one in-plane (x) and one out-of-plane (z) axes (**FIG. 2.2.1**). The vector potential is defined as $\phi = (\phi_x, \phi_z)$ for the strain tensor which is related to the latter via:

$$S =: \begin{pmatrix} \partial_x \phi_x & \frac{1}{2}(\partial_x \phi_x + \partial_z \phi_x) \\ \frac{1}{2}(\partial_x \phi_z + \partial_z \phi_x) & \partial_z \phi_z \end{pmatrix} \tag{2.2.2}$$

Here, ∂_x and ∂_z represent the partial derivative with respect to the variable x and z, respectively. The flow field, j, is coupled to ϕ by

$$\partial_x \phi = -\omega_0 \phi + j \tag{2.2.3}$$

Since we focus on the thermally activated capillary wave, the discussions can be restricted to small amplitudes. Thus, the nonlinear term $-j\nabla\phi$ is neglected, and only linear terms are kept.

The capillary wave is dominated by the viscous force. In the limit of low Reynolds number (viscous force dominant) and combining the theory of elasticity[92] and hydrodynamics[93], the force balance can be written as:

$$\eta \Delta \mathrm{j} = \nabla \mathrm{p} - \frac{E}{2(1-\psi)} \Delta \phi \tag{2.2.4}$$

Here, E is Young's modulus, ψ is Poisson's ratio, p is the pressure field, and η is the viscosity. In the following, the melt will be assumed to be incompressible: $\psi = 0.5$. The density fluctuations are neglected, and the only relevant fluctuations are those of strain. Combining **Eq. 2.2.1** and **2.2.3**, the motions can be expressed by the equation:

$$\left\{\partial_t + \omega_0 + \frac{E}{\eta}\right\} \Delta \phi = \frac{\nabla p}{\eta} \tag{2.2.5}$$

For supported films, the free surface is defined at z = 0 and the substrate is defined at z = -h (**FIG. 2.2.1**). The harmonic solution of **Eq. 2.2.5** is

$$\phi = \begin{pmatrix} f(z) \\ g(z) \end{pmatrix} \cdot exp(iqx - \omega t) \tag{2.2.6}$$

At the free surface, there is no tangential stress$\left(f^{'}(0) = 0\right)$, and gets

$$g(z) = (1 - \alpha qz)e^{qz} + (2\alpha - 2\beta - 1 - \beta qz)e^{-qz} \tag{2.2.7}$$

Here, α and β are the wave number, q, and film thickness, h, dependent. Because of the mass conservation, $f(z) = ig'(z)/q$.

At the substrate, the force balance needs

$$[(\omega_0 - \omega)\eta + E]f^{'}(-h) = (\omega_0 - \omega)\kappa f(-h) \tag{2.2.8}$$

Here, κ is the coefficient of sliding friction at the substrate. A generalized form of the extrapolation length is given by[94].

$$L = \frac{2\eta}{\kappa} - \frac{2E}{(\omega - \omega_0)\kappa} \tag{2.2.9}$$

The boundary condition of substrate is set as $g(-h) = 0$. Then,

$$2\alpha = \frac{e^{2qh}-2qh+3+Lqh\left(e^{2qh}-1\right)}{e^{2qh}+(qh-1)^2+Lqh\left(e^{2qh}+qh-1\right)} \tag{2.2.10}$$

and

$$\beta = \left(\frac{\alpha[qh(L+2)-1]+2}{Lqh+1}\right)e^{-2qh} \tag{2.2.11}$$

If there is no friction at the substrate (κ = 0), slip boundary condition, $\beta = \alpha exp(-2qh)$ is shown, and

$$\alpha(q) = \left(\frac{1}{2}\right)\frac{e^{2qh}-1}{e^{2qh}+qh-1} \tag{2.2.12}$$

These modes are the same as the symmetric modes of free-standing films, with h is half of the film thickness. On the other side, if the polymer sticks to the substrate, e.g. non-slip boundary condition, $f(-h) = 0$, then $\beta = [\alpha(2qh-1)+2]exp(-2qh)$ and

$$\alpha(q) = \left(\frac{1}{2}\right)\frac{e^{2qh}-2qh+3}{e^{2qh}+(qh-1)^2} \tag{2.2.13}$$

In order to obtain the mode spectrum, the additional boundary condition $p = -\gamma\partial_{xx}\xi(x,t)$ is set at the free surface. Here, $\xi(x,t)$ is the excursion of the latter, and γ is the surface tension. Then,

$$2\omega(q) = \omega_0 + \frac{E}{\eta} + \frac{\gamma qF(qh)}{\eta}$$

$$\pm\sqrt{\left(\omega_0 + \frac{E}{\eta} + \frac{\gamma qF(qh)}{\eta}\right)^2 - 4\omega_0\frac{\gamma qF(qh)}{\eta}} \tag{2.2.14}$$

Here, $(qh) = \frac{\alpha-\beta}{\alpha+\beta}$, when $\omega_0 \ll \omega(q)$ for all q,

the relation of **Eq. 2.2.14** can be recast as

$$\omega(q) = \omega_0 + \frac{E}{\eta} + \frac{\gamma qF(qh)}{\eta} \tag{2.2.15}$$

Note that the modes with the frequencies of $\omega(q) < \omega_0$ for all q have not been considered here.

A capillary wave is defined by its wave vector k and complex frequency $f = \omega_p + i\Gamma$ [95]. Here, the real part of the complex frequency, ω_p, represents the propagation frequency, while the imaginary part, $i\Gamma$, represents the decay of the capillary wave with the relaxation time of Γ. Γ can also be considered as the inverse of mean relaxation time, τ. The time evolution of the capillary wave depends on the surface tension γ, the viscosity η, and the density ρ of the liquid. The capillary wave shows over-damped behavior, when the ratio of ω_p/Γ becomes zero.

In a DLS experiment capillary waves can be observed in the correlation function in PCS or in the power spectrum in e.g. Fabry-Perot interferometry (results from both experiments are coupled via Fourier transform). In REDLS the time-correlation function g (q,τ) is shown as a combination of heterodyne g_1 and homodyne g_2 terms[95] and

$$g(q,\tau) = A_0 \cdot g_1(q,t) + B_0 \cdot g_2(q,t) + C_0 \qquad (2.2.16)$$

Here, A_0, B_0, and C_0 are q-dependent (but time-independent) functions[88]. In REDLS, the local oscillator is stronger than the scattered light signal, so the heterodyne term g_1 in **Eq. 2.2.16** is the dominant signal. Then

$$g(q,\tau) = g_1(q,\tau) \qquad (2.2.17a)$$

$$g_1(q,\tau) = exp(-\Gamma t)cos(\omega t) \qquad (2.2.17b)$$

When the capillary wave shows propagation behavior, the time-correlation function will show an oscillating behavior. Hence, when the frequency ω is over zero, the corresponding power spectrum $S(q,\omega)$ demonstrates two peaks at ω with a Lorentzian line shape which are away from the original incident light frequency[96]. The half width at half maximum (HWHM) is Γ. This characteristic propagation wave property is also predicted by Jäckle[20] (**FIG. 2.2.2**).

When the viscosity of a polymer thin film is high, the propagation of capillary waves can be over-damped. In the over-damped situation, the capillary wave shows a single exponential decay without oscillating term in the time-correlation functions. That is the frequency ω will become

zero in the $g_1(q,\tau)$ (**Eq. 2.2.17b**). This represents that there is a single Lorentzian peak centered at the incident light frequency close to the quasi-elastic scattering region[20].

The capillary wave model in the high viscosity regime[41] can be demonstrated as

$$\frac{1}{\tau(q_\parallel)} \cong \frac{1}{\tau_0(q_\parallel)} + \frac{\mu}{\eta} \tag{2.2.18}$$

Here

$$\tau_0(q_\parallel) \cong \frac{2\eta[cosh^2(q_\parallel h)+q_\parallel^2 h^2]}{\gamma q_\parallel[sinh(q_\parallel h)cosh(q_\parallel h)-q_\parallel h]} \tag{2.2.19}$$

Here, μ is the real and frequency independent shear modulus.

When

$$\tau_0(q_\parallel) \ll \frac{\eta}{\mu}, then\ \frac{1}{\tau(q_\parallel)} \cong \frac{1}{\tau_0(q_\parallel)} \tag{2.2.20}$$

$$\tau_0(q_\parallel) \gg \frac{\eta}{\mu}\ , then\ \tau(q_\parallel) \approx \frac{\eta}{\mu} \tag{2.2.21}$$

Eq. 2.2.20 is the purely viscous model used later to describe the capillary waves. In the results and discussion chapter, the simplified form of the capillary wave mode which is under the situation of **Eq. 2.2.20** is used to describe the experimental results later.

$$\tau(q_\parallel) \cong \frac{2\eta[cosh^2(q_\parallel h)+q_\parallel^2 h^2]}{\gamma q_\parallel[sinh(q_\parallel h)cosh(q_\parallel h)-q_\parallel h]} \tag{2.2.22}$$

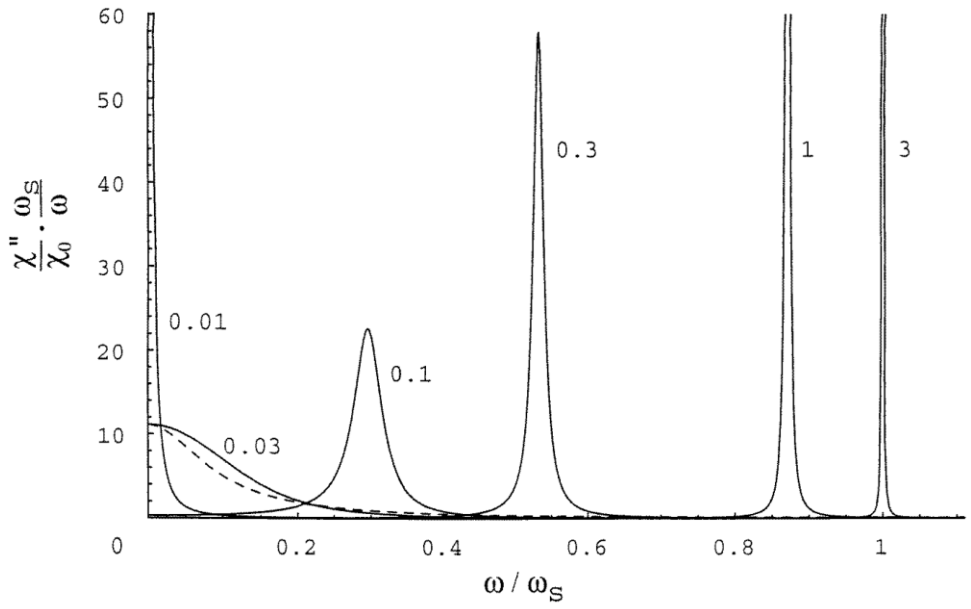

FIG. 2.2.2 The power spectrum of surface wave in dimensionless units for a nearly ideal liquid for kh = 0.01, 0.03, 0.1, 0.3, 1, and 3. Dashed line represents kh = 0.03. χ is the dynamic susceptibility of the vertical surface displacement with respect to an external force acting vertically on the liquid surface. ω_s is the frequency which referred to the surface wave on an ideal liquid of infinite depth. k is the wave vector. Reprinted with permission from Journal of Physics: Condensed Matter, Vol. 10, Josef Jäckle, The spectrum of surface waves on viscoelastic liquids of arbitrary depth, Page No. 7127. Copyright [1998], IOP Publishing, LTD.

2.3 Surface plasmon polariton

The free electrons in metals can move freely and thus can be thought of as an electron liquid with a high density of electrons, about $10^{23}cm^{-3}$. At optical frequencies, the metal's free electrons liquid can sustain surface and volume charge-density oscillations, so-called Surface plasmon polaritons (SPP) which propagate along the surface of the metal[97]. Several experimental geometries such as Otto and Kretschmann geometries have been employed to induce the SPP (**FIG. 2.3.3**). In this thesis, based on the setup of our REDLS, I will describe the procedure to induce the SPP by using evanescent waves. Further details can be found in the literature given by Novotny and Hecht (2012)[97], Raether (1988)[98] and Knoll (1998)[99].

When the light impinges from one medium with the refractive index of n_1 to another medium with the refractive index of n_2, light will be split into two at the interface, where a part of the light will be reflected and the other part of the light will be refracted into the medium. If $n_1 > n_2$,

the impinging light will be totally reflected beyond a specific angle, the critical angle θ_c which can be determined by Snell's law.

$$n_1 \sin\theta_1 = n_2 \sin\theta_2 \qquad (2.3.1)$$

Here, θ_1 is the incident angle and θ_2 is the refractive angle when the light impinges from medium 1 to medium 2. When the light is totally reflected, there is no light refracted into the medium 2 and the refractive angle θ_2 becomes 90°. If we take the interface between a glass prism and water as example (**FIG. 2.3.1a**), the critical angle for total reflection based on Snell's law is defined as

$$\sin\theta_c = \frac{n_d}{n_p} \qquad (2.3.2)$$

n_d is the refractive index of the dielectric medium, here it is water in **Eq. 2.3.2**. The refractive index of the prism is n_p, and θ_c represents the critical angle for total reflection.

When the incident angle is higher than the critical angle θ_c, the incident light is reflected totally and there is a so-called **evanescent wave** exited at the interface between two mediums with different refractive index. In the experiment, the critical angle θ_c can be found by measuring the reflectivity with increasing incident angle (**FIG. 2.3.1b**).

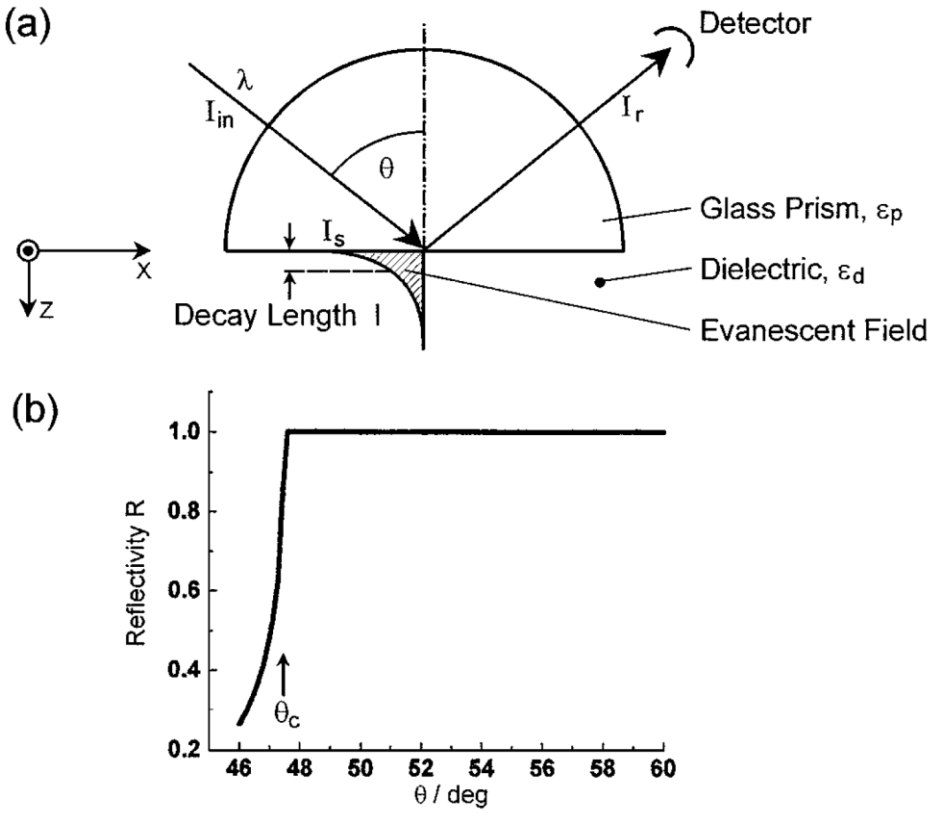

FIG. 2.3.1. (a) Schematics for total reflection of a light with wavelength λ and intensity I_{in} at the base of a glass prism with dielectric constant ε_p which is in contact with a dielectric medium of ε_d, and $\varepsilon_d < \varepsilon_p$. When the incident angle is over the critical angle θ_c for total reflection, the evanescent wave will show in the dielectric medium/glass prism interface with the intensity I_s which decays exponentially away from the interface. The decay length here is identical to the penetration depth used later.(b) Incident angle dependent reflectivity. The curve was calculated with $\varepsilon_p = 3.4036$ and $\varepsilon_d = 1.778$. Reprinted with permission from Annual Review of Physical Chemistry, Vol. 49, Wolfgang Knoll, Interfaces and thin films as seen by bound electromagnetic waves, Page No. 571. Copyright [1998], Annual Review.

The evanescent wave can be thought of as the incoming photon field, and be used to excite the free electrons at the metal surface to oscillate resonantly and which induces the SPP. The SPP can only be induced at interface between two mediums with dielectric constant of opposite sign (**Eq. 2.3.3**)[99].

$$\frac{k_{z1}}{k_{z2}} = -\frac{\varepsilon_1}{\varepsilon_2} \tag{2.3.3}$$

Here, k_z is the out-plane wave vector to the medium 1/medium 2 interface, and ε_i is the dielectric constant for medium i.

The complex dielectric constant of medium 1 and medium 2, e.g., $\varepsilon_1 = \varepsilon_1' + \varepsilon_1''$ and in-plane complex wave vector $k_x = k_x' + k_x''$ can be applied to describe the properties of SPP. The medium 1 is assumed as the semi-infinite metal and medium 2 is assumed as air or vacuum adjacent to medium 1. The dispersion relation for SPP at medium 1/medium 2 interface is[98]

$$k_x = \left(\frac{\varepsilon_1\varepsilon_2}{\varepsilon_1+\varepsilon_2}\right)^{1/2}\frac{\omega_{sp}}{c} \tag{2.3.4}$$

Here, ω_{sp} is the angular frequency, c is the light speed in vacuum.

The relation of k_x and incidence angle θ in the Kretschmann setup[100] which will be discussed later is shown as[101]

$$k_x = n_p\frac{\omega_{sp}}{c}\sin\theta \tag{2.3.5}$$

If we assume besides a real ω_{sp} and ε_2 that $\varepsilon_2'' < |\varepsilon_1'|$, the complex in-plane wave vector k_x is

$$k_x' = \frac{\omega_{sp}}{c}\left(\frac{\varepsilon_1'\varepsilon_2}{\varepsilon_1'+\varepsilon_2}\right)^{1/2} \tag{2.3.6}$$

$$k_x'' = \frac{\omega_{sp}}{c}\left(\frac{\varepsilon_1'\varepsilon_2}{\varepsilon_1'+\varepsilon_2}\right)^{3/2}\frac{\varepsilon_1''}{2(\varepsilon_1')^2} \tag{2.3.7}$$

The propagation length, L_{SPP} of SPP is

$$L_{SPP} = \left(2k_x''\right)^{-1} \tag{2.3.8}$$

The penetration depth, z, for different mediums are

In the medium 2: $$z_2 = \frac{\lambda}{2\pi}\left(\frac{\varepsilon_1'+\varepsilon_2}{\varepsilon_2^2}\right)^{1/2} \tag{2.3.9}$$

In the medium 1: $$z_1 = \frac{\lambda}{2\pi}\left(\frac{\varepsilon_1'+\varepsilon_2}{\varepsilon_1^2}\right)^{1/2} \tag{2.3.10}$$

The SPP is affected by the thickness and dielectric constant of the film which covering the metal surface where the SPP is excited. This property is used to measure the thickness of

polymer thin film by the Surface Plasmon Resonance Spectroscopy (SPR). The shift of k_x in the dielectric medium on the top of metal surface is[98]

$$\Delta k_x(h_d) = \frac{\omega_{sp}}{c}\frac{\varepsilon_d - 1}{\varepsilon_d}\left(\frac{|\varepsilon'_m|}{|\varepsilon'_m| - 1}\right)^2 \frac{|\varepsilon'_m| + \varepsilon_d}{|\varepsilon'_m| + 1}\frac{1}{\sqrt{|\varepsilon'_m|}}\frac{2\pi h_d}{\lambda} \qquad (2.3.11)$$

Here, the h_d is the thickness of dielectric medium, ε_d and ε_m are the dielectric constants for dielectric medium and metal, respectively.

In **FIG. 2.3.2**, the schematics of surface wave propagation and exponential decay of penetration depth away from the interface is shown.

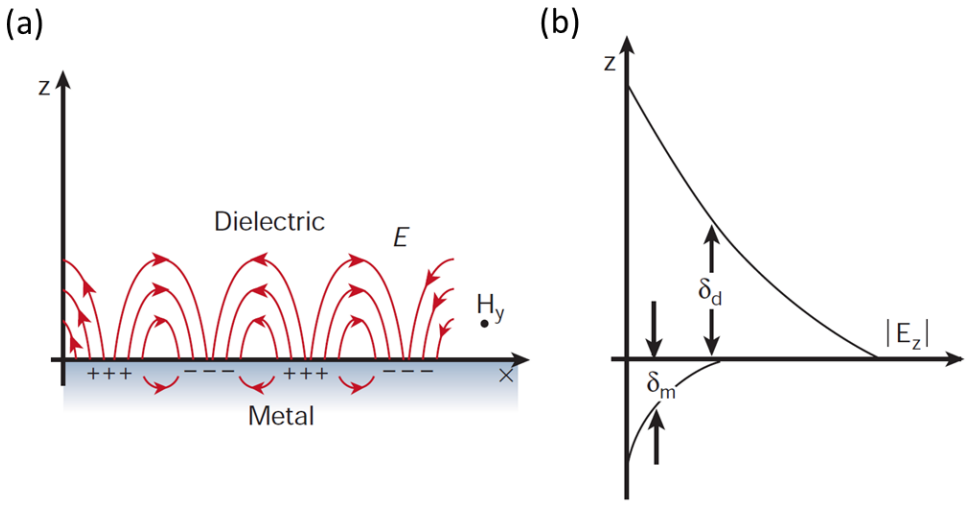

FIG. 2.3.2. (a) Schematics for the SPP propagation along the metal/dielectric medium interface. E is the electric field and H_y is the magnetic field in the y-direction. (b) The exponential dependence of the field E_z is shown. Reprinted by permission from Macmillan Publishers Ltd: Nature (Vol. 49, William L. Barnes and Alain Dereux, and Thomas W. Ebbesen, Surface plasmon subwavelength optics, Page No. 826), copyright (2003).

Based on the above discussion, one intuitive way to induce the SPP by evanescent wave is the Otto-configuration[102] (**FIG. 2.3.3a**). In the Otto-configuration, the SPP are excited by the tail of evanescent wave which is induced when the light impinges from glass prism to air over critical angle θ_c. The Otto-configuration is not so practical since the metal surface must be close to the glass prism within 200 nm and this space is easily affected by the surrounding e.g., dusts.

Hence, Kretschmann and Raether[100] introduced another setup for the SPP (**FIG. 2.3.3b**), which was also adopted by REDLS. In the configuration proposed by Kretschmann and Raether, the photons in the glass prism directly couple with the metal to induce the SPP. In the **FIG. 2.3.3b**, one side of metal layer is glass prism, and the other is dielectric medium. The thickness and dielectric constant of the dielectric medium will strongly affect the angle at which the SPP happens. We make use of these properties to characterize the thickness of polymer thin film in our study.

The thickness of thin film can be estimated from (**Eq. 2.3.5**, **2.3.11** and literature[103])

$$h_d = \frac{\varepsilon_{air}\lambda\sqrt{-\varepsilon'_m}(\varepsilon_{air}-\varepsilon'_m)\varepsilon'_d}{2\pi(\varepsilon'_d-\varepsilon_{air})(\varepsilon'_d-\varepsilon'_m)}\left(\frac{\varepsilon'_m+\varepsilon_{air}}{\varepsilon'_m\varepsilon_{air}}\right)^2 \Delta\left(\sin\Psi_{spp}\right) \qquad (2.3.12)$$

Here, ε_{air} is the dielectric constant of the air, and Ψ_{spp} is the resonance angle for the SPP. The SPP can be found by monitoring the sharp minimum of reflectivity and that angle is the resonance angle Ψ_{spp} (**FIG. 2.3.4**).

The estimation of film thickness depends on the shift of the resonance angle Ψ_{spp}, and also relates to the surrounding optical properties, e.g., the dielectric constant of metal and dielectric medium. Thus, the refractive index or film thickness cannot be determined independently only by the shift of the resonance angle Ψ_{spp} if not one of the two is known precisely.

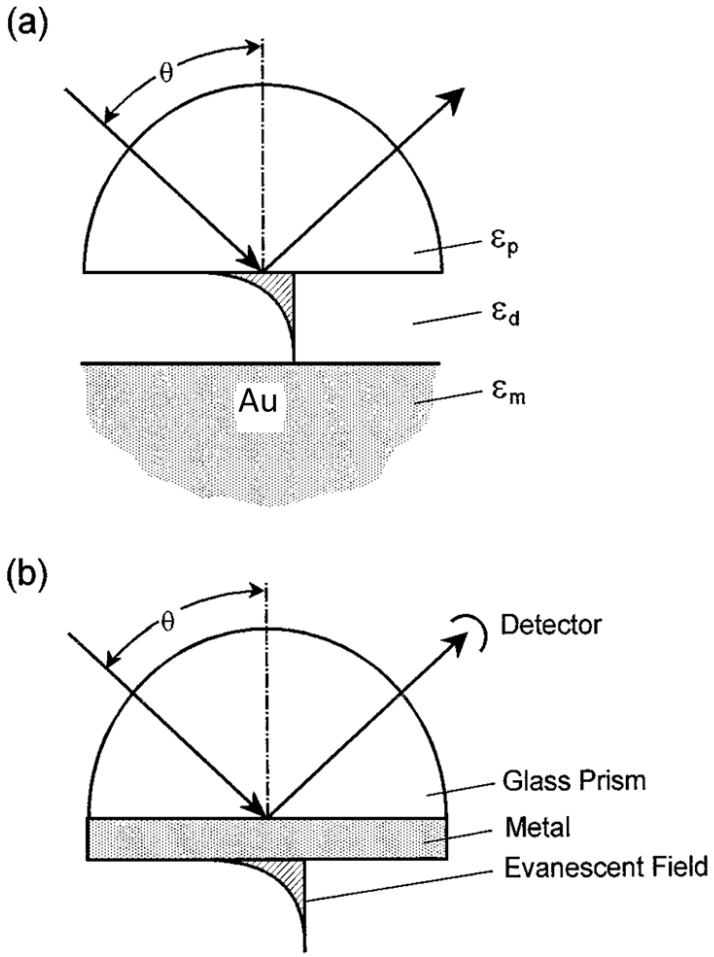

FIG. 2.3.3. (a) The Otto configuration. ε_p, ε_d, and ε_m represent the dielectric constant of glass prism, dielectric medium, and metal, respectively. (b) Attenuated total internal reflection (ATR) for the SPP excitation in the Kretschmann configuration. Reprinted with permission from Annual Review of Physical Chemistry, Vol. 49, Wolfgang Knoll, Interfaces and thin films as seen by bound electromagnetic waves, Page No. 578. Copyright [1998], Annual Review.

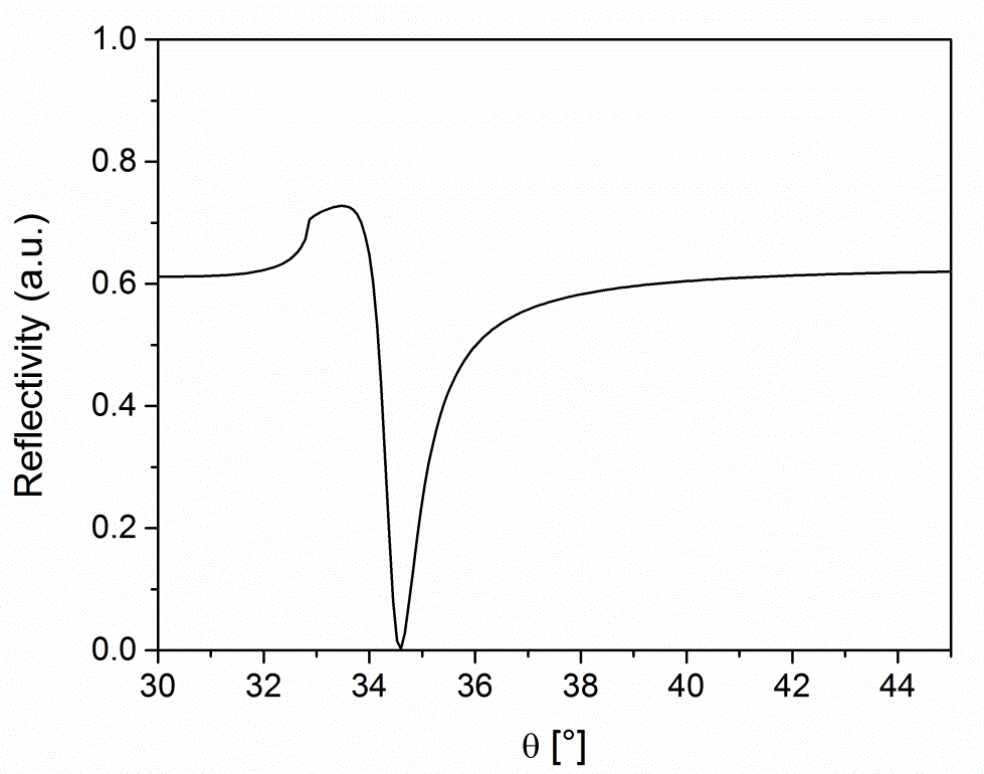

FIG. 2.3.4. Calculated reflectivity. The parameters are assumed as: half-cylinder prism, four layers: glass prism ($\varepsilon_p^{'}$= 3.4)/ 1 nm Cr ($\varepsilon_{Cr}^{'}$= -4)/ 47 nm Au ($\varepsilon_{Au}^{'}$= -12.3)/ air ($\varepsilon_d^{'}$= 1).

2.4 Dynamic light scattering

As mentioned in **section 2.1**, thermally activated density fluctuations are present in the polymer thin films, which induce the variation of the scattered light electric field, i.e., the signal intensity fluctuation. From the measured intensity fluctuation, we can obtain the correlation functions, from which we can further obtain the characteristic time of polymer chains motions. The intensity of the scattered light is proportional to the numbers of scattering units. In this session, I will briefly introduce the principle of dynamic light scattering based on Berne and Pecora (2000)[96]. Further theoretical details and application can be found in this textbook[96].

When light impinges on the polymer chains (**FIG. 2.4.1**) it will be scattered in all directions. The detector is set at a specific angle θ to capture the scattered light. Different detected angles θ represent the different probing length scale given by$1/|q|$ as is given in (**Eq. 2.4.1**). The wave

vectors of the evanescent (incident) and the scattered electric field are defined as $\vec{k}_i$ and $\vec{k}_s$, respectively (**FIG. 2.4.1**). Thus, the scattering wave vector is defined as q :

$$q \coloneqq |\vec{q}| = \left|\vec{k}_i - \vec{k}_s\right| = \frac{4\pi n}{\lambda} \sin\left(\frac{\theta}{2}\right) \qquad (2.4.1)$$

Here, λ is the wavelength of incident light and *n* is the refractive index of the sample.

The scattered light received by the detector at a given time is the superposition of radiated electric fields from polymer molecules in the scattering volume. The superposition of electric fields forming a speckle field will fluctuate with time since the dynamics of molecules is affected by the thermal fluctuation. In order to exact the characteristic time of the polymer dynamics, the time-dependent correlation function is applied to analyze the time-dependent fluctuating electric filed.

The output of the detector represents the intensity of scattered electric field, and their relation is $I(q,t) \propto |E(q,t)|^2$. Here, $I(q,t)$ and $|E(q,t)|$ are defined as the intensity and scattered electric field at a specific scattering wave vector q and time t. The intensity-intensity time autocorrelation function is shown as

$$\langle I(q,t_0)I(q,t_0+t)\rangle = C_{efficiency}\langle |E(q,t_0)|^2 |E(q,t_0+t)|^2\rangle \qquad (2.4.2a)$$

Here, the $C_{efficiency}$ is a proportionality constant related to the efficiency of the detector.

In the so called homodyne method, only the scattered light from the polymer molecules contributes to the intensity signal. Thus, $\langle I(q,t_0)I(q,t_0+t)\rangle$ is proportional to the homodyne correlation function $g_2(q,t)$. The **Eq. 2.4.2a** can be recast as

$$g_2(q,t) \equiv \langle |E(q,t_0)|^2 |E(q,t_0+t)|^2\rangle \qquad (2.4.2b)$$

If the intensity signal is a mixed contribution from a local oscillator (unscattered, direct or elastic light), this technique is called heterodyne detection. The heterodyne method enhances the signal intensity and raises the S/N ratio. In the heterodyne method, the local oscillator and the scattered light are mixed, so the autocorrelation function **Eq. 2.4.2a** is modified to

$$\langle I(q,t_0)I(q,t_0+t)\rangle = C_{efficiency}\langle|E_{loc}(q,t_0)+E(q,t_0)|^2|E_{loc}(q,t_0+t)+E(q,t_0+t)|^2\rangle \quad (2.4.2c)$$

Here, $E_{loc}(q,\mathrm{t})$ is defined as the electric field of the local oscillator.

Based on the following approximations we obtain the field autocorrelation function $g_1(t)$ directly:

(1) $\left|E_{ref}(q,\mathrm{t})\right| \gg |E(q,\mathrm{t})|$

(2) The fluctuation of the electric field from the reference light is negligible.

(3) The electric fields of scattered light and reference light (local oscillator) are statistically independent

The homodyne correlation function $g_2(q,t)$ and heterodyne correlation function $g_1(q,t)$ are connected via Siegert relation

$$g_2(q,t) = C_{base}[1+f|g_1(q,t)|^2] \quad (2.4.2d)$$

Here, C_{base} is the baseline and f is the correction factor for the instrument, both of them are constants.

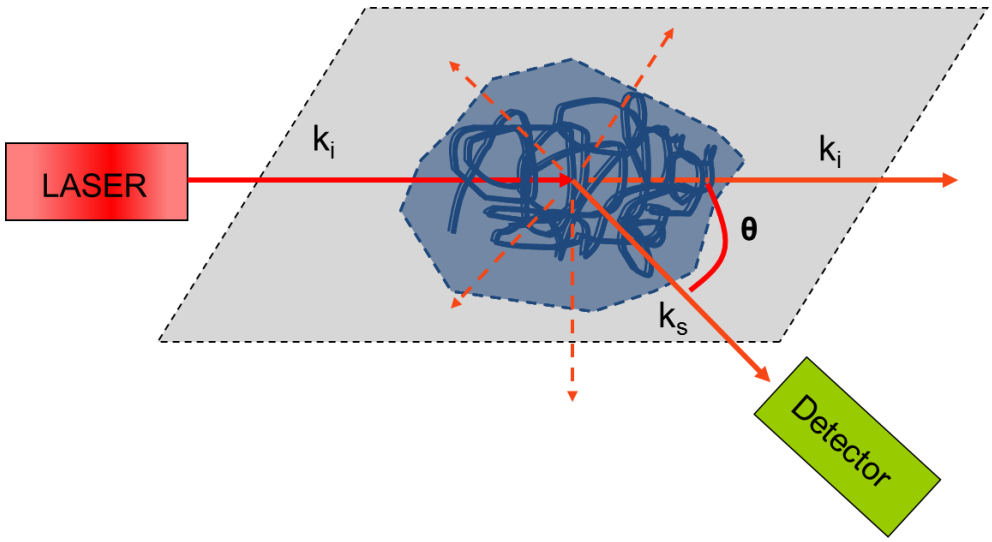

FIG. 2.4.1. Schematics for dynamic light scattering. Here, the wave vector of incident light is defined as $\vec{k}_i$, and of the scattered light is defined as $\vec{k}_s$. The angle between $\vec{k}_i$ and $\vec{k}_s$ is defined as θ.

Chapter 3

Materials and Experimental Methods

In this chapter, the sample preparation and the main experimental method, REDLS, will be introduced. Different methods of data analysis will be compared. The estimation of error for the experimental data of the custom-made REDLS will be also discussed.

3.1 Sample preparation

Our samples consist of polymer thin films and metal thin films which are supported by the glass substrate. The substrates used here are highly polished glass slides (Hellma, N-LaSF9). First a 1 nm Cr-layer was deposited by thermal evaporation onto the substrate to make sure that the following Au-layer is attached well. Subsequently a layer of 47 nm of Au was deposited in order to induce the SPP to be the light source. Then, the polymer thin films were spin-coated on the top of Au layer. The polymers were dissolved in toluene (HPLC-grade, Sigma Aldrich). Between 0.5 and 2 wt% solutions were spin-coated onto the Au coated glass substrate at 1000-5000 rpm for 5 to 10 minutes to prepare and dry the films. The 45 nm thin film usually could be obtained from 1 wt% solution at the speed of 1000 rpm. Since the thickness of thin films made by spin-coating are easily affected by the surroundings, the exact spinning-speed and the concentration of solution has to be modified each time one prepares films. Three different samples are used in this thesis: (1) PB thin films, (2) PS/PN bilayers consisting of PS thin films on the substrates covered by a thin film of PN, (3) PS thin films anchored to Au surface by PS polymers with a thiol group as end group. All the solutions used below were filtered through 0.2 μm PTFE filter (Rotilabo-syringe filter, not sterile, Carl Roth GmbH+Co. KG). All the thin films were prepared using glass syringes and stainless steel needles to avoid the contamination

by lubrication oil which is commonly used inside the plastic syringes and needles for medical application. Before preparing the polymer solution, all the glass syringes and stainless steel needles were rinsed and cleaned thoroughly by the solvent.

3.1.1 Polybutadiene (PB)

Polybutadiene (45% 1,4-cis-, 45% 1,4-trans-, 10% 1,2-vinyl) of two different molecular weights (as obtained by GPC), synthesized at Max Planck Institute for Polymer Research (MPIP) by anionic polymerization, was used. One, PB50, has molecular weight M_w= 50 kg/mol, M_w/M_n=1.08, and T_g = 172 K, the other, PB267, M_w= 267 kg/mol, M_w/M_n=1.10, and T_g = 175 K. A refractive index of n = 1.52 for the PB[104,105] was used subsequently in our analysis. Both polymers are well above the entanglement molecular weight and should show similar relaxation behavior. The viscosity of PB267 should be slightly higher due to the slightly higher T_g. These polymers, however, have a different radius of gyration; R_g of 8.5 nm for PB50 and 19.5 nm for PB267[106] chosen by us to test theoretical predictions about the dependence of confinement on dynamics on R_g or a multiple of it.

The polystyrene film was spin-coated on the Au substrate for 5 minutes. After spin-coating, samples were annealed in vacuum at room temperature (T_g+125K) for 12 hrs. This annealing removes satisfactorily the solvent from the films. No additional diffusion process of solvent in the films was detected in our experiments. The thickness of the films was checked by SPR (**Eq. 2.3.12**).

3.1.2 Polystyrene/ polynorbornene (PS/ PN) bilayers

The PS/PN bilayer is the PS thin film capped by the PN layer. Later in the results and discussions, the sample of PS capped by PN layer is presented like PS+thickness$_{PS}$+PN+thickness$_{PN}$. For example, the PS45PN20 means PS 45nm is capped by PN layer 20 nm.

Polystyrene used was synthesized at MPIP by anionic polymerization. The molecular weight (M_w) is 1821 g/mole (as obtained by GPC), M_w/M_n = 1.08, and T_g = 326 K. A refractive index of n = 1.59 for the PS[107] was used subsequently in our analysis.

The polystyrene was spin-coated onto the Au coated glass substrate for 10 minutes. After spin-coating, samples were annealed in vacuum. The samples were annealed with the following steps. First, the samples were annealed at 338K for 12hrs. Then, the temperature was increased to 348K for 12hrs. Finally the sample temperature was kept at 353K over 48hrs. This annealing removes satisfactorily the solvent from the films. No additional diffusion process of solvent in the films was detected in our experiments.

The norbornene monomer (Sigma-Aldrich, 99% purity, bp. 338K, vapor pressure 52mbar at 298K) is used to ignite a norbornene-plasma which then polymerizes on top of the polystyrene film forming a crosslinked PN layer. A cylindrical Pyrex plasma reactor was used, the details about the reactor and plasma-polymerized process are described elsewhere[108-110]. The pressure of the norbornene gas was controlled to be 0.05 mbar. A pulsed mode of plasma which is generated by setting t_{on} = 20 ms and t_{off} = 50 ms of plasma was adopted with an input power of radiofrequency at 50W. The thickness of PN layer was adjusted by the time of plasma reactor is switched on. The deposition rate was estimated of ~10 nm/min. Finally, the thickness of the films was checked by SPR.

3.1.3 PS thin film anchored to Au surface by thiol group

PS and the thiol terminated PS-SH used were synthesized at MPIP by using anionic polymerization. A refractive index of n = 1.59 for the PS[107] was used subsequently in our analysis.

The M_w of PS is 2695 g/mol (as obtained by GPC), M_w / M_n=1.06, and T_g = 326 K. The M_w of the PS which was modified by a thiol (-SH) group at the end is 3000 g/mol, M_w / M_n=1.2. The PS-SH was dissolved in toluene (HPLC-grade, Sigma Aldrich) at the concentration of 1mM.

Then the prepared gold thin film supported by the glass substrate was immersed in the 1mM PS-SH /toluene solution for 72hrs. After 72hrs, the substrate with the now covalently attached PS-SH was rinsed by the toluene solvent 10 times to remove the unbound PS-SH.

The PS of 2695 g/mole was spin-coated onto the Au coated glass substrate for 5 minutes. After spin-coating, samples were annealed in vacuum. The annealing temperature was processed in three stages. In the first stage, the samples were annealed at 338K for 12hrs. Second, the temperature was increased up to 348K for 12hrs, and then maintained the temperature at 353K over 48hrs. The above annealing process removes satisfactorily the solvent from the films. No additional diffusion process of solvent in the films was detected in our experiments.

The thickness of the films was characterized by SPR. Here, all the samples are named by the PS-SH/PS with the PS film thickness. For example, the PS-SH/PS85 represents the Au layer modified by PS-SH, and there is a layer of 85 nm of PS on top.

TABLE 3.1.1 The polymers we used to prepare samples in this thesis. P.D.I. polydispersity index, n refractive index

Abbrev.	Polymer	M_w (g/mole)	P.D.I.	T_g	n
PB50	Polybutadiene	50000	1.08	172K	1.52
PB276	Polybutadiene	276000	1.10	175K	1.52
PS	Polystyrene	1820	1.08	326K	1.59
PS	Polystyrene	2695	1.06	326K	1.59
PS-SH	Polystyrene modified by thiol end group	3000	1.20	283K	1.59

P.D.I. is the polydispersity and defined by M_w/M_n.

3.2 Resonance enhanced dynamic light scattering

REDLS (**FIG. 3.2.1**)[55,56] is a non-invasive, marker free technique to probe the dynamics of polymer thin films supported on a noble metal, in our case Au, to excite the SPP at the resonance angle $\Psi_{SPP.}$ The SPP is adopted to be the light source with penetration depth ξ = 200

nm. The light is scattered by the polymer thin film on the top of Au layer and collected by the DLS at an angle θ.

First, we have to attach our sample, the substrate with the film on top to the top of a half-cylinder prism . There are two reasons to use a half-cylinder prism here. One is that we can excite the SPP at a lower resonance angle Ψ_{SPP} when we measure the film with h > 60 nm. The other is, geometrically the SPP is always excited at the center of Au substrate which coincides with center of the goniometer in the REDLS (**FIG. 3.2.2**) at any resonance angle Ψ_{SPP}. This is not the case for angular prism where due to refraction the angle can shift substantially. Therefor it is easier in DLS to align the scattering light spot in/on the polymer thin film. We use PS of M_w: 400 g/mole to be the matching oil between the sample and the prism. The refractive index of matching oil should be as close as possible to the one of the prism, and does prevent internal reflection between the substrate and the prism which can interfere with the SPR measurement. When using PS of refractive index of 1.59 here to match the LaSFN9 prism and glass substrate with refractive index of both is 1.81 at λ= 632.8 nm, internal reflection and interference happen at angles over 55°; because of the half-cylinder prism we do not have to go to such high angles and therefor the interference is not hindering the experiment. The reason we choose PS to be the matching oil is because we will perform temperature dependent experiments and the matching oil is required to be thermally stable even at high temperature (over 373K) which is not the case for the commercially available matching oils which will fit better for the index matching.

When the light of a He-Ne laser (wave length λ=632 nm) impinges at the resonance angle Ψ_{SPP} on the sample, the evanescent part of the SPP is excited on the Au surface to be the light source in our dynamic light scattering experiment. In the experiments, the SPP is excited at the angle of the minimal reflectivity (**FIG. 2.3.4**) Ψ_{SP}. The sample is covered by a hemispheric quartz sample holder with $N_{2(g)}$ inside it to prevent the sample from oxidizing during measurement.

The light induced by the SPP will be scattered by the polymer thin film on the top of Au-layer since there are density fluctuations in and on the film. The REDLS is a heterodyne DLS setup.

This means the scattered light is mixed with light from a local oscillator formed by elastic, scattered light induced by the roughness of the gold film. One thing one has to make sure of is the amplitude of the local oscillator has to be much greater than the scattered light. According to the literatures[55,57,111], the intensity of signal contributed from the local oscillator is 1000 times or higher than the scattered light by choosing the proper surface plasmon radiation to ensure fully heterodyne DLS. The scattered light is collected at varying scattering angles θ (or wave vector q) by two photomultipliers (MP-973(6606-P-079)-Perkin Elmer) to obtain the pseudo cross-correlation function by using an ALV7004 fast multiple tau digital correlator (ALV, Germany). The pseudo cross-correlation is adopted to eliminate undesired signals[112]. The incoming signal is split into two to two photon detectors and their outputs into a correlator. The real data of intensity fluctuation and g_1 correlation function is shown (**FIG. 3.2.3**). The scattering wave vector q is defined as **Eq. 2.4.1**.

The REDLS setup sits on an anti-vibration table and is housed in a black housing to prevent and minimize interference from the surroundings. The anti-vibration system (AVI-350/LP, Table Stable) we use is a piezo-coil damping mechanism designed for vibration frequency from 1-200Hz with a damping of better than 35dB. The high frequency part of the vibration spectrum is passively damped by using an aluminum breadboard.

The capillary wave of polymer thin films is sensitive to temperature fluctuation. Temperature fluctuation induced by the environment can contribute to the signal and lead to spurious correlated signals. In order to prevent this we always used a heater to control the temperature by a control loop feedback mechanism, i.e., proportional-integral-derivative (PID) controller. In the PID controller, we set different values of 1, 0.1, and 0.01 for the Integral parameter in the PID to test if the feedback loop of the heater causes systematic errors producing correlated signals by e.g. systematically expanding/shrinking parts. At the integral value = 1, the signal we receive is influenced by the oscillation of temperature feedback loop. In the integral vales = 0.1 and 0.01, there is no influence to the signal. The temperature of the film is measured with a PT100 (#9 in

FIG. 3.2.2) pressed onto the film well outside of the scattering volume. The thermo sensor for the heating control is in the base of the prism holder (#8 in **FIG. 3.2.2**) to ensure quick reaction on temperature changes.

The scattering angle θ is an off-plane angle, and $q_{\parallel}$ is the component of the wave vector q parallel to the substrate plane. Because the capillary wave propagates along the surface of the film, q has to be replaced by $q_{\parallel}$ to describe the dynamics properly[7]. $q_{\parallel}$ and $q_{\perp}$ are defined as

$$q_{\parallel} := |\overrightarrow{q_{\parallel}}| = |\vec{q}| \cdot \cos\left(\frac{180°-\theta}{2}\right); \quad q_{\perp} := |\overrightarrow{q_{\perp}}| = |\vec{q}| \cdot \sin\left(\frac{180°-\theta}{2}\right) \qquad (3.2.1)$$

In REDLS one measures fully heterodyne correlation functions due to the mixing of elastic light from the Au surface[111] as local oscillator and the scattered light[55,56]. The related data analysis will be shown in the **section 3.3**.

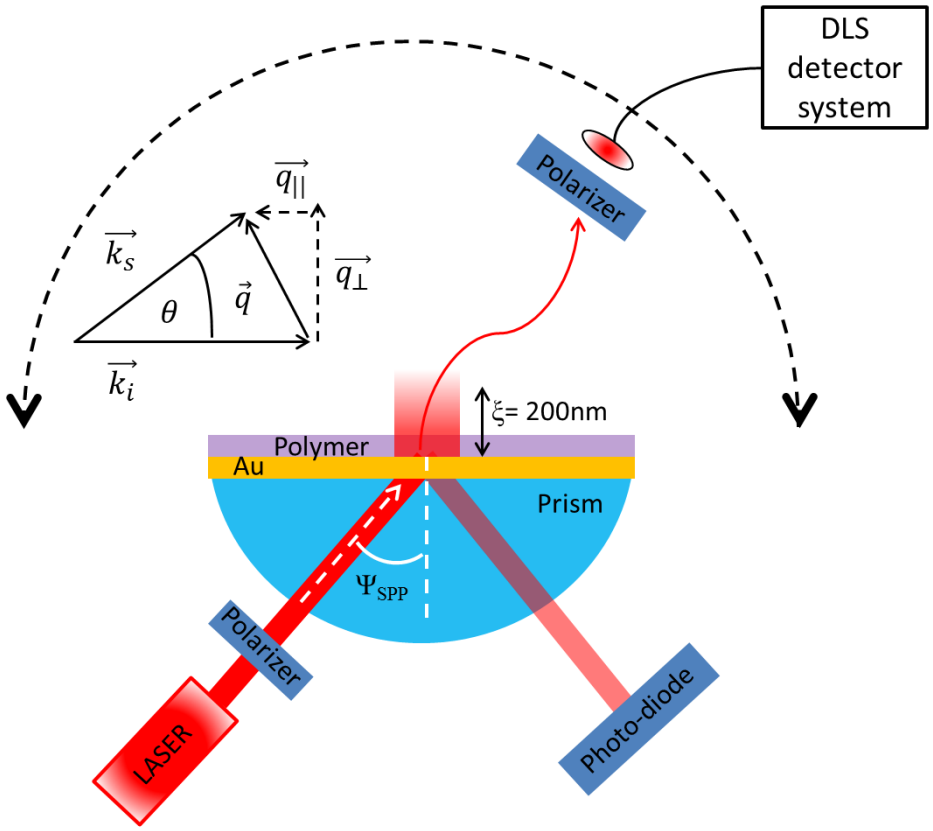

FIG. 3.2.1. Schematics of the REDLS setup. The LASER beam impinges at the resonance angle Ψ_{SPP} on the gold-glass boundary to excite the SPP in the gold layer with an evanescent field with a penetration depth ξ of 200 nm into the dielectric above. The polymer thin film is on the Au surface. The scattered light from the polymer layer is collected by the DLS detector system at a scattering angle θ. Polarized and depolarized light scattering is feasible via the build in polarizers to select the according combination of polarized light. The REDLS setup is adapted from Vianna's Ph.D. works.[57]

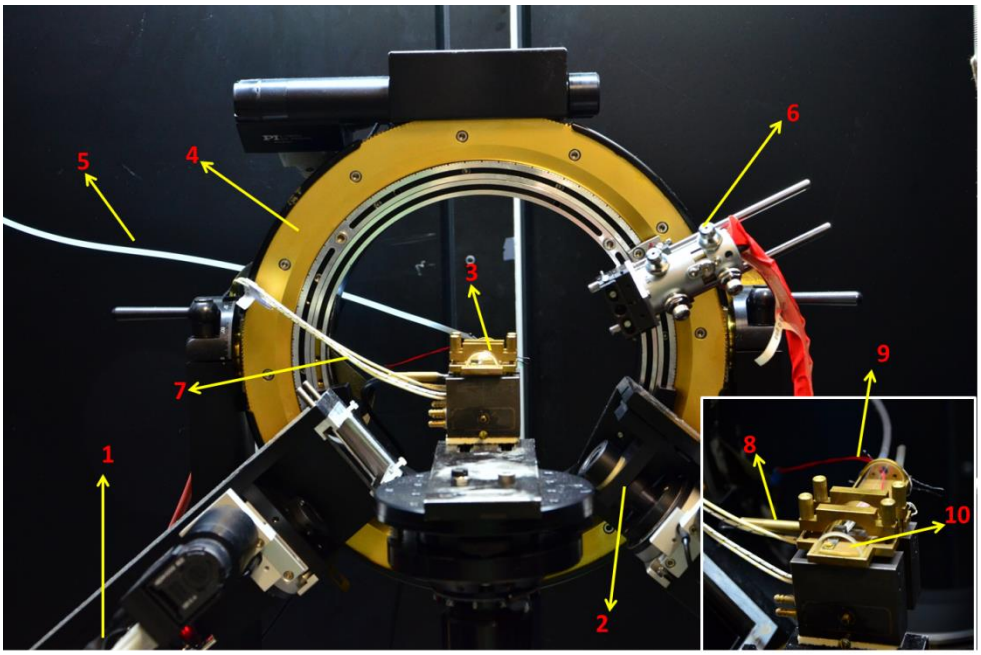

FIG. 3.2.2. REDLS setup: (1) He-Ne LASER λ=632.8 nm (2) photo-diode detector for the SPP (3) sample holder (4) goniometer from Optrel (Multiskop) (5) $N_{2(g)}$ connection to sample holder (6) holder for optical fiber which connects to the DLS detector (7) heater (8) thermo-sensor (PT100) for heating control (9) thermo-sensor (PT100) for monitoring the sample temperature (10) quartz holder to keep the sample holder under the $N_{2(g)}$ surrounding. The inset is the larger figure for the sample holder.

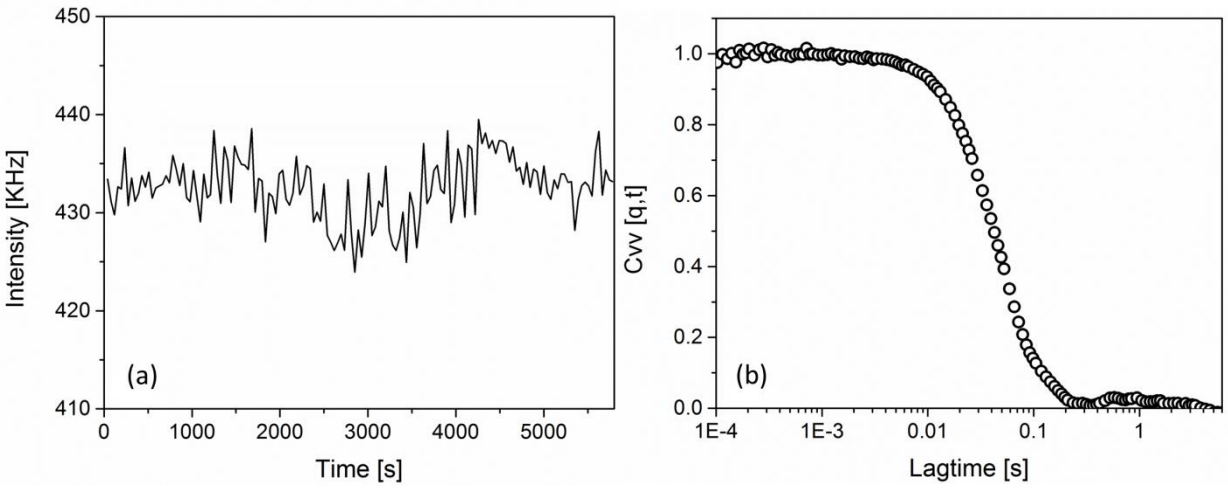

FIG. 3.2.3. Typical experimental data: (a) Time-dependent intensity fluctuation for PS thin film of 45 nm thick at 366K and q = 0.78×10^{-2} [nm^{-1}]. (b) Normalized heterodyne autocorrelation function in VV polarization which is calculated from intensity fluctuation (a) by the correlator automatically.

3.3 Data analysis

Despite the low polydispersity of our samples (see **TABLE 3.1.1**), there is an inevitable molecular weight distribution. This remaining polydispersity as well as hydrodynamic interactions of the solid substrate and the liquid-gas interphase on the dynamics lead to a distribution of relaxation times or rates. This distribution is expected to have a different form compared to the distribution in diffusion experiments in bulk solution following e.g. the distribution in sizes of particles. Thus e.g. fitting by the Cumulant[113] method is not justified in our case. Hence, we fitted the heterodyne auto-correlation functions by the empirical Kohlrausch-Williams-Watts equation (KWW) - the so-called stretched exponential decay.

$$C(q,t)=a\exp\left\{-\left(\frac{t}{\tau}\right)^{\beta}\right\}, \quad \Gamma=\frac{1}{\tau};\ 0<\beta\leq 1 \tag{3.3.1}$$

Here, the C(q, t) is our measured heterodyne auto-correlation function, *a* is the amplitude of the decay, τ is the relaxation time, and β is the stretching parameter describing the distribution of relaxation times. The physical relevant parameter is the mean relaxation rate <Γ> or the mean inverse relaxation time[114]

$$\langle\Gamma\rangle=\langle\frac{1}{\tau}\rangle=\frac{\beta}{\tau}\cdot\frac{1}{Gamma\,[1/\beta]} \tag{3.3.2}$$

with *Gamma* the gamma function. For simplicity in the following we denote <Γ> as Γ.

The comparison and discussion of different fitting methods are processed in the following:

In scattering theory, the diffusional motions of an ideal system of monodisperse particles are described by:

$$g_1(q,t)=exp(-\Gamma t), \quad \Gamma=1/\tau \tag{3.3.3}$$

the heterodyne correlation function. Here, Γ is the relaxation rate, τ the relaxation or characteristic time of this motion.

Due to the aforementioned reasons the relaxation process describing a motion has not a single exponential shape as in **Eq. 3.3.3**. Moreover, the samples do not show only one mode of motion, but combine different kind of motions at the same probing time and length; e.g., rod-like particles show translation and rotation.

Several methods have been developed to describe the decay function. Here, three widely-used methods are compared: Cumulant expansion [113], CONTIN [115,116] and Kohlrausch-Williams-Watts (KWW)[117,118]. We compare different distributions of relaxation time to examine the applicability of the above approaches.

3.3.1 Cumulant expansion

The Cumulant expansion is a method to expand the heterodyne correlation function by power series. For the multi-exponential decay, the **Eq. 3.3.3** is rewritten as:

$$g_1(q,t) = \int_0^\infty G(\Gamma) exp(-\Gamma t) d\Gamma \tag{3.3.4}$$

with

$$\int_0^\infty G(\Gamma) d\Gamma = 1 \tag{3.3.5}$$

Here, $G(\Gamma)$ is the distribution function of the relaxation rates, and the distribution from the mean is a Gaussian curve. The mean value is defined as

$$g_1(q,t) = exp(-\Gamma t) exp(-(\Gamma - \langle\Gamma\rangle)t) \tag{3.3.6}$$

Expanding **Eq. 3.3.4** by power series

$$g_1(q,t) = \int_0^\infty G(\Gamma)\, exp(-\langle\Gamma\rangle t) \left[1 - (\Gamma - \langle\Gamma\rangle)t + \frac{(\Gamma - \langle\Gamma\rangle)^2}{2!} t - \cdots \right] d\Gamma \tag{3.3.7}$$

$$g_1(q,t) = exp(-\langle\Gamma\rangle t) \left(1 + \frac{k_2^2}{2!} t^2 - \cdots \right) \tag{3.3.8}$$

$$ln\, g_1(q,t) = -\langle\Gamma\rangle t + \frac{k_2^2}{2} t^2 - \cdots \tag{3.3.9}$$

Here, $k_2 = \int_0^\infty G(\Gamma)\,(\Gamma - \langle\Gamma\rangle)^2 d\Gamma$

The method of Cumulants assumes the distribution of relaxation time to be narrow. In order to fit heterodyne correlation functions with a broad distribution of relaxation time, the method of CONTIN was developed to get a better estimate.

3.3.2 CONTIN

CONTIN[115,116] belongs to the class of constrained regularized methods of which it is the most used in data analysis of DLS data.

The distribution function $G(\Gamma)$ can be transformed to a sum of single-exponential decay functions by Laplace transformation.

$$\mathcal{L}[G(\Gamma)] = \int_0^\infty G(\Gamma)\, exp(-\langle\Gamma\rangle t) = g_1(q,t) \qquad (3.3.10)$$

We have to find the corresponding distribution function by inverse Laplace transformation from $g_1(q,t)$.

$$G(\Gamma) = \mathcal{L}^{-1}[g_1(q,t)] \qquad (3.3.11)$$

This is a so called ill-posed problem since there are infinite solutions existing to satisfy **Eq. 3.3.11** within small experimental error. Hence, in the method of CONTIN, some constraints have to be used. There are three strategies to achieve this goal[119]:

- Limiting of the extent of information being recovered: The number of components of the distribution function is limited.
- Incorporation of a prior knowledge: the non-negativity constraint, assume a specific analytical form and a certain more general feature of the distribution function.
- Parsimony or regularization: the simplest of all possible solutions compatible with the data is taken.

3.3.3 Kohlrausch-Williams-Watts function

The fitting function used in this study is named Kohlrausch-Williams-Watts (KWW) function or stretched exponential function. This is a straightforward fitting method to describe the distribution of relaxation time problem by tuning the power law.

$$g_1(q,t) = a\ exp\left\{-\left(\frac{t}{\tau}\right)^{\beta}\right\};\ \beta =]0,1] \qquad (3.3.12)$$

Here, a is the amplitude of the decay β is the stretching parameter. In the dynamic light scattering, the stretching parameter β is a measure for the width of the distribution of relaxation times.

The physical relevant relaxation parameter is the mean relaxation time or rate: <1/τ>=β<1/τ>/Gamma[1/β] with Gamma the gamma function.

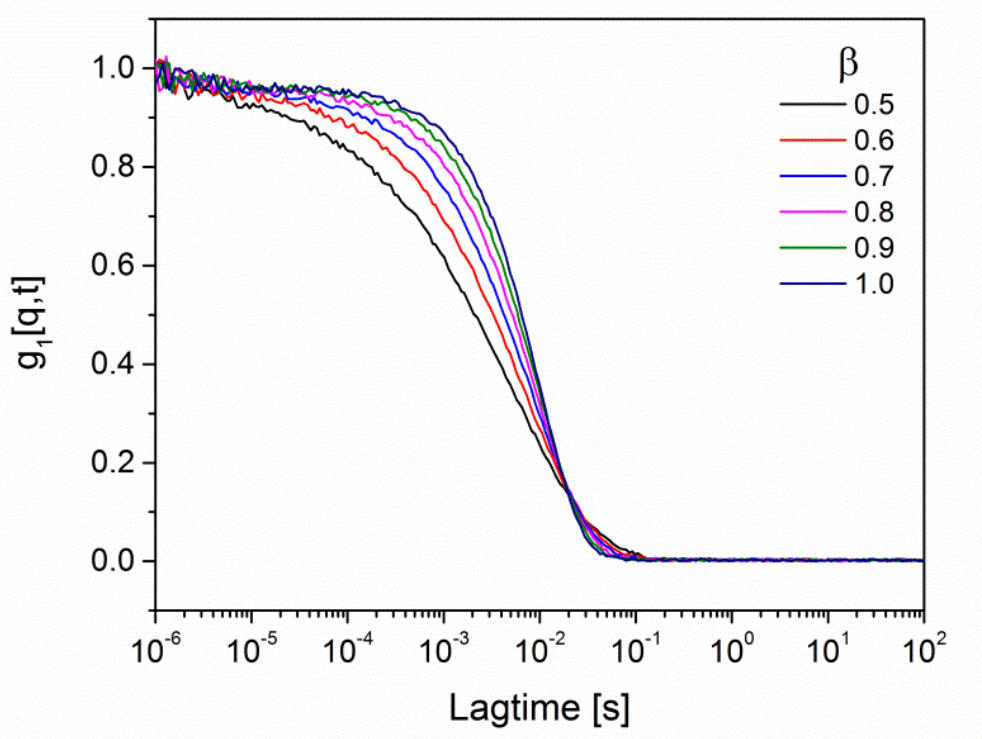

FIG. 3.3.1. Simulation of KWW function, **Eq. 3.3.12**, with different stretching parameters β from 0.5 to 1. The <Γ> is set to 100s^{-1}. The relaxation rate Γ of each β is defined by the relation <1/τ>=β<1/τ>/*Gamma*[1/β].

3.3.4 Comparison of methods

To test the applicability of the three fitting routines to as real systems we have simulated photon correlation spectroscopy curves by KWW functions varying the stretching parameter from 0.5 to 1 in steps of 0.1. The noise of each point is defined as (random number[0,1]/N, N is the number of each point). This mimics the increasing sample time in a modern multi-tau correlator which leads to a decrease of noise in real experiments with advancing lagtime.

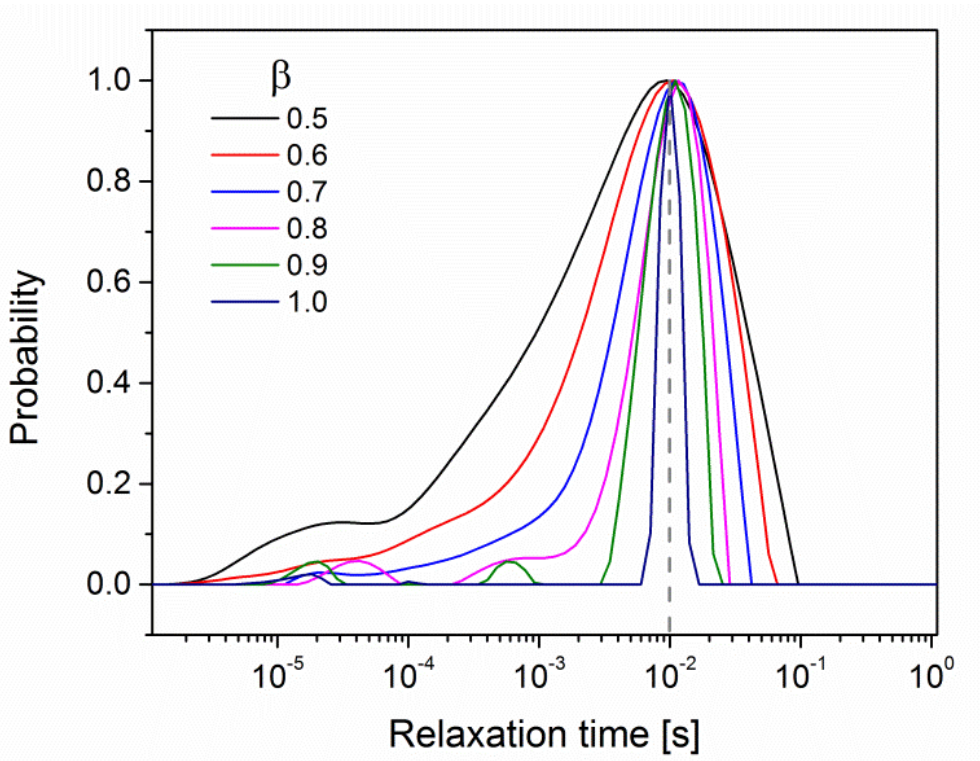

FIG. 3.3.2. The distribution curve of relaxation time from the CONTIN fitting results of **FIG. 3.3.1**. The grey dashed line marked the mean relaxation time 0.01 s.

Decreasing β value means the distribution of relaxation time increase, and makes the uncertainty of fitting increasing, too. Therefore, with the decreasing β value, the curves fitted by CONTIN deviate the pre-set mean relaxation time 0.01 s more, and the shape of distribution curves become broader and unsymmetrical (**FIG. 3.3.2**). Depending on the regularization parameter artificial side-peaks can emerge.

If the single exponential function $g_1(q,t) = exp(-\Gamma t)$ is fitted by the Cumulant method, of course, a perfect fitting result is obtained. However, after adding noise to the above single

exponential function, but β value remains at one, a poorer fitting result is obtained (**FIG. 3.3.3a**). With decreasing β value, the correlation functions are hardly fitted by the Cumulants well (**FIG. 3.3.3b**). Actually, besides the first term in **Eq. 3.3.9**, the remained parts do not give a good estimate of correlation functions.

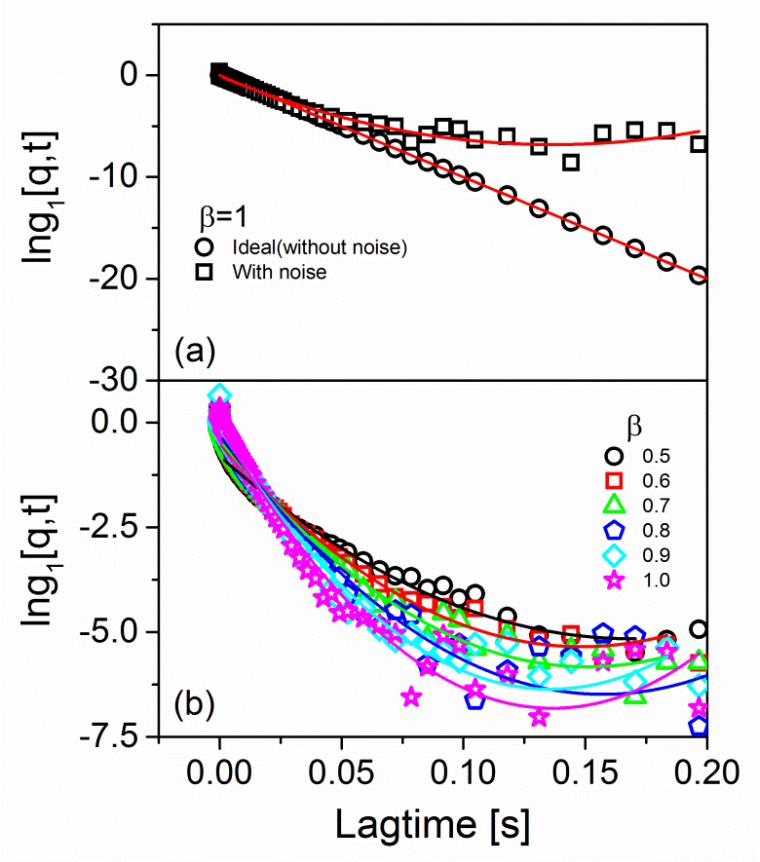

FIG. 3.3.3. (a) Comparison of the single exponential decay function $g_1(q,t) = \exp(-\Gamma t)$ with noise (☐) and without noise (O). (b) Comparison of Cumulants fitting results of **FIG. 3.3.1**. All of the solid lines are fitted by the **Eq. 3.3.9** to the quadratic term.

With increasing β value, the deviating relaxation times of Cumulants method converge to the pre-set value (**FIG. 3.3.4a**). When different fitting methods are compared at β=0.7 (**FIG. 3.3.4b**), the results of KWW and CONTIN almost coincide. However, the result of Cumulants is not as good as CONTIN, but still in the reasonable error range (within the central part of peak).

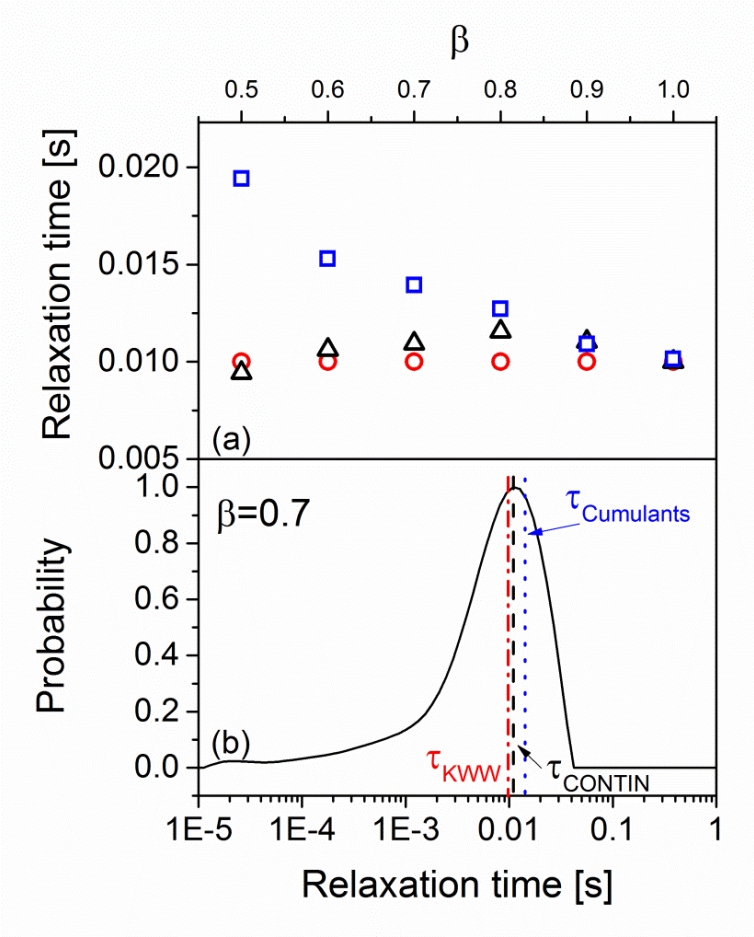

FIG. 3.3.4. (a) The relaxation time of heterodyne correlation functions in **FIG. 3.3.1** at the different β value from KWW(O), CONTIN(△), and Cumulants(□). (b) The distribution curve of relaxation time in the β=0.7. The different types of lines mark the relaxation time from methods: KWW (dash-dotted line), CONTIN (dash), and Cumulants (dot). Here, all the relaxation time of KWW is the mean relaxation time set to 0.01 s.

Comparing these three fitting methods, the KWW function is the method to describe the heterodyne correlation function. And it also shows the fitting results are better than CONTIN and Cumulants especially at smaller β value. Hence, it can be applied to solve the distribution of relaxation time problem, describe the correlation function well, and get a good estimate of relaxation times.

3.4 Experimental errors

The viscosities are fitted by the simplified capillary wave model[7]. Hence, the uncertainties are probably from several factors: surface tension, relaxation time, $q_{\parallel}$, and the film thickness.

The surface tension and relaxation time are affected by temperature. The error in surface tension and relaxation time from the error in temperature can be estimated by the influence on $d\gamma/dT$=-0.065 (mN/m K) and VFT law [120-122]. The $q_{\|}$ is affected by measuring the angle decided by the precision of the machine. The errors induced by the uncertainties of surface tension, relaxation time, and $q_{\|}$ are less than 4%. Compared to the uncertainties induced from thickness, the effects from the surface tension, relaxation time and $q_{\|}$ errors are much smaller and can be neglected.

The thickness of our films is measured by Surface Plasmon Resonance Spectroscopy (SPR). The error of thickness characterized by SPR is usually much less than 1 nm if the film is attached in situ in the SPR experiment. In our case in order to change samples easily, we have to spin-coat the thin film on glass substrates and use matching oil between glass substrate and prism. However, it is impossible to get exactly the same thickness of matching oil every time. This layer also affects the fit results for the thickness of thin films. The worst case leads to an error of film thickness of ±2 nm. Therefore the largest error of viscosity in the thinner films is about 23% (as shown as error bar in PB 50, 23 nm, (**FIG 4.1.6b**). The error bar for viscosity is, due to the logarithmic scale smaller than the symbol size.

Chapter 4

Results and Discussion

In Sulivan D.B. Vianna's PhD thesis[57], the capillary waves of polystyrene (PS) thin films were measured above but close to T_g. In cooperation with the theory group of Prof. Dr. Kurt Kremer at the Max Planck Institute for Polymer Research and the group of Prof. Dr. Klaus Rätzke at the University of Kiel, the density and free volume voids of PS thin film at an Au interface were studied[35] by multiscale molecular simulation and positron annihilation lifetime spectroscopy (PALS). In the experimental part, PALS, shows a higher density of polymer chains at the Au/PS interface and smaller free volume voids in the thin film compared to the bulk. These experimental results are in agreement with the simulation results from the multiscale molecular dynamics simulations where the higher density of polymer chains is found to be close to the Au/PS interface.

Based on this study, we measure polymer thin films in different elastic modulus and are changing the confinement imposed on the thin films to observe how e.g. the substrate affects the capillary wave dynamics. One approach is to use PB thin films which are a liquid at our measuring temperature which is above T_g + 125K. Compared to the PS, the PB thin film is a suitable low viscosity sample to test the capillary wave model in different polymer film thickness. In a second approach, the capillary wave of PS thin film is suppressed by a glassy capping layer to answer if there are other motions contributing to the thin film dynamics. The third approach is to test the influence of a more or less immobilized layer at the substrate interface, the PS is anchored to the substrate by thiol group. The dynamics of capillary waves can be tuned via modifying the interaction at the substrate/polymer interface and prove the existence of several modes of motions at the polymer/air interface and in the polymer.

4.1 Capillary wave dynamics of thin liquid PB films

The confinement on different length scales can be affected e.g. by type of substrate, modulus of thin film, and temperature. Thin films of PS close to T_g where studied by Vianna[57]. Hence, one of the polymer materials studied in this thesis, PB, is a polymer which is close to the behavior of a Newtonian fluid since it is being used for experiments at very high temperatures compared to T_g. On the other hand it is in the entanglement region of high M_w and one should be able to observe how long-range motions of polymer chains are suppressed by a less mobile layer[46,123] at the interface to the solid substrate. We measured the polybutadiene (PB) at 298K (i.e. T_g + 125K), where the thin films are liquid. To be in the same range PS will have to be heated to 450K and more to be close to a Newtonian liquid. At these high temperatures these PS films are not stable. The molecular weights of PB we studied are beyond 50 kg/mol corresponding to the highly entangled region (entanglement Mw: 1.85 kg/mole)[124].

This also avoided thin film dewetting and kept the films mechanically stable during measurement. Here, we did not do temperature dependent measurement. The reason is, the purpose of this study is to observe the confinement effects at the low modulus and high temperature region, and start from a single measuring temperature. Most of the results we observe can be described by capillary wave models[2,20], but we find that the viscosity of the PB thin films is sensitive to the film thickness. We account for the mechanism of our findings by using a three layer model.

The following results and discussion of section **4.1** are adapted and partially reprinted with permission from Journal of Chemical Physics, Vol. 141, Fan-Yen Lin and Werner Steffen, Capillary wave dynamics of thin liquid polymer films. Copyright [2014], AIP Publishing LLC.

4.1.1 Results and discussion

Film stability

A dewetting during the experiment shows up as a drastic change in incident intensity in the REDLS experiment due to the change in local refractive index. In cases we observed this, we discarded the measurements.

Here, the AFM images (**FIG. 4.1.1 and 4.1.2**) are obtained after the REDLS measurement. There is no dewetting pattern observed in the topography images of different scale at thickness 25 nm and 75 nm for PB50 (**FIG. 4.1.1a, c and 4.1.2a, c**). The roughness (rms) of PB50 at thickness 25 nm and 75 nm are lower than 1nm for the range below 1μm×1μm. This roughness may be induced by the dynamic heterogeneities in a thin liquid-like layer at the glassy polymer surface as reported[125]. All the samples were measured in contact mode at 298K under 1 atm in air (Dimension 3100, Digital Instruments).

Most experiments conducted in the past on polymers in thin films were done in a low temperature regime, i.e. above and close to T_g. Here we explore the dynamics for temperatures far above T_g. PB can be assumed to be close to a viscous polymer liquid since at 298K it is 126 K above its T_g. The relaxation time of PB thin films increases with decreasing film thickness (**FIG. 4.1.3a**). We attribute this increase to viscoelastic effects and the stick boundary condition at the solid/liquid interface. The relaxation time decreases with increasing scattering wave vector (**FIG. 4.1.3b**) as predicted by the capillary wave models[2,20].

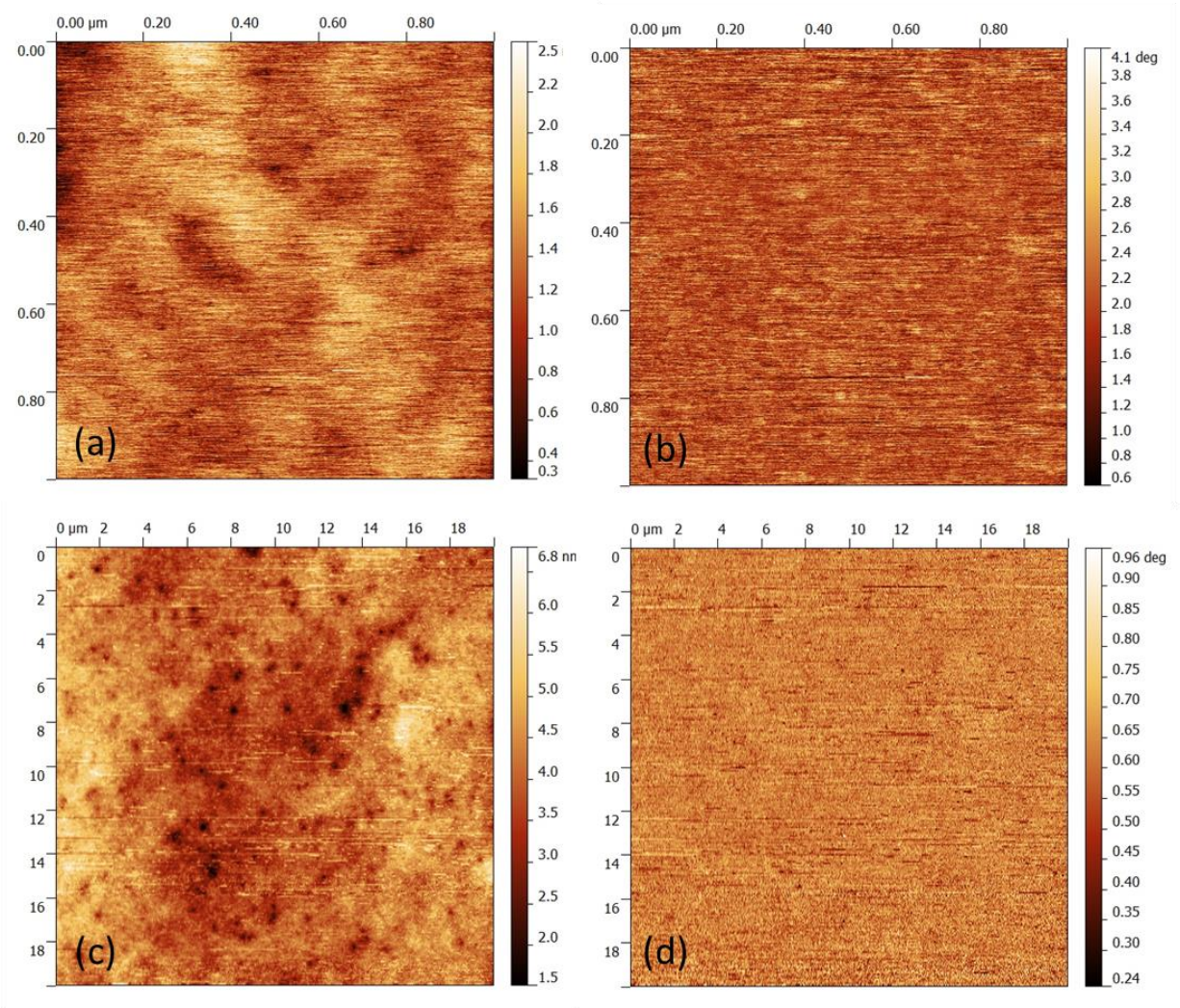

FIG. 4.1.1. AFM measurement for PB50 obtained after the REDLS measurement, film thickness 25nm, at 298K. Topography images: (a) size 1µm×1µm (c) 20µm×20µm, and phase image: (b) 1µm×1µm (d) 20µm×20µm. The roughness (rms) are 0.278 nm for the range of 1µm×1µm, and 0.628 nm for 20µm×20µm, respectively.

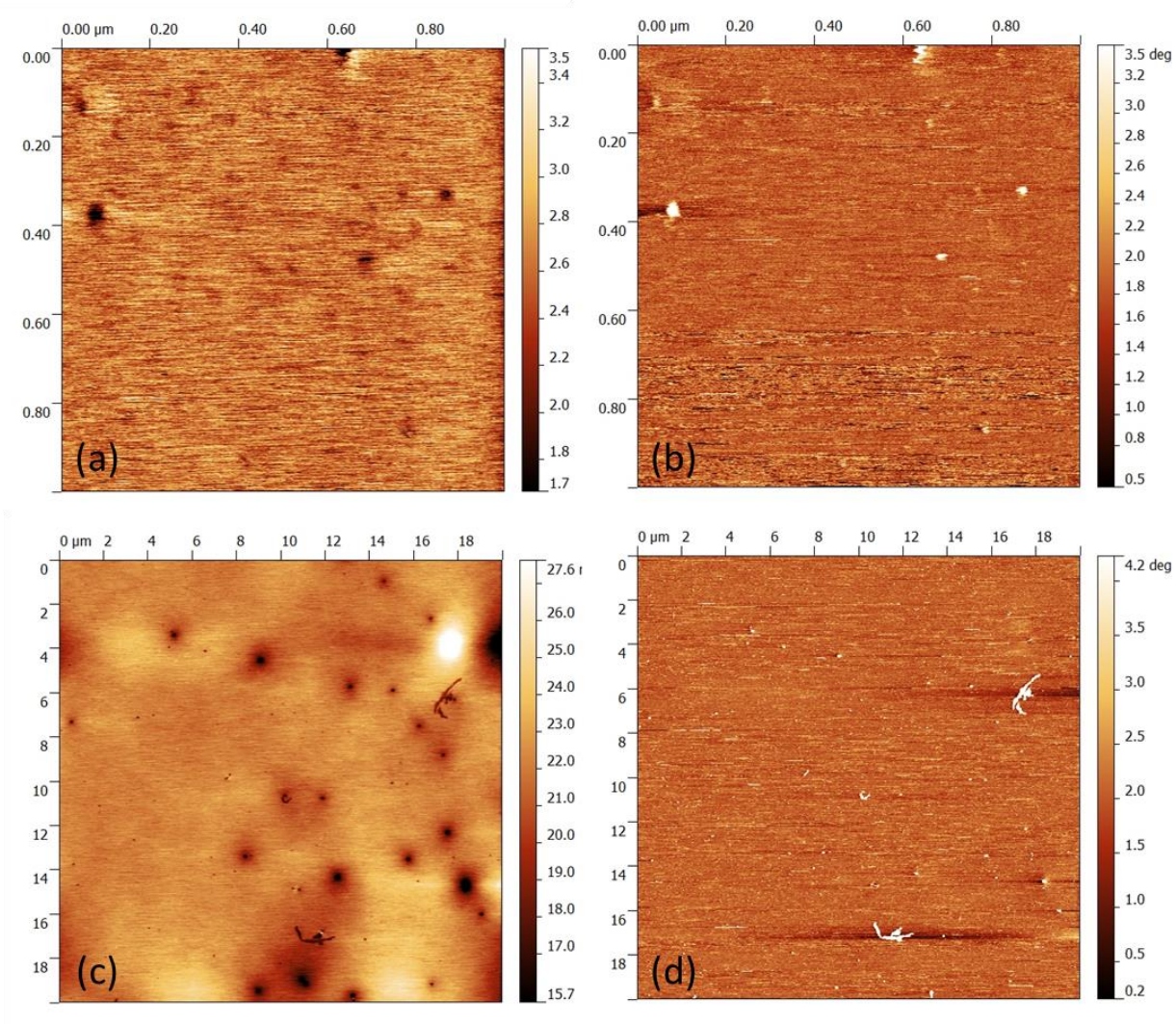

FIG. 4.1.2. AFM measurement for PB50 obtained after the REDLS measurement, film thickness 75nm, at 298K. Topography images: (a) size 1µm×1µm (c) 20µm×20µm, and phase image: (b) 1µm×1µm (d) 20µm×20µm. The roughness (rms) are 0.218 nm for the range of 1µm×1µm, and 1.24 nm for 20µm×20µm, respectively.

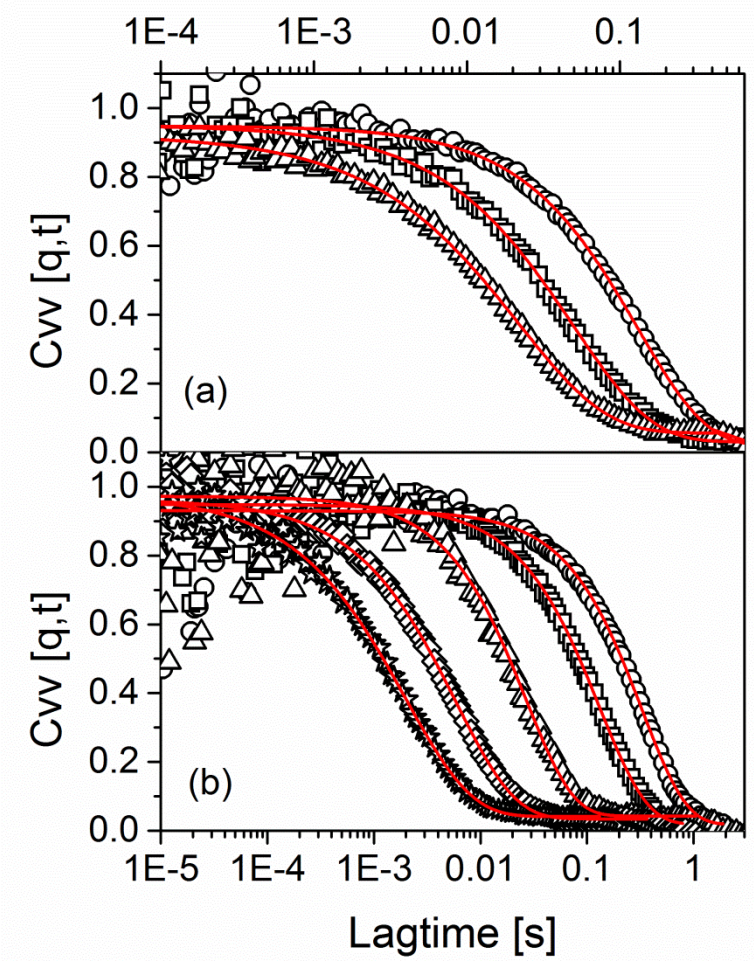

FIG. 4.1.3. Normalized, heterodyne auto-correlation functions for PB50 at 298 K (T_g+126K): (a) at $q_{\|}$ =0.37×10^{-2}[nm^{-1}] and different thickness h: (O) 45 nm, (□) 65 nm, and (△) 95 nm and (b) at h=45 nm and different scattering vectors: (O) 0.21×10^{-2}, (□) 0.37×10^{-2}, (△) 0.78×10^{-2}, (◇) 1.16×10^{-2}, and (★) 1.57×10^{-2} [nm^{-1}]. The solid (red) lines are fits by KWW functions.

In **FIG. 4.1.4a** the mean relaxation rate Γ is plotted vs. $q_{\|}$. The solid, red lines are fits by the capillary model with a simplification introduced in[7]:

$$\Gamma \cong \frac{\gamma q_{\|}\left(\sinh(q_{\|}h)\cosh(q_{\|}h)-q_{\|}h\right)}{2\eta(\cosh^2(q_{\|}h)+q_{\|}^2h^2)} \qquad (4.1.1)$$

Here η is the viscosity, γ the surface tension, and h the film thickness. The mean relaxation rate Γ is the inverse term of the relaxation time τ. Thus, **Eq. 4.1.1** is the inverse form of **Eq. 2.2.22** assuming a free liquid surface without elastic effects. The relaxation rate of the h=45 nm PB film can be well described by the capillary wave model. The only parameter in these fits is the viscosity η (**TABLE 4.1.1**) since γ is taken and/or derived from literature values of thick

films or bulk polymer. Thus we used 32.0 (mN/m) at 298K and linearly extrapolated γ to the other temperatures needed by $d\gamma/dT = - 0.065$ (mN/m K)[120] in our fits.

The viscosity of the PB thin film obtained from the fits decreases with increasing temperature. The absolute values were, however, lower by about two orders of magnitude (**FIG. 4.1.4b**) compared to bulk PB [121,126,127] with similar molecular weight; using $\eta \propto M^{3.4}$ we extrapolated these values to the molecular weight of our polymer. This is in contrast to other experimental work[7,41]. They found the viscosity of PS thin film system, using the same capillary model, to be close to the bulk value for PS.

The bulk viscosity for a polymer is correlated to the so called α-process of the glass transition at high temperatures[128]. Put into an activation plot, both, viscosity and α-process follow, besides the absolute scale, the same Vogel-Fulcher-Tammann (VFT) fit diverging towards the same temperature T_0. The theoretical finding[1,2] that the dynamics of thin films is faster is thus observed here via the lower viscosity in our ultrathin PB films. These lower, average viscosities hint to the existence of a more mobile layer. The other possible reason will be discussed later.

The apparent viscosity decreases with decreasing film thickness. The complete trend of viscosity vs. thickness is shown further down. In a transmission ellipsometry experiment[48] it was claimed, that there is more than one ‘accelerating mechanism’ acting on the thin film one stemming from enhanced mobility at the free surface.

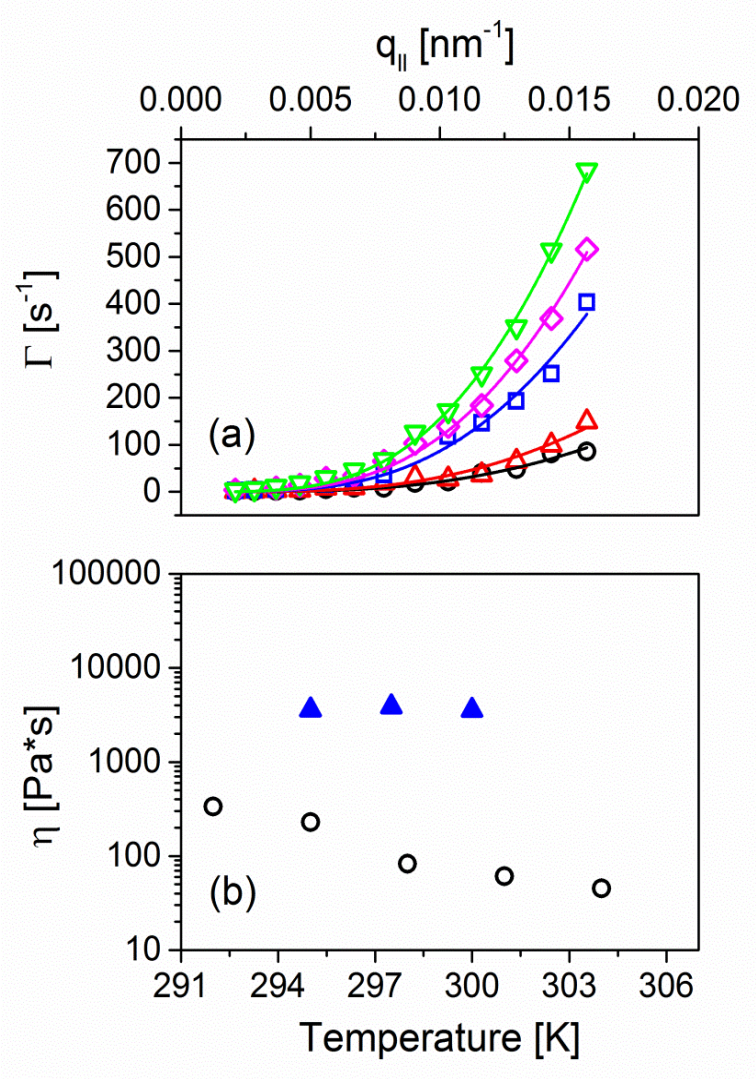

FIG. 4.1.4. (a) The $q_{||}$-dependence of the mean relaxation rate Γ for PB50, h=45 nm at different temperatures: (●) 292K, (△) 295K, (□) 298K , (◇) 301K and (▽) 304K. The solid lines represent least-squares fits based on the capillary wave model[7] represented by eq. 4.1.1. (b) Comparison of viscosities: (●) from fits of the capillary wave model (▲) bulk viscosity[121,126,127]. The error in viscosity is up to 14%, the error bars are smaller than the symbols and are omitted therefore.

TABLE 4.1.1. Viscosity η of PB50, film thickness 45 nm, vs. temperature obtained via the ratio γ/η as obtained from the fits with the capillary wave model in **FIG. 4.1.4**. Surface tension γ was taken from ref.[120].

T (K)	γ/η (nm/s)	γ (mN/m)	η (Pa s)
292	96300	32.4	336.5
295	140300	32.2	229.5
298	388300	32.0	82.4
301	523000	31.8	60.8
304	696000	31.6	45.4

When plotting the relaxation time as a function of the wave vector $q_{||}$ at different film thickness (**FIG. 4.1.5a**) or normalized film thickness (**FIG. 4.1.5b**) the results for the film thicknesses 45 nm, 65 nm, and 95 nm coincide in the region $q_{||}>0.96\times10^{-2}$ nm^{-1} (marked by vertical dashed line) within the experimental error. In the lower $q_{||}$ region the relaxation times deviate from each other for different film thickness. Dynamics is suppressed more strongly at lower $q_{||}$ in thinner films than in thicker ones. Such a deviation is described in the literature and cited as "cut-off"[14] or "transition"[13]. According to the literature[41,129], the van der Waals interactions introduces a low cut-off, and which is given by $q_{vdW}=(A_{eff}/2\pi\gamma)^{0.5}/h^2$ (A_{eff} is the Hamaker constant: 10^{-19}-10^{-20} J). The q_{vdW} is much smaller, i.e. in the order of 0.001 nm^{-1}, as the $q_{||}$ we find for the transition in our case. This implies that the transition in our experiments is most probably not caused by van der Waals interactions between polymer and substrate. The transition visible in our data is in the same range as found by Jiang et al.[41] studying PS films. They showed the surface dynamics becomes slower due to the confinement by the substrate but no transition for temperatures far above T_g was found. Hence, the transition we observe could be regarded as a transfer from a regime where the internal interaction of the polymer dominates (high $q_{||}$) to a substrate dominated regime (low $q_{||}$) analogous to Evans et al.[13] studying the influence of substrates of different modulus on their films.

In case the system follows the capillary wave model[7] (**Eq. 4.1.1**), according to this model all data normalized by thickness should coincide. However, a stronger reduction of surface dynamics is found by us in thinner films as also previously shown[13] at $q_{||}h$ lower than 0.4 (**FIG. 4.1.5b**). We attribute this to a stronger effect of the substrate when the film gets thinner.

Completely different is the observed behavior when h < 30 nm. The surface dynamics is suppressed even stronger and the trend of its relaxation time in different $q_{||}$ region is qualitatively different compared to the thicker films.

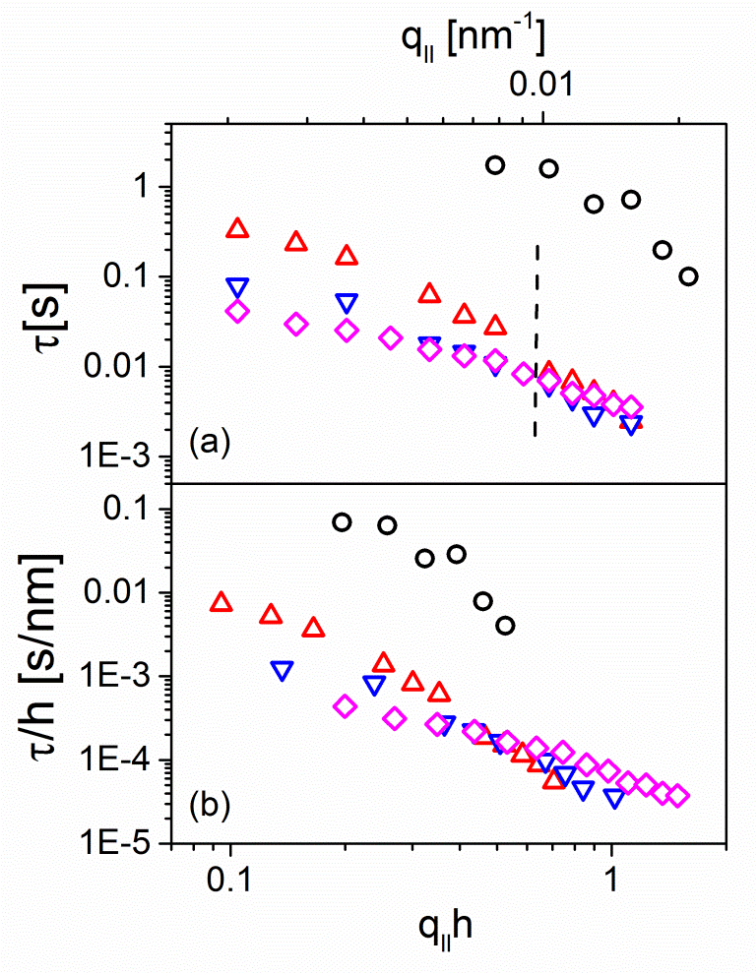

FIG. 4.1.5. (a) The $q_{||}$-dependent relaxation time at 298 K for PB50 of different thickness: (O) 23 nm, (△) 45 nm, (▽) 65 nm, (◇) 95 nm (b) The $q_{||}$-dependent relaxation times at 298K normalized by film thickness h by plotting τ/h vs. $q_{||}h$ for PB50. The dashed line marks the deviation of curves of different thickness.

In **FIG. 4.1.6a** the relaxation time τ is plotted as a function of h for two molecular weights. When h decreases from 95 nm to 30 nm, the relaxation time of PB50 films increases over one order of magnitude. This slowdown may be explained by the immobilization of polymer at the interface to a solid substrate, which was postulated to extend over $3R_g$[14,41]. In ultrathin films of molten polystyrene (PS)[14,41] and for film thickness down to the 1 - $3R_g$ region, the surface dynamics was found to be slowed down by the substrate. However, the relaxation time of our system, PB267, displays the same thickness-dependent relaxation time trend as PB50 but there was no crossover at $3R_g$. Its relaxation time also increased over one order of magnitude but only when the film thickness is down to the 20 nm. Compared to the tube diameter of PB, which was

estimated to be about 3.0 nm[130], this is 6 - 7 times larger. Hence, in our systems, the beginning of the strong confinement effect from the substrate is limited to an absolute distance of 20-23 nm and the onset of this confinement effect is not related to $R_{g.}$

For the case of PS on Au at high temperatures compared to T_g recent computer simulations find the by the substrate affected length scale to be only a few nanometer[32,33], in any case much less than 23 nm. The density of polymer thin film adjacent to the substrate should increase compared to bulk. This higher density can be visualized as an ultra-thin less mobile viscoelastic layer near the substrate, therefore the relaxation time and the viscosity increases exponentially[46]. The effect of this layer on the dynamics supposedly effects not only this layer but via the long range motion of the polymer spreads into the film above[46]. The viscosity obtained as a fit parameter is plotted as a function of film thickness in different molecular weight (**FIG. 4.1.6b**). The viscosities of PB50 and PB267 at h = 23 nm region both increase over one order of magnitude compared to 30 - 35 nm and prove the above prediction[46].

On the other hand, the smallest viscosities of the PB50 and PB267 are at a film thickness close to 30 nm, and decrease in the range from 95 to 30 nm used here in the experiments with decreasing film thickness. These results fit the theoretical prediction[1,2] and experimental findings[17,22] about a more mobile layer existing near the free surface if we assume the polymer thin film is not a continuous but rather an inhomogeneous system[1]. In this model, there is a high density, less mobile layer adjacent to the substrate due to the confinement effect. On the other hand, there is a more mobile layer existing near the free surface. Between these two layers, the polymer shows normal bulk behavior (**FIG. 4.1.6c**). The viscosity of the whole film is an average over these three different viscosities. And the thickness-dependent viscosity is caused by the ratio of these three layers changing with different thickness of the whole film.

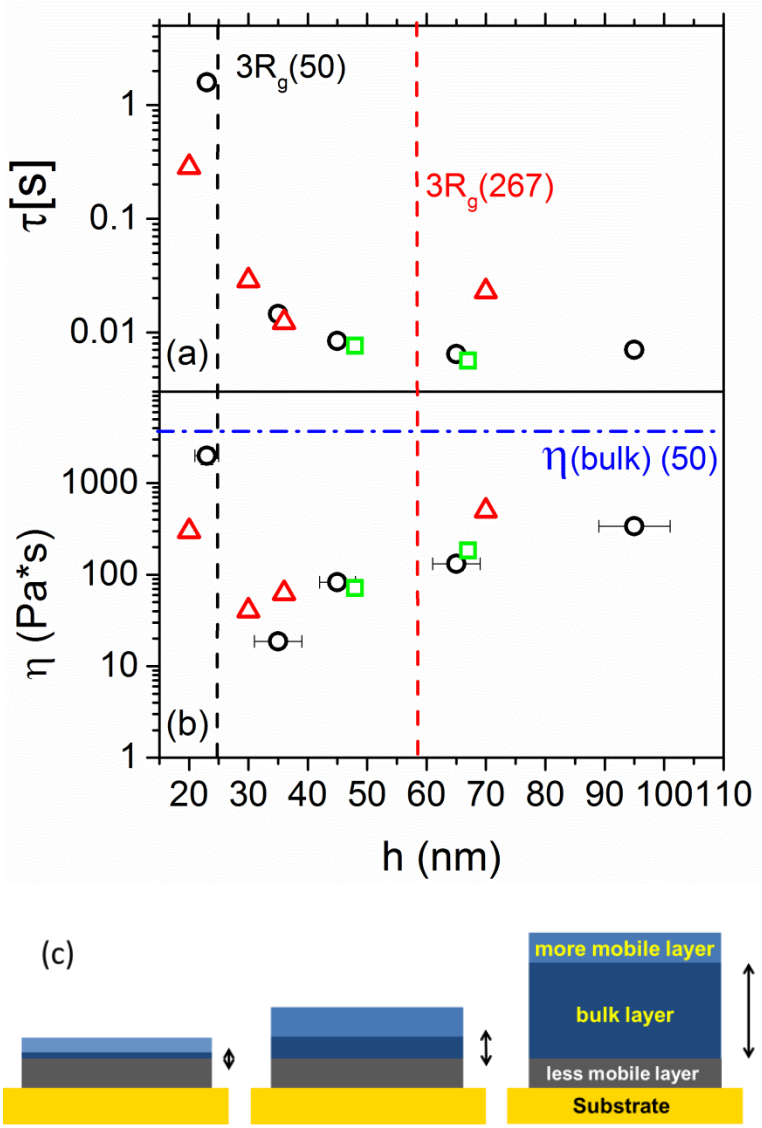

FIG. 4.1.6. Comparison of: (a) relaxation time τ and (b) viscosity η vs. film thickness h at 298K for PB of two molecular weights at $q_{\|}$ =1.03×10^{-2}(nm^{-1}): (O) PB 50 kg/mole (R_g = 8.5 nm), (△) PB 267 kg/mole (R_g=19.5 nm) (□)PB 50 kg/mole prepared with Heptane as solvent during film-preparation. The respective 3R_g is marked by vertical, dashed lines. The blue, horizontal dash-dot line in (b) marks the bulk viscosity for the PB50. (c) Schematics of the proposed three layer model for polymer thin film system. Error in thickness ±12% as marked by error bar; for τ and η the error is smaller than the symbols, error bars are omitted.

A further indication of a change of the relative contribution of each layer is the change of the distribution of relaxation times as described by the stretching parameter, β, (**Eq. 3.3.1**) of the KWW function. With the film being one homogeneous layer one would expect a constant β for all layer thicknesses h. Albeit the experimental uncertainty one can identify two regimes of β (**FIG. 4.1.7a**), a decreasing β for h ≤ 50 nm and a regime of constant β for h ≥ 50nm

β displays a strong, linear dependence on the scattering vector $q_{||}$ (**FIG. 4.1.7b**). While at low values of $q_{||}$ an almost single exponential behavior is observed, we find a pronounced broadening of the distribution of relaxation times τ in the high $q_{||}$ region. Since q is the inverse of the probing length this translates to being more sensitive to the different relaxation behavior in the three layers at short probing length.

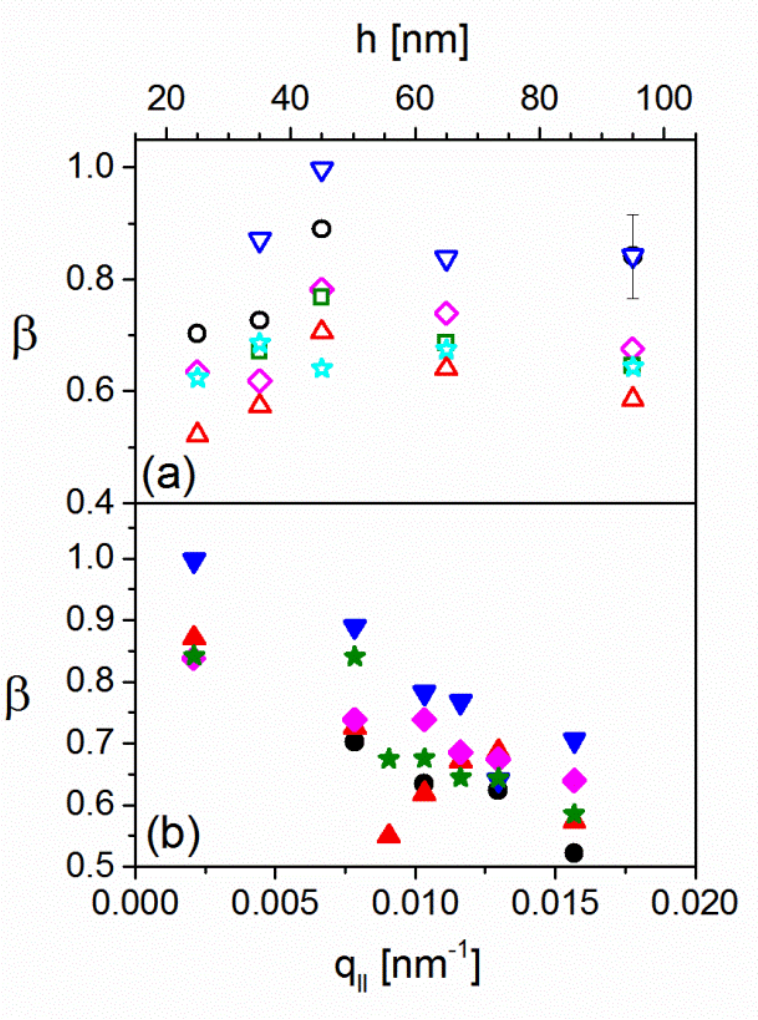

FIG. 4.1.7. Stretching parameter β from KWW fit for PB50 at 298 K (a) Thickness dependence for different scattering vectors: (▽) 0.21×10^{-2}, (○) 0.78×10^{-2}, (◇) 1.03×10^{-2}, (□) 1.16×10^{-2}, (☆) 1.30×10^{-2} and (△) 1.57×10^{-2} [nm^{-1}]. (b) q dependence for different h: (●) 23 nm, (▲) 35 nm, (▼) 45 nm, (◆) 65 nm, (★) 95 nm. Error in thickness ±12%, in q < 1%; for β ±9% at scattering vector 0.78×10^{-2} nm^{-1} in thickness of 95 nm shown on the plot.

We have to note, that even for "thick" films of h=100 nm the fitted, apparent viscosity is lower by about one order of magnitude as compared to bulk. We cannot explain this effect so far, not

even with the simulation results which showed a somewhat faster relaxation and thus lower viscosity in the PB-Graphite system[4,34]. Others[48] have found the dynamics to be the same as the bulk when the film thickness is higher than 100 nm. We rule out plasticization by remaining Toluene as the solvent for the spin coating on the basis of our rigorous annealing protocol. We also used with the same annealing protocol a theta-solvent for PB, Heptane, instead of Toluene to study possible solvent effects. The results show no considerable difference in the viscosity results (**FIG. 4.1.6b**). Furthermore, any remaining solvent will have diminished during our experiments over several days since the samples were kept under a N_2 atmosphere.

Further we have to note, that the relaxation times and hence viscosities obtained are solely from the dynamics of the capillary waves. Our results can lead to no statement about the motion of polymer segments.

For the low viscosities compared to bulk, a possible reason is the theoretical model used. The assumption of capillary wave model is based on a homogeneous single layer film. But our and other work [2-4,34] show the real polymer thin film is not a simple homogeneous layer with heterogeneous dynamics along the different depth. A modification of the capillary wave model by considering the film to be composed of several layers is beyond the scope of this work.

There is evidence to support the modification of capillary wave model in the literature[31]. By using Au nanoparticles as the markers in the XPCS experiments[31], the measured surface viscosity was about 30% lower than the remained part of thin film. This reduced viscosity was attributed to less entanglement at the surface while the measuring temperature is 56K to 86K above T_g. Compared to this XPCS experiment with Au nanoparticles, our measuring temperature is extremely high, T_g+125K. The melting degree of surface might be completely out of the assumption of capillary wave model.

4.1.2 Summary

Our results show the dynamics of thin polymer films at high temperature is confined by the substrate. We found the film viscosity to be over one order of magnitude lower than bulk and decreasing with decreasing film thickness down to 30 nm. This indicates a more mobile layer to exist near the surface. It plays a more and more important role with decreasing thickness. Below 30 nm thickness of the film the viscosity increases almost to bulk level which we attribute to an additional, less mobile layer at the boundary to the solid substrate. The ratios of less mobile layer in the vicinity of the substrate, more mobile layer at the liquid-gas interface, and the remaining bulk part in the thin film compete to govern the viscosity of the whole polymer film. All of our observations are in an agreement with theoretical predictions[1,2] and some other experimental findings [17,22].

4.2 Molecular motions of confined ultra-thin polystyrene films

The dynamics at and of interfaces between polymer/polymer influencing mechanical toughness of polymer blends[131], adhesion properties[132], and co-extrusion of polymer[133] is a fundamental question and of the scientific interest[134]. It also plays an important role in many applications such as coatings[108,135], advanced polymer electronics[136,137], and optical devices[138,139]. Each polymer layer has its own property. Through the different interfacial interaction e.g., slip, attractive, or repulsive, combining these polymer layers enables us to generate multilayer polymer systems which have unique properties and can be used for specific purposes. For example, for improving high density data storage devices[108], both high surface wear resistance and high plasticity are really required. Therefore a fundamental knowledge of the multilayer properties of polymer is essential.

We study here a polystyrene (PS)/polynorbornene (PN) bilayer (**FIG. 4.2.1**) to understand the dynamics of polymer/polymer interface and to find which influence the change of confinement has on the dynamics and hence the glass transition. PS is adopted as sub-layer. The polynorbornene (PN) on the top of PS behaves like a (solid) skin. The T_g of PS and PN are 326K and 473K, respectively. The measuring temperatures are close but above T_g of PS. Within the temperature region where we carried out the measurements, the capillary wave of the PS film should be suppressed by the glassy PN layer. We thus expect that the signals measured in our experiment mainly arise from the substrate or other dynamic processes present in the PS/PN interface via lowering the amplitude of the capillary wave. The dynamics of this bilayer is not only dictated by the PN/PS interface. The confinement effect from substrate also affects the dynamics of the bilayer.

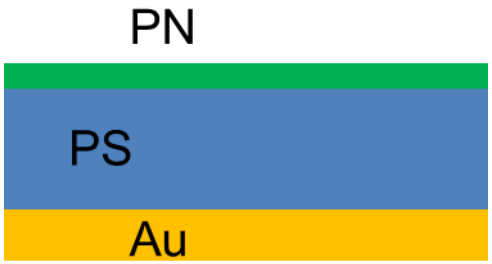

FIG. 4.2.1. Schematics of PS/PN bilayer on gold substrate. The bottom layer is Au, the inner, middle layer is polystyrene (PS). Polynorbornene (PN) is the top of thin film sandwich which is polymerized to the surface of PS directly by plasma polymerization.

4.2.1 Results

Film stability

The norbornene is polymerized to the surface of PS 45 nm thin film directly by a plasma polymerization process (see **section 3.1.2**). Here, the AFM images (**FIG. 4.2.2**) are obtained after the REDLS measurement. There is no dewetting observed shown in the AFM topography images (**FIG. 4.2.2**). The roughness (rms) determined in **FIG. 4.2.2** is close to 1 nm, the surfaces are extremely flat. All the samples are measured with AFM contact mode at 298K under 1 atm in air (Dimension 3100, Digital Instruments).

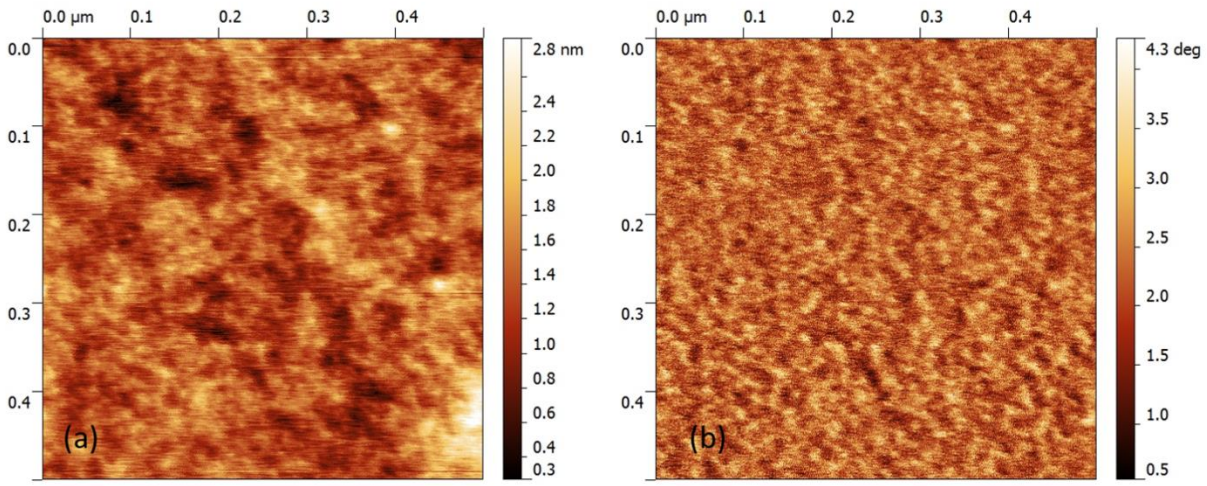

FIG. 4.2.2. AFM measurement for PS45PN10 at 298K obtained after the REDLS measurement. (a) Topography image and (b) phase image. The roughness (rms) is 0.3 nm for the range of 500 nm×500 nm.

The relaxation time of PS decreases with increasing film thickness (**FIG. 4.2.3b**). The film is confined strongly by the substrate with decreasing the thickness. Since the signal is sensitive to the thickness of the film, the signal should not be contributed from the bulk region rather but from the surface of polymer/air interface. The relaxation time decreases with increasing wave vector as predicted by the capillary wave model (**FIG. 4.2.3a**).

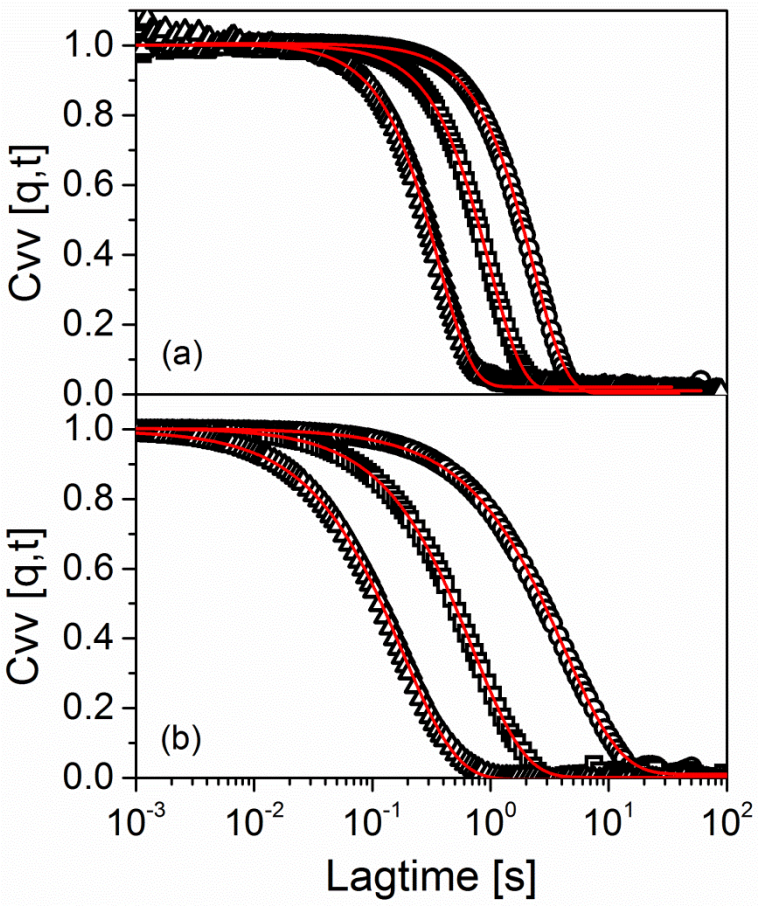

FIG. 4.2.3. Normalized, heterodyne auto-correlation functions for PS: (a) at h=45 nm, 366 K, and different scattering vectors: (O) 0.46×10^{-2}, (□) 0.78×10^{-2}, and (△) 1.57×10^{-2} [nm^{-1}], and (b) at $q_{||}$ =0.78×10^{-2}(nm^{-1}), 360 K, and different thickness h: (O) 25 nm, (□) 45 nm, and (△) 60 nm. The solid (red) lines are fits by KWW functions. Adapted from Vianna's Ph.D. works.[57]

The PS 45nm without PN capping layer shows a single exponential decay. The PS thin film with the same thickness of 45 nm capped by 10 nm PN layer also shows the single-exponential decay, but relaxation time becomes longer (**FIG. 4.2.4a**). This means the capillary wave is slightly suppressed by the PN layer. However, when the PS 45 nm is capped by a PN layer of 20

nm and more, the correlation functions becomes a bi-exponential decay (**FIG. 4.2.4b**). Of this new bi-exponential decay, one relaxation is faster than the original single exponential decay, and the other is slower. We denote these as Mode 1 and 2 for the faster and slower decays, respectively (**FIG. 4.2.4c**).

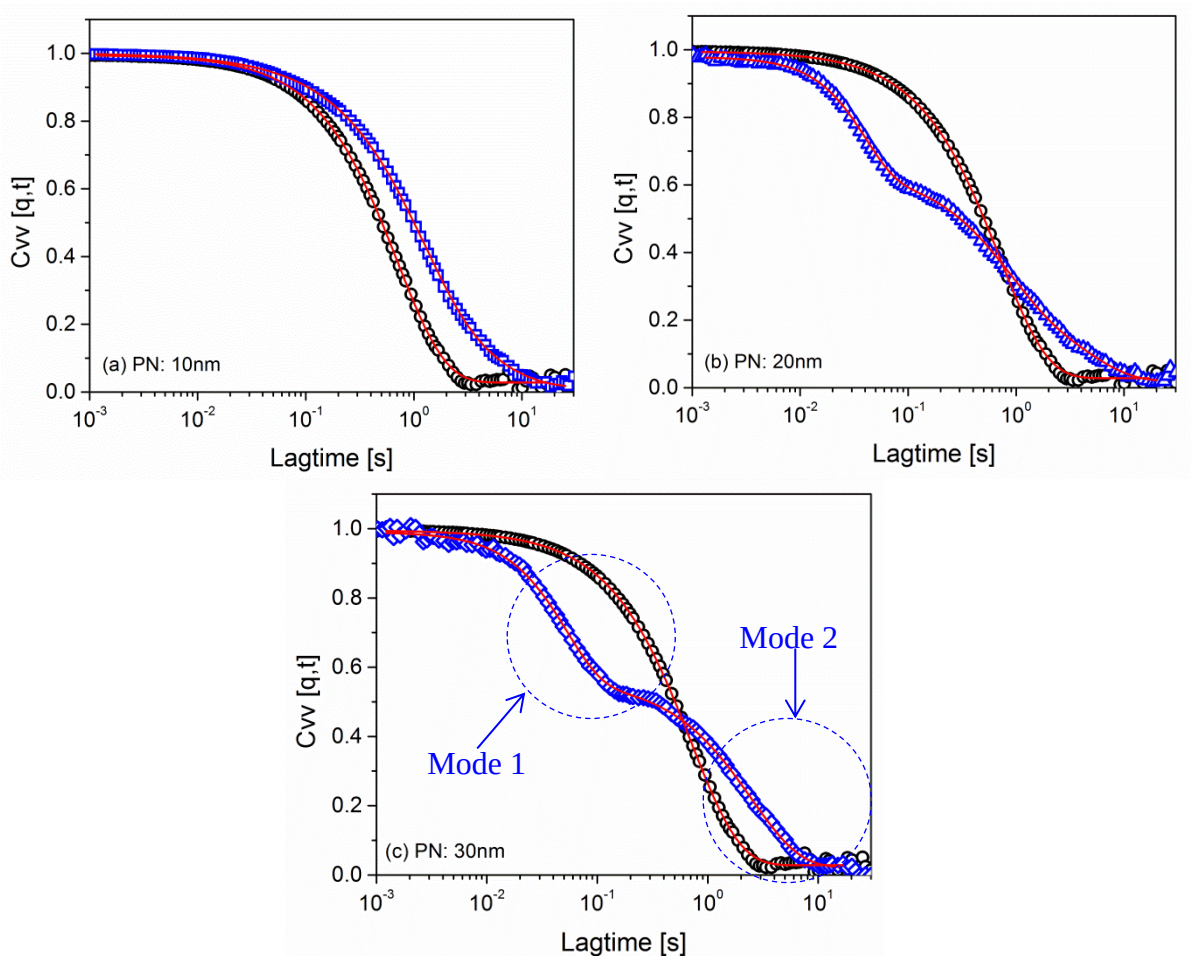

FIG. 4.2.4. Normalized, heterodyne correlation functions for PS (●) 45 nm at 360 K (T_g+34K) and PS 45nm/PN at 358 K (T_g+32K) at different PN thickness (a) (□) 10 nm, (b) (△) 20 nm, and (c) (◇) 30nm. All the data was measured at $q_{\|} = 0.78\times10^{-2}(nm^{-1})$. The solid (red) lines are fits by KWW functions. The data of PS45 is adapted from Vianna's Ph.D. works.[57]

The relaxation of the capillary wave of the PS 45 nm at different temperatures can be described by the Vogel-Fulcher-Tammann (VFT) equation with the parameters of $\tau_0 = 10^{-13.2}$ (s), B = 1767.2K, and T_0 = 276.8K comparable to the α-relaxation process of bulk PS (**FIG. 4.2.5a**). However, as is clear from **FIG. 4.2.5a**, the relaxation time for the PS 45 nm is much longer than that of the PS 200 nm[57] at the same temperature. The long relaxation time implies that the

surface dynamics of PS confined by the substrate. The correlation function of the PS45PN10 also behaves in similar way as the PS 45 nm, but shifts to longer lagtime region (**FIG. 4.2.5a**). This represents that the 10 nm thick PN layer retards the capillary wave dynamics of the PS45, but the capillary wave dose not vanish. This indicates that a thicker PN layer will be required to suppress the capillary waves completely.

When the thickness of the PN layers is 20 nm and more, the PS45PN20 and PS45PN30 show Arrhenius behavior for both Mode 1 and Mode 2 (**FIG 4.2.5b**). Since the temperature region in our experiment is much lower than T_g of the PN layer which was estimated to be over 473K, the PN layer is in the amorphous, glassy state. Thus, we can reasonably assume that signals contributing from the PN layer are negligible. We observe a transition from VFT to the Arrhenius behavior. We attribute this to the polymer chains being confined at small length scale. In the Arrhenius plot, the curves for the PS45PN20 and PS45PN30 are almost identical (**FIG 4.2.5b**). This means when the PN layer is 20 nm and more, the capillary wave can be suppressed completely and the PS layer behaves like polymer chains filled in the nanoporous structures[140]. The PN layer is like a glassy cap.

The activation energies of Mode 1 for PS45PN20 and PS65PN20 are almost the same (**FIG. 4.2.6**). When the thickness of the PS increases from 45 nm to 65 nm, the activation energy of Mode 2 increases from 10.5 kJ/mole to 47.0 kJ/mole and 47.0 kJ/mole is close to the activation energy for the bulk PS[141,142] (**FIG. 4.2.6**). Based on the assumption used in the capillary wave model, we conclude that the relaxation time of the surface dynamics decreases when the PS layer is thicker and less confined by the substrate.

PS45PN10 follows a similar $q_{||}$-dependent trend like PS 45 nm, but its relaxation rate is slower than PS 45 nm after the $q_{||} = 0.012$ nm^{-1} which is referred to probing length scale of 80 nm (**FIG. 4.2.7**). That is the smaller length scale (high $q_{||}$ region) of the capillary wave is confined more strongly because of the existence of the PN layer. The upward kink in the data of the PS45PN10 cannot be explained since due to experimental problems such a sample was not

available again and hence the data could not be reproduced to judge if this was a systematic error or if it is real. The PS45PN20 and PS45PN30 show the $q_{||}$-independent behavior (**FIG. 4.2.7**). The $q_{||}$-independent behavior is evidence that the polymer chains move locally. Thus, these support the assumption of capillary wave confined in the small length scale while the PN layer achieves the specific thickness.

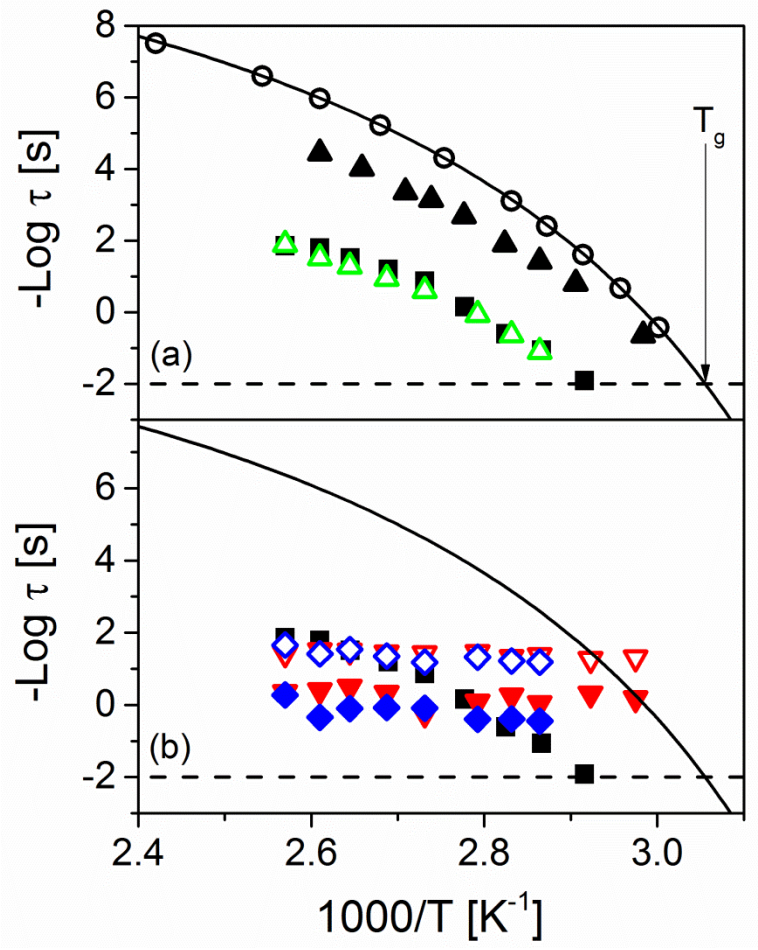

FIG. 4.2.5. Arrhenius or activation plot: (a) PS (O) bulk with the accompanying VFT-fit, PS (■) 45 nm (▲) 200 nm and PS 45 nm/PN at different PN thickness: (△) 10 nm, (b) (▽) Mode 1 and (▼) Mode 2 of 20nm, and (◇) Mode 1 and (◆) Mode 2 of 30nm. In (b) the solid line represents the VFT curve (Eq. 2.1.1) of PS bulk with the parameters of $\tau_0 = 10^{-13.2}$ (s), B = 1767.2K, and T_0 = 276.8K . All data was measured at $q_{||} = 0.78\times10^{-2}(nm^{-1})$. The data of PS45, PS200, and PS bulk are adapted from Vianna's Ph.D. works.[57]

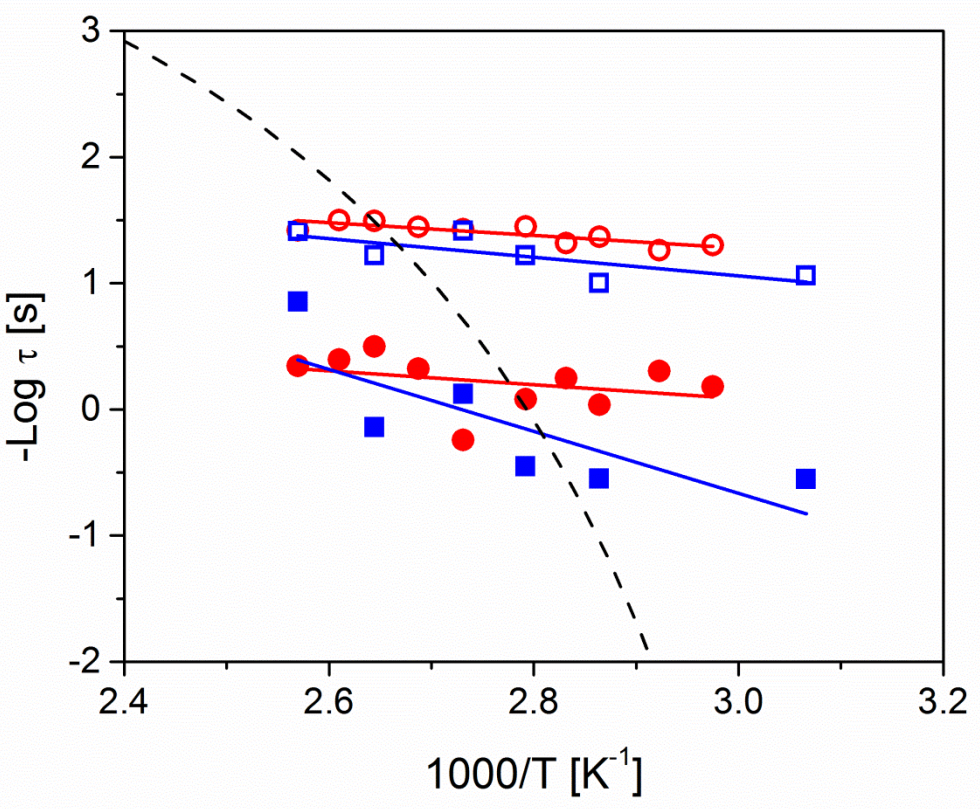

FIG. 4.2.6. Arrhenius plot of PS/PN 20 nm at $q_{\parallel}$ =0.78×10^{-2}(nm^{-1}) at different PS thickness: (○) Mode 1 and (●) Mode 2 of 45nm, and (□) Mode 1 and (■) Mode 2 of 65nm. The dashed line represents the VFT fitting curve of the PS 45 nm without PN as a capping layer. The solid (red and blue) lines are fitted by Arrhenius equation. The fitted activation energy (E_a) of Mode 1 (Mode 2) of PS45PN20 and PS65PN20 are 9.7 kJ/mole (10.5 kJ/mole), and 14.1 kJ/mole (47.0 kJ/mole), respectively. The data of PS45 is adapted from Vianna's Ph.D. works.[57]

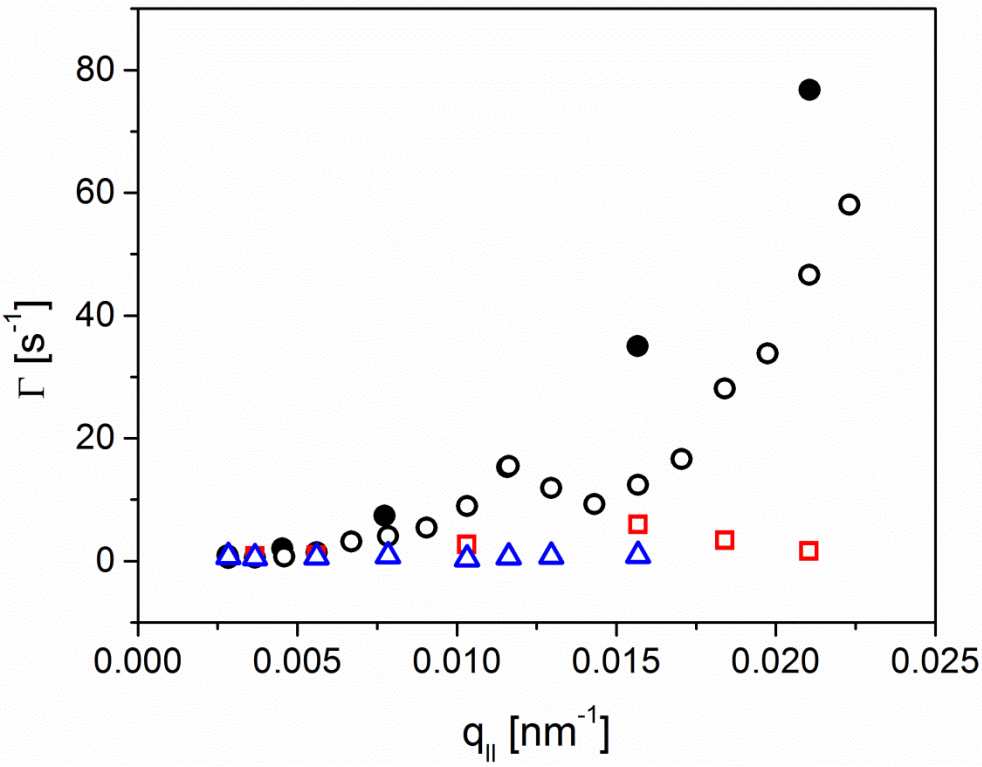

FIG. 4.2.7. The $q_{||}$-dependence of the mean relaxation rate Γ for (●) PS 45 nm (black dashed line) and Mode 2 of PS 45nm/ PN at 366K at different PN thickness: (○) 10 nm, (□) 20 nm, and (△) 30 nm. The data of PS45 is adapted from Vianna's Ph.D. works.[57]

To examine the contribution of the PS layer to the signal, in cooperation with the group of Professor Dr. Friedrich Kremer at the Leipzig University, dielectric spectroscopy measurements were conducted by this group on samples we prepared. The dielectric data shows that the α-relaxation of the PS 45 nm is close to the bulk PS but seems to be somewhat faster – this could be due to measuring different observables in dielectric spectroscopy and in mechanical spectroscopy. Another possibility is that the faster segmental motions are induced by the density fluctuation of polymer chains adjacent to the substrate [143]. This density fluctuation close to the substrate influences the dynamics of the thin film more with decreasing film thickness. The PS45PN30 follows a similar VFT curves as the PS 45 nm and bulk PS (**FIG. 4.2.8**) but is faster than the bulk PS. This indicates the α-relaxation is probably not affected by the film thickness, which is consistent with previous studies[7,11] of the Kremer group. Hence, for the Mode 1 and Mode 2, we can neglect the contribution from the α-relaxation of the PS layer to the signal.

Our current results are in good agreement with the previous work[24] where it was found that there is no T_g shift without a free surface. The PS thin film used here is confined between PN and gold substrate, meaning that a free surface of the PS facing to the air does not exist. Since the α-relaxation is a main indicator for T_g because it is the motion of polymer segments, the not changing α-relaxation in our experiment agrees with a not shifted T_g. However, it should be noted that the fluorescence studies[9,144] show different results.

In cooperation with the group of Dr. Eichhorn at the Leibniz Institute of Polymer Research Dresden , temperature dependent ellipsometry experiments were performed on samples prepared by us by our preparation method. T_g of 326K for PS 45 nm and PS45PN20 measured by the ellipsometry (**FIG. 4.2.9**) are the same as the bulk PS measured by differential scanning calorimetry. As is shown above, T_g is dictated by the α-relaxation and vice versa, and the α-relaxation does not change in the thin film or bulk (**FIG. 4.2.8**). From this, we may expect that there is no shift of T_g observed in the ellipsometric measurement. This was observed in the ellipsometry measurement, indicating that our conclusion obtained from dielectric spectroscopy and ellipsometric measurement is consistent. Furthermore, no shift in T_g also implies that the PS under the PN layer has not been cross-linked during plasma polymerization process of norborene on top of the PS surface.

When the polymer is cross-linked, the polymer chains are confined in smaller spaces than in the not cross-linked situation. The activation or Arrhenius plot of cross-linked polymer shows the Arrhenius behavior but not VFT behavior[145]. But it was reported[109] that plasma polymerization generated tiny cross-linked part between the PS and PN layers. This hints to the conclusion that the signal of Mode 1 and Mode 2 may be contributed from the PS/PN interface.

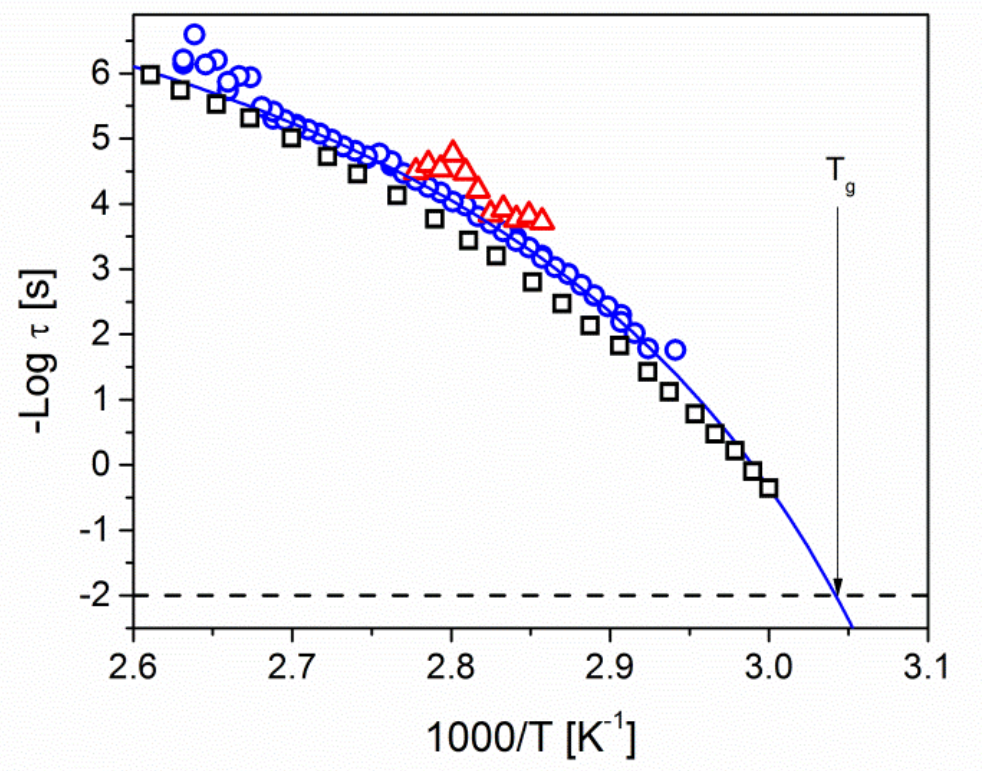

FIG. 4.2.8. Arrhenius plot of (□) PS Bulk, (○) PS 45 nm, (△) PS45PN30. The PS bulk is measured by rheometer in a dynamic mechanical spectroscopy experiment[57] and the PS 45 nm and PS45PN30 were measured by dielectric spectroscopy. The solid line represents the VFT curve of PS 45 nm measured by dielectric spectroscopy.

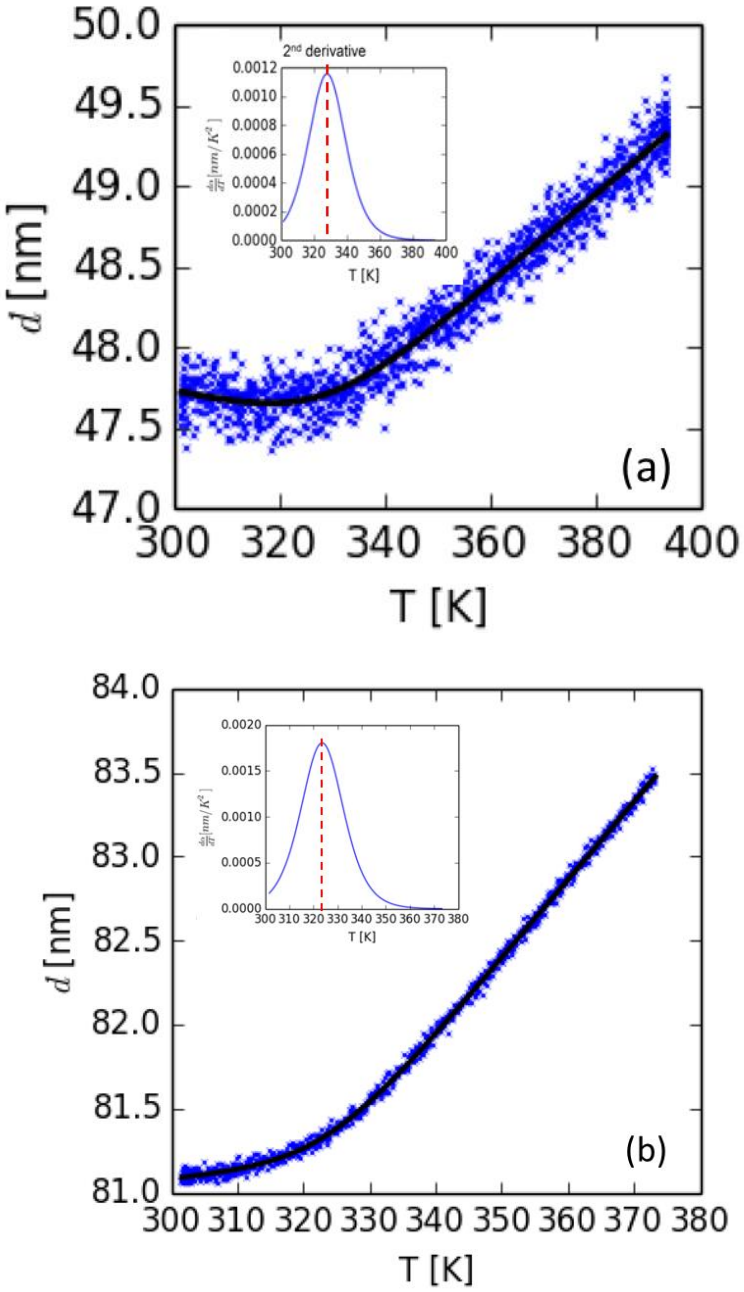

FIG. 4.2.9. The film thickness measured by ellipsometry as function of temperature for (a) PS 45 nm and (b) PS45PN20. The insets show the second derivatives of the temperature dependent film thickness to determine precisely T_g. The black solid lines represent the fitting lines, and the red dashed lines mark the T_g.

4.2.2 Discussion

The above results **(FIG. 4.2.8** and **4.2.9**) indicate that the contribution of α-relaxation of the PS for Mode 1 and Mode 2 can be excluded from the signal we observe. These modes show Arrhenius, i.e. thermally activated, behavior. This is an indication for a local mode. However,

the β-relaxation of the glass transition (cp. **section 2.1**) is one of the possible explanations for the signal since the Mode 1 and Mode 2 show an Arrhenius curves which is typically found for the β-relaxation process. Compared to the literature[141,142,146], both of the Mode 1 and Mode 2 locate in the range of 0.001 s to 10 s which is considered to be dominated by β-relaxation. The β-relaxation can be found below T_g. When the temperature is above T_g, the β-relaxation disappears or merges into the α-relaxation. However, both Mode 1 and Mode 2 can be observed below T_g and extend over T_g (**FIG. 4.2.5** and **4.2.6**). In some cases the β-relaxation is regarded as the side chain rotation[64] or side chain motion in general. In terms of polarization, dynamic light scattering with the geometry of the incident orthogonal polarized to the scattered light can capture the rotational motion (**Section 3.2**)[96,147]. But, for our PS thin films, we cannot see any depolarized signal in the correlation functions. That indicates that rotation motion has only negligible contribution to the Mode 1 and Mode 2.

The fragility index m, is defined as $m= d(\log \tau)/d(T_g/T)$ and determined at T_g[67,148]. Because our curves, $\log \tau$ is very insensitive to the temperature, T_g/T (**FIG. 4.2.6)**, the index m can be considered as the average slope of different temperature. In the literature[140], the segmental dynamics of polymers which refers to the motions of two to three polymer segments confined in the nanoporous alumina (AAO) shows a so called “fragile” dynamic behavior when the diameters of AAO are 200 and 400 nm. When the diameter of AAO is below 65 nm, the segmental dynamics changes to the “strong” dynamic behavior. The AAO diameter of 65 nm is a critical value for this fragile-to-strong transition. This means if the confined space is small enough, the dynamics inside the polymer chains will be affected. Our results (**FIG. 4.2.5** and **4.2.6**) show a similar transition as reported in the literature[140], but do not show the typical α- and β-relaxation behavior. The activation energy of Mode 2 increases with the thickness of the PS increasing (**FIG. 4.2.6**). Hence, the Mode 2 can be attributed to a contribution from the suppressed capillary wave. The stored energy is caused by the fluid deformation. When the shape of the wave is deformed, the energy is dissipated into the PS layer. The specific motion

which cannot be found in the bulk possibly arises from the interface of polymer/polymer or polymer/air[149]. Like internal waves in the ocean[150,151], if there is a surface tension fluctuation at or in the PS/PN interface, the capillary wave can still exist there[76].

Addressing the question why we see Mode 1 and Mode 2 as local modes one can use in analogy to the α-process of the glass transition the fragility index m as an indication for characteristic length scales. m of Mode 1 of PS45PN20 and PS65PN20 are 1.5 and 2.3, respectively. Recently the dynamics of CRR in thin films was shown[125]. According to the literature[66,68], the fragility index is proportional to the size of the CRR (V) which is introduced by Adam and Gibbs[65]. The fragility index and volume of CRR of bulk PS are reported as 139 and 15.6 (nm^3)[148,152], respectively. By using the Adam and Gibbs[65] relation of the CRR, $V= \xi^3$, the volume of CRR of Mode 1 can be estimated to 0.2 nm^3 with the characteristic length ξ of 0.6 nm. The activation energy of Mode 1 is about 10 ~ 14 kJ/mol. Its activation energy is less than the value of E_a ~ 60 kJ/mol of β-relaxation[141]. Larger activation energy is related to a bigger size of the CRR[68]. This indicates the energy barrier the Mode 1 has to overcome is even less than the side chain rotation.

In another words, the length scale in which the polymer chains with the Mode 1 can move is smaller than that for side chain rotation. For Mode 2 of PS65PN20, the index m is about 7.5, and the characteristic length ξ can be estimated as 0.9 nm. The CRR of Mode 2 can be calculated as 0.7 nm^3 by using the Adam-Gibbs relation expressed above. On the other hand, the characteristic length ξ ranges from 1 to 4 nm near T_g[9,153], giving the CRR of 1-64 nm^3. Thus, the CRRs of Mode 1 and Mode 2 are not large enough to affect the CRR near T_g. Hence, it will be reasonable to anticipate that T_g of PS/PN samples is very similar to T_g of the bulk PS. This fact also hints the properties of the Mode 1 and Mode 2; since the Mode 1 and Mode 2 are not related to the bulk properties, these modes should arise from an extremely confined environment such as the PS/PN interface.

The PN layer is assumed to be immobile in our experimental time scale (> 100 s). As discussed above, both α- and β-relaxation can be excluded from the signal. At the PS/PN and Au/PS interface, the layers are influenced by strong, attractive interactions (see **Section 3.1**), and thus a possible slip effect is negligible. As also discussed above, the Mode 2 can be assumed to be induced by the suppressed capillary wave. The dynamic length scale of Mode 1 is around the scale of 4~5 polymer segments. However, Hu et. al[134] reported that mixed PS/PBrS layer is present at the interface of the PS/PBrS bilayer system and showed extremely low viscosity. This means that the mixed layer is very mobile. Furthermore, other studies[10,12,15,17,26] have reported that there is a more mobile layer existing at the surface of the thin film. As shown in **Section 4.1**, the surface of PB thin films has extremely low viscosity[123].

4.2.3 Summary

In this section, we characterized the capillary wave and its suppression of the PS/PN bilayer by using the REDLS. The data show that the capillary wave at the PS surface confined between the gold substrate and PN when the thickness of PN 20 nm and more. In this strongly confined polymer sample of PS/PN bilayer, the PS shows a Arrhenius behavior even above T_g. In contrast to the single-exponential decay found in the PS layer, the measured correlation function in the confined PS/PN bilayer shows bi-exponential decay mode. This can be well accounted for by using the theoretical model of multi-decay in the viscoelastic layer and bilayer[149]. We demonstrated that the α-relaxation is not affected by the confinement, whereas the dynamics of polymer chains near the interface is strongly affected. This is in a good agreement with the literature[154]. Our data also implies that due to the strong attractive force acting on the PS/PN interface, the interface plays an important role like PS and PN layers, and contributes to the dynamics of the thin film.

4.3 Polystyrene thin films anchored to gold by thiol group

Evan et al.[13] explored the surface dynamics of a PS top layer in bilayer films and found that the dynamics of the bilayer can be adjusted by changing the modulus of the sub-layer. When the temperature is ~10K above the T_g of the PS top layer, the shorter relaxation time of PS top layer with lower modulus sub-layer was shown, especially at the low in-plane scattering wave vector (larger probing length scale). In addition, the relaxation time of PS top layer increases significantly with decreasing PS top layer thickness. When the temperature is 40K above the T_g of PS, the faster relaxation induced by the softer sub-layer and the stronger confinement effects with decreasing thickness are neglected.

To get a better insight into the effects of confinement imposed by the solid substrate we changed the interaction between the solid substrate and the polymer thin film by putting an anchor for the film to the substrate. This anchor consists of covalently bound PS by thiol groups as end groups of the PS.

When the PS surface is capped by the PN layer, multi-mode decays emerge in the correlation functions. As is clarified in the **Section 4.2**, Mode 2 is inferred as to be contributed from the suppressed capillary wave of the PS. The Mode 1 of the PS/PN samples follows a Arrhenius curve and can be found below T_g. The emergence of the Arrhenius curve for the Mode 1 indicates that Mode 1 is weakly temperature dependent and has the relatively small energy barrier. Also from the discussion in Chapter 4, the dynamic length scale of the Mode 1 is around the scale of 4~5 polymer segments, and should arise from the PS/PN interface. Thus, we can attribute the origin of the Mode 1 to the local motion at the PS/PN interface.

By measuring the capillary wave with XPCS[7,41], the surface viscosity of PS thin film was found to be similar to the bulk PS. However, there is a more mobile layer with low viscosity claimed to be at the surface of PS thin films[16]. For the PS thin film, an Arrhenius curve has been reported[10,146] below T_g while above T_g, this Arrhenius curve disappears and/or merges

into the VFT curve. As the discussion about the Mode 1, this Arrhenius curve can be seen as the thermal behavior of local motion. As such, it is reasonable to infer the more mobile layer to be contributed from other kinds of the motion such as the local motion rather than capillary waves. This inference can be supported by the reduction of local viscosity[31].

The contribution of the Mode 1 to the signal is assumed to be so tiny that Mode 1 cannot be measured by REDLS and is hidden in the noise of the strong signal of the capillary wave. Although the theoretical studies[149,155] predicted that multi-mode decays are present at the single viscoelastic layer and the bilayer e.g. PS thin film and PS/PN thin film, whether a decay can be observed or not really depends on the amplitude of the mode. Thus, the key point is that the amplitude of the Mode 1 should be increased if possible or to lower or diminish the amplitude of capillary waves as we did in the case of PS/PN to enable us to receive the signals from the Mode 1.

Since the capillary wave is influenced by the properties of the viscoelastic layer[46], we want to increase viscoelasticity of the PS layer by enhancing the confinement form the substrate. To do this, we grafted the PS with a thiol end group (PS-SH) to the gold substrate, giving rise to an increase in the viscoelasticity of the PS layer. This PS-SH forms an anchor to the PS spin-coated subsequently and changes the adhesion and interaction of the PS with the substrate.

4.3.1 Results and discussion

Besides van der Waals force, there is no special interaction between the Au interface and PS. After modifying the interface by grafting PS-SH, the binding of the interface to PS becomes stronger.

Producing our films with unchanged experimental procedures as spinning speed and concentration of the polymer solution, we found that the film thickness increased about 10 nm on the Au interface modified by PS-SH. If the substrate becomes more binding to the PS in the sample solution, more PS will be attached to the substrate at a fixed spinning-speed. Thus, the

increasing thickness at a fixed spinning-speed gives us the message that the confinement between the Au and PS was enhanced.

To check for the attachment of PS-SH we performed AFM. All the samples were measured with contact mode at 298K under 1 atm in air (Dimension 3100, Digital Instruments). The small protrusion-like structures (**FIG. 4.3.1c, d**) are the PS-SH. PS-SH can be checked by the AFM phase image (**FIG. 4.3.1d**). The molecular weight of our PS-SH is 3000 g/mole, and thus its radius of gyration (R_g) is about 2 nm[106]. The profile (**FIG. 4.3.2b**) shows the height difference equals to 2 nm, which is another evidence to confirm that the protrusions are PS-SH.

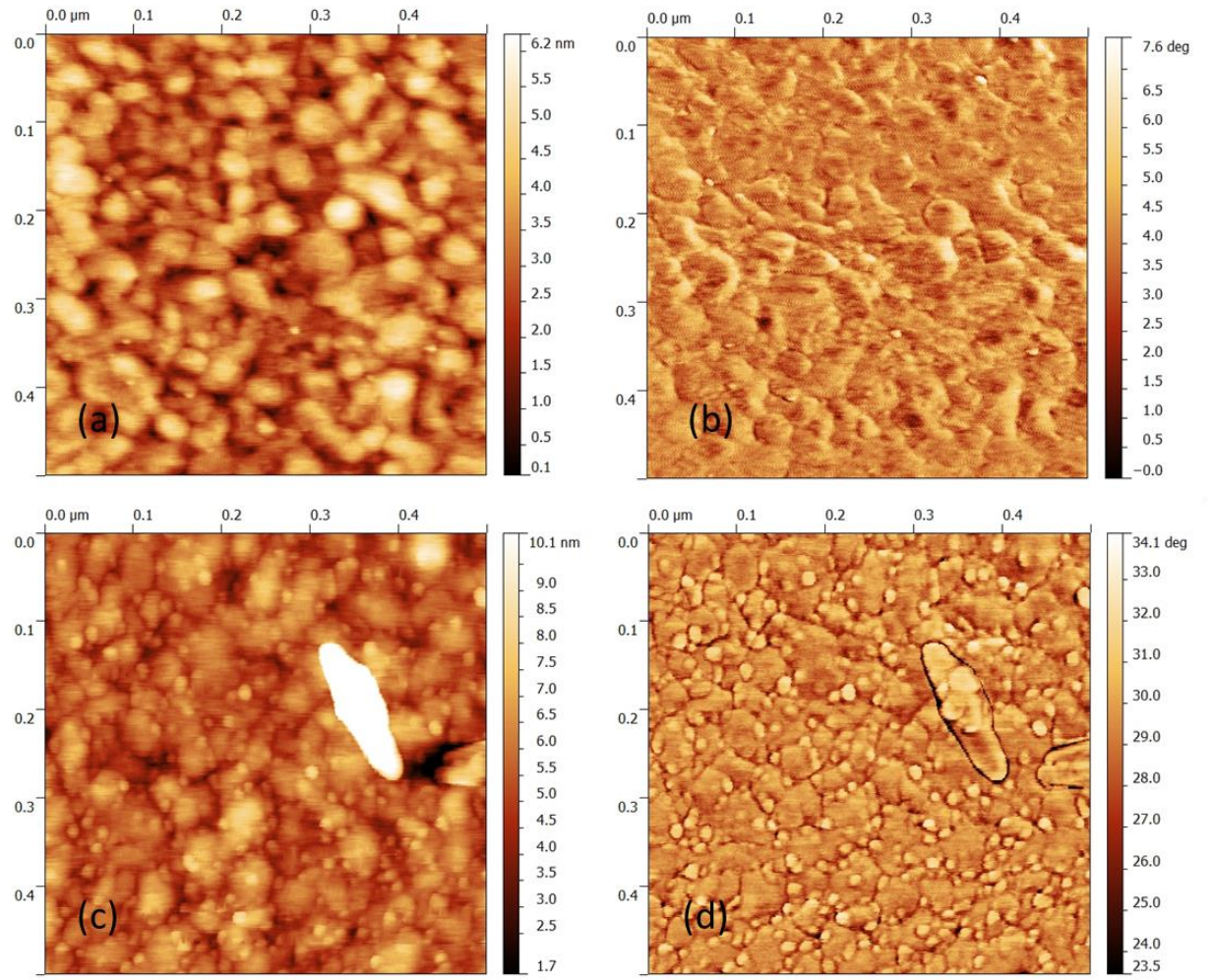

FIG. 4.3.1. AFM measurement (500nm×500nm) at 298K for pure Au: (a) topography image (b) phase image. PS-SH grafted to Au: (c) topography image (d) phase image. Comparing (a) and (c), there are protrusion-like structures shown on the Au substrate after grafting the PS-SH. This can be confirmed by the (d) since the PS-SH shows a different phase compared to the Au substrate. The white and shiny spot in the (c) could be stemming from small impurities in the solvent.

The Au layer was evaporated to the glass directly, and is composed of many different Au facets inside (**FIG 4.3.1a, b**). Since thiol groups strongly graft to the [111] facets [156-158], the PS-SH are only located at specific areas of the Au surface (**FIG. 4.3.1c, d**).

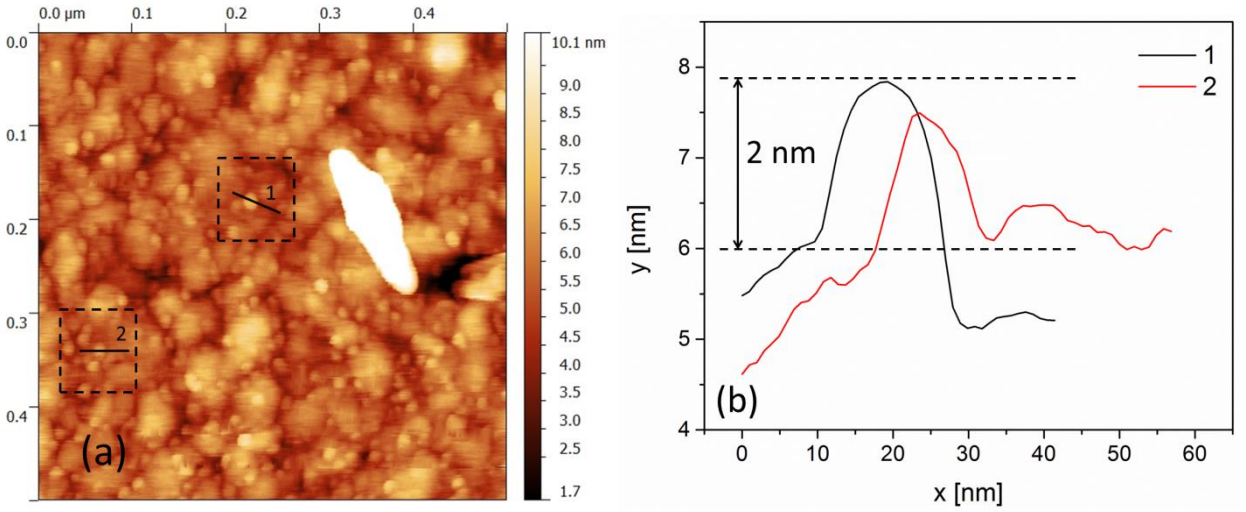

FIG. 4.3.2. AFM measurement (500nm×500nm) at room temperature (a) for topography image of PS-SH anchored to Au (b) profiles for the marked position 1 and 2.

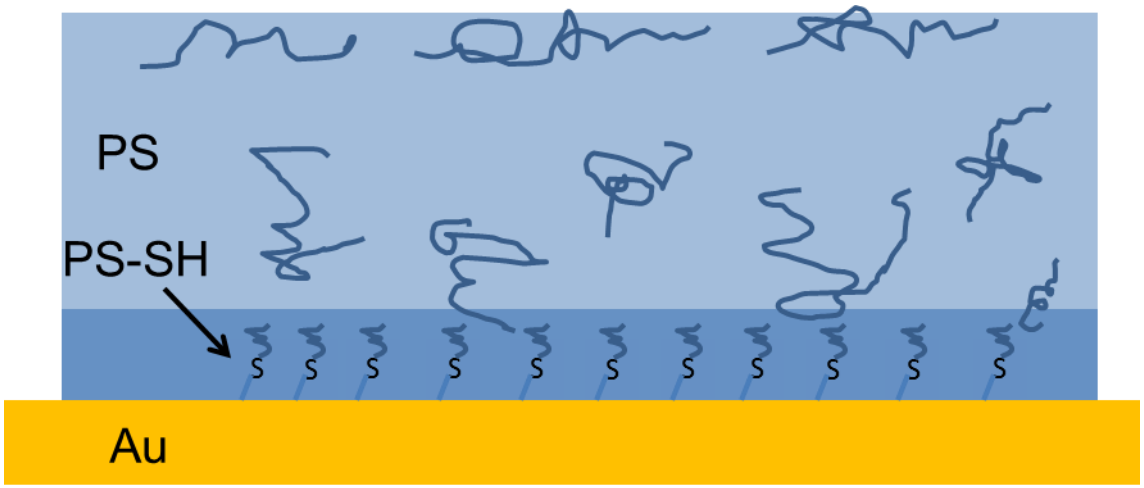

FIG. 4.3.3. Schematics for Au which is modified by the PS-SH, and the PS layer is spin-coated on the top of the PS-SH. The dark blue represents the PS layer here is less mobile.

The PS 35 nm grafted to gold substrate shows the Arrhenius behavior at $T < T_g$ and $T > T_g$+30K (**FIG. 4.3.4**). The time scales of Mode 1 and Mode 2 coincide with the temperature region of $T > T_g$+30K and $T < T_g$, respectively (**FIG. 4.3.4**). At $T_g < T < T_g$+30K, the PS thin

film changes from the glassy state to the rubber state with increasing temperature. During this phase transition, the polymer chains have to overcome a higher energy barrier, and this is related to the larger size of the CRR. Hence, the dynamics of thin film is dominated by the capillary wave. Compared to the PS 45 nm, the PS-SH/PS35 the relaxation changes from VFT to Arrhenius dependence. This indicates that this mode of the PS-SH/PS35 moves locally because of the strong confinement from the substrate. Over T_g + 30K, the dynamics of capillary wave synchronized with the Mode 1. In the high T region, the cooperative length are also reduced[146]. Decreasing cooperative length and increasing in confinement lowers the amplitude of capillary wave, and makes the Mode 1 observable[149]. The PS-SH results fit with the assumption about Mode 1. That manifests that the Mode 1 arises from the local motions at the surface of the PS thin film.

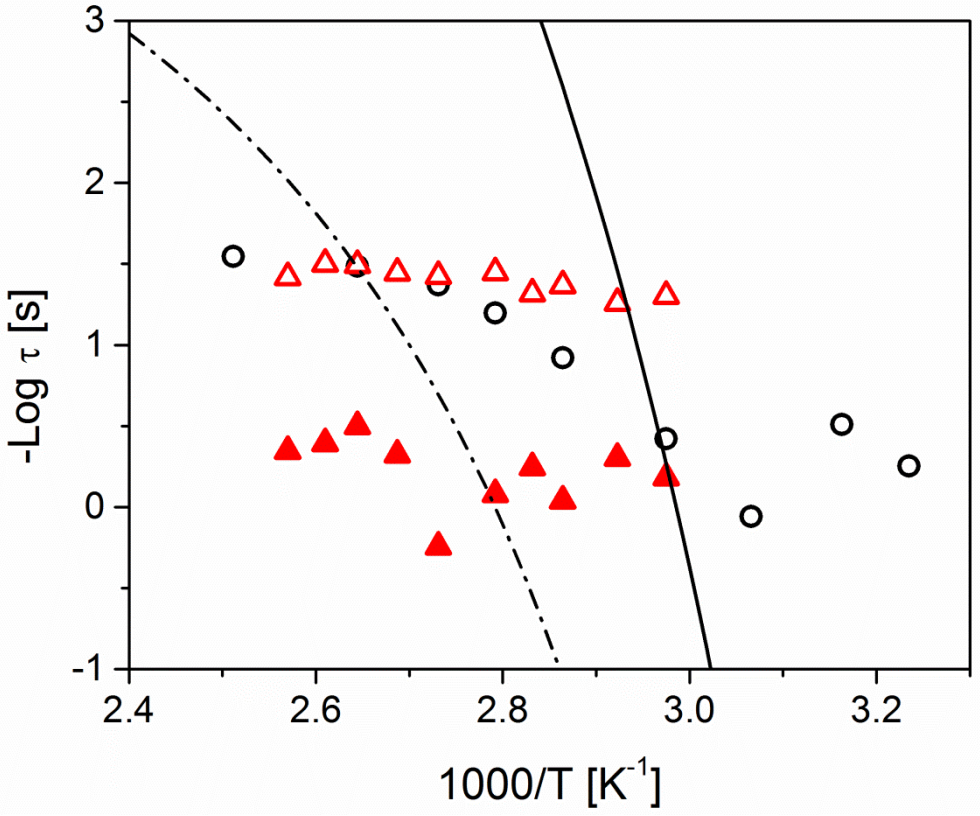

FIG. 4.3.4. Comparison between films with PS capped by PN and the thiol anchored PS films. Arrhenius plot measured at $q_{||} = 0.78 \times 10^{-2}(nm^{-1})$ of (O) PS-SH/PS35, and (△) Mode 1 and (▲) Mode 2 of PS45PN20. The dash-dot and solid lines represent the VFT curve of the capillary waves of the PS 45 nm and the bulk, respectively. The data of PS45 and PS bulk are adapted from Vianna's Ph.D. works.[57]

The chain dynamics which corresponds to the end-to-end vector of polymer chains or of terminal sub-chains are strongly affected by their boundary condition[154]. But the segmental dynamics which length scale is referred to two to three polymer segments and hindered in the bulk part of thin film is not affected by the boundary condition. The free end groups of chains exist at the edge of polymer thin film[1]. These free end groups should move locally. The Mode 1 in our work might be referred to the motions of free end group at the edge.

The relaxation time of PS-SH/PS85 thin film decreased with increasing temperature (**FIG. 4.3.5**). This trend is as predicted by the capillary wave model[2,20] since the surface tension decreases with increasing temperature.

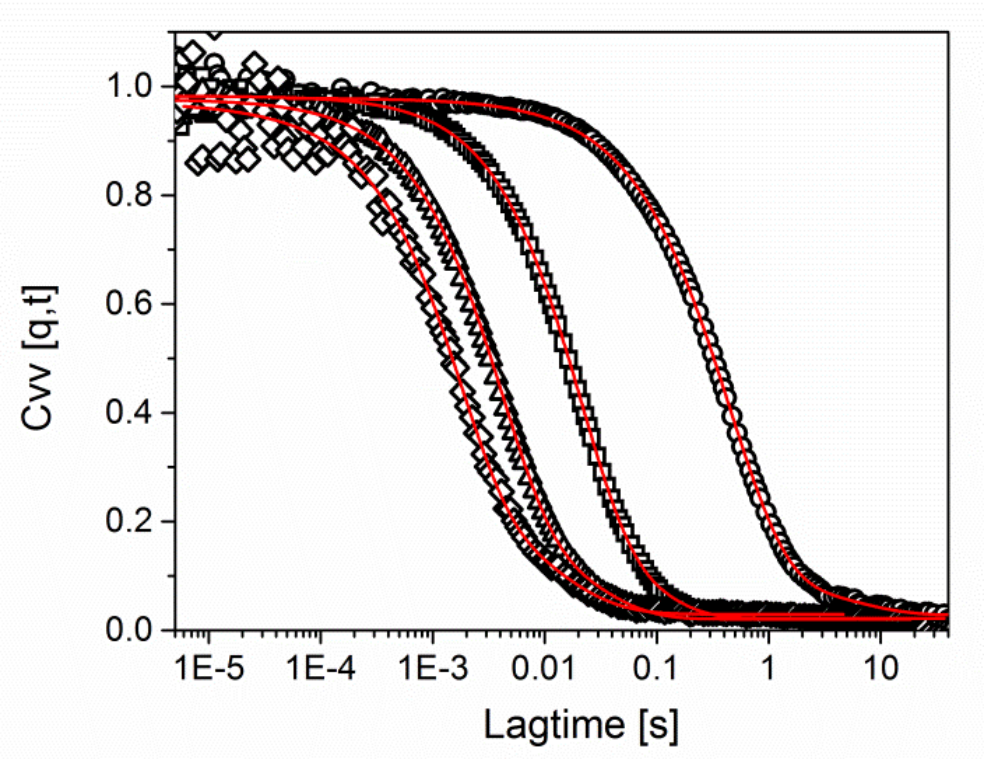

FIG. 4.3.5. Normalized, heterodyne auto-correlation functions for PS-SH/PS85 at $q_{\|} = 0.78\times10^{-2}$ (nm^{-1}) and different temperatures: (O) 366K, (□) 378K, (△) 389K and (◇) 398K. The solid (red) lines are fits by KWW functions.

The PS-SH/PS65 shows the Arrhenius behavior at the temperature over T_g + 30K **(FIG. 4.3.6)**. When the PS thickness increases to the 85 nm (PS-SH/PS85), the VFT curve is shown at the temperature over T_g + 30K **(FIG. 4.3.6)**. That represents the capillary wave is not suppressed by

the confinement from the substrate. When the thin film becomes thicker, the surface is away from and less confined from the substrate. Below T_g, there are Arrhenius curves like the Mode 1 in the PS/PN samples. The relaxation time of these Arrhenius curves decrease with increasing thickness. Hence, these Arrhenius curves should originate from the surface and represent the local motion.

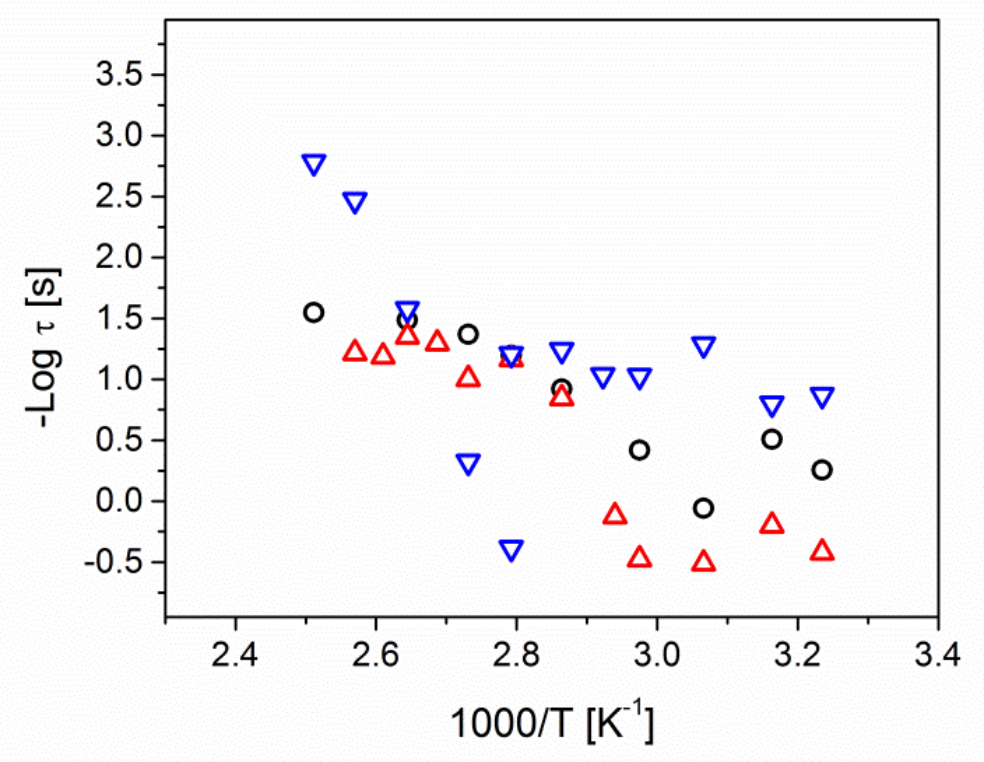

FIG. 4.3.6. Arrhenius plot, $q_{\|}$ =0.78×10^{-2}(nm^{-1}), of PS-SH/PS at different PS thickness: (O) 35 nm, (△) 65 nm and (▽) 85 nm. For PS-SH/PS85, the VFT curve is shown from T_g + 30K. For PS-SH/PS35 and PS-SH/PS65, the VFT curves are shown from T_g to T_g + 30K.

The relaxation time decreases with increasing scattering wave vector in the region $q_{\|}$ > 0.56 x 10^{-2} nm^{-1}(marked by vertical dashed line) (**FIG. 4.3.7**). This trend is consistent with the prediction of the capillary wave model. In the region of $q_{\|}$ < 0.56 x 10^{-2} nm^{-1}, the relaxation time does not show the $q_{\|}$-dependent behavior due to the enhanced confinement from the substrate. This transition can be thought as a transfer from internal interaction dominated (high $q_{\|}$, which is referred to smaller probing length scale) to a substrate dominated regime (low $q_{\|}$, which is referred to larger probing length scale)[123]. The transition is not related to the modulus of the

thin film itself since PS-SH/PS85 shows the same transition $q_{||}$ at different temperature. Compared to the literature[123], this transition shifts to lower $q_{||}$ because the enhanced confinement. That also means the enhanced confinement from the substrate does not affect the internal interaction of polymer chains (high $q_{||}$).

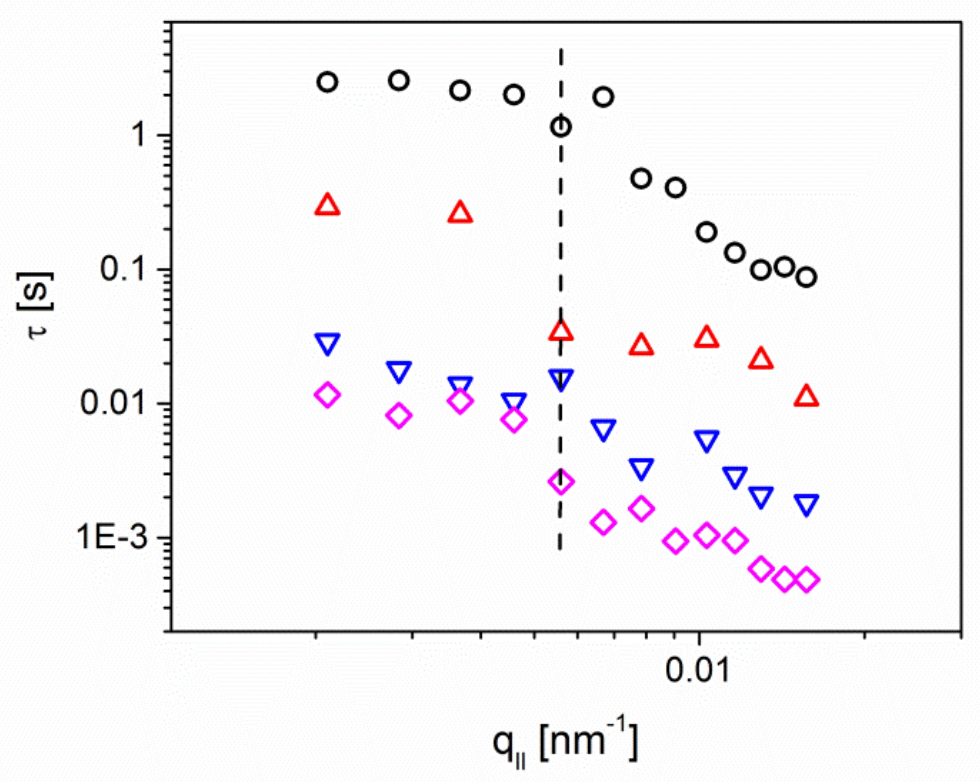

FIG. 4.3.7. $q_{||}$-dependent relaxation time of PS-SH/PS85 at different temperature: (○) 366K, (△) 378K, (▽) 389K and (◇) 398K.

The viscosities of the PS-SH/PS85 obtained from the fit decreased with increasing temperature (**FIG. 4.3.8b**). Their value was higher than bulk value about half order. According to the literatures[7,41], the viscosity of PS thin films should be the same as the bulk. Hence, the bulk viscosities of different temperatures were regarded as defaults in the capillary wave model to fit and get the related effective thickness (**TABLE 4.3.2**). The effective thickness is defined as the thickness of the part of the thin film contributing to the capillary wave motion according to the fit result. The effective thickness is about 30 nm at all temperatures (**FIG. 4.3.9b**). 85 nm of PS was spin-coated on the Au modified by PS-SH. Therefore there is about 55 nm thick PS layer strongly confined by the substrate and which effectively does not contribute the dynamics of

capillary wave. This is in a good agreement with the Arrhenius behavior shown by the PS-SH/PS65 (**FIG. 4.3.6**). The capillary wave of PS is strongly confined by the substrate up to 65 nm thick. In other words, there should be 55-65 nm of less mobile layer adjacent to the Au modified by PS-SH.

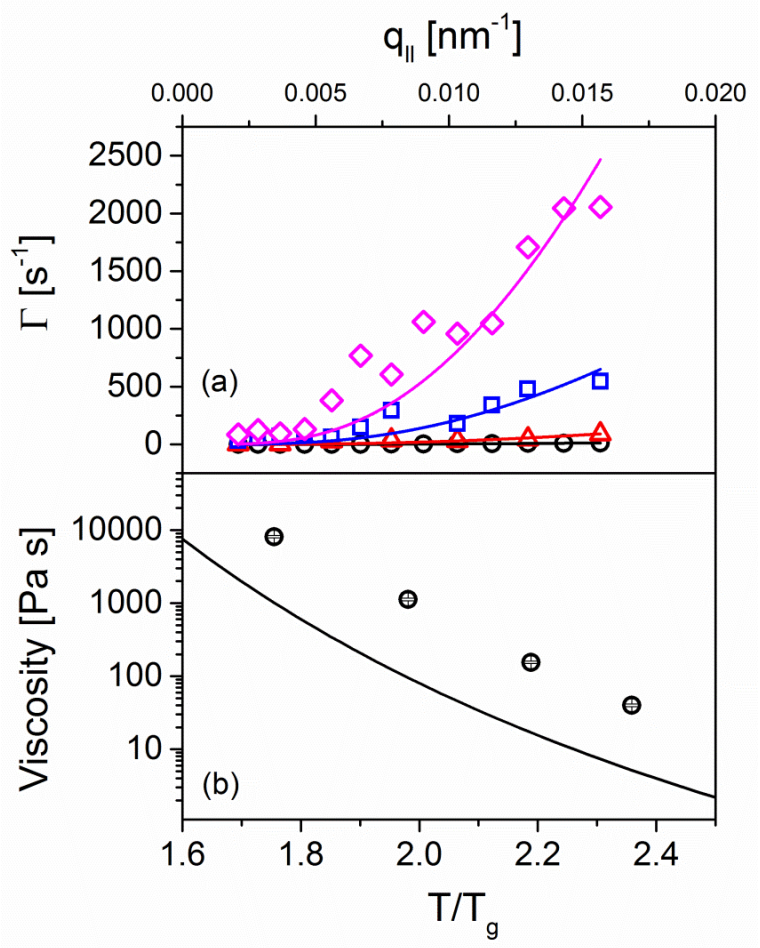

FIG. 4.3.8. (a) The $q_{||}$-dependence of the mean relaxation rate Γ for PS-SH/PS85 at different temperatures: (O) 366K, (△) 378K, (□) 389K and (◇) 398K. The solid lines represent least-squares fits based on the capillary wave model[7] represented by Eq. 3.1. (b) Comparison of viscosities: (O) from fits of the capillary wave model. The solid, black line represents the bulk viscosity[57]. The experimental error in viscosity is up to 4%.

TABLE 4.3.1. Viscosity η of PS-SH/PS85 vs. temperature obtained from the capillary wave model fits in **FIG. 4.3.8a.** Surface tension γ was taken from ref.[120].

T (K)	h (nm)	γ (mN/m)	η (Pa s)
366	85	35.4	8128.3
378	85	34.5	1127.7
389	85	33.7	155.1
398	85	33.1	40.1

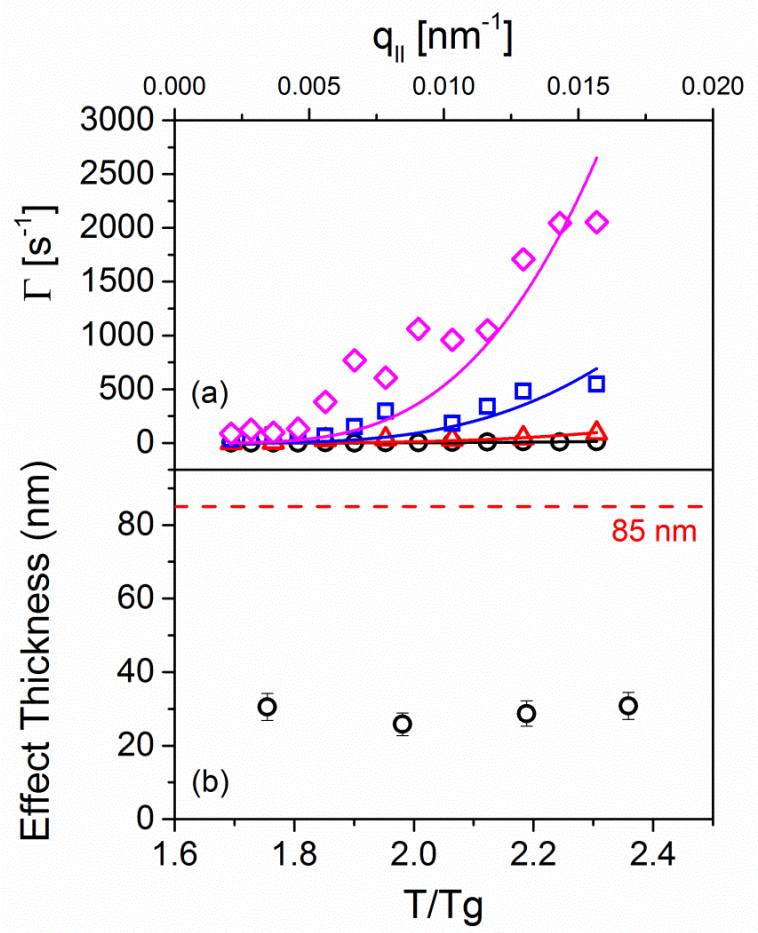

FIG. 4.3.9. (a) The $q_{\|}$-dependence of the mean relaxation rate Γ for PS-SH/PS85 at different temperatures: (O) 366K, (△) 378K, (□) 389K and (◇) 398K. The solid lines represent least-squares fits based on the capillary wave model[7] represented by Eq. 3.1. (b) (O). Effective thickness from fits of the capillary wave model. The red, dashed line represents the real thickness of PS. The error in effective thickness is up to 12%.

TABLE 4.3.2. Effective thickness h^{eff} of PS-SH/PS85 vs. temperature obtained from the capillary wave model fits in **FIG. 4.3.9a.** Surface tension γ was taken from ref.[120].

T (K)	Bulk η (Pa s)	γ (mN/m)	h^{eff} (nm)
366	1016.5	35.4	30.5
378	95.6	34.5	25.8
389	17	33.7	28.7
398	5.2	33.1	30.8

4.3.2 Summary

In this study, experiments on Au substrate modified by PS-SH which have been covered by spin-coating with a PS layer on top are evaluated. By using the preparation method mentioned above, the confinement from the substrate is enhanced, and the capillary wave is suppressed by that. Since the amplitude of capillary wave is lowered by enhanced confinement from the substrate, the Mode 1 which is discussed in Chapter 4 has been confirmed to originate from the local motion at the surface of the PS thin film. The capillary wave is strongly confined in the larger probing length scale (low $q_{//}$). The effective thickness which really contributes to the capillary wave is less than the real thickness of PS on the top of the substrate. Because the confinement from the substrate is enhanced, the length scale of less mobile layer adjacent to the substrate increases. This viscoelastic layer does not contribute to the motions of capillary wave, and makes the viscosity of PS-SH/PS samples increasing. As such, we demonstrated that the surface dynamics can be tuned by the interaction between the substrate and polymer which can be change by modifying the substrate.

Chapter 5

Conclusion

In this thesis, the noninvasive and marker-free experimental method REDLS was employed to measure the dynamics of polymer thin films of which capillary waves were the most prominent ones. Based on a study of the capillary waves of PS thin films[57], we want to go further to investigate how capillary waves behave in different confinement situation and temperature region, e.g., close to the T_g or far above T_g in low viscosity, liquid-like thin films. Thus, three different systems have been measured:

(1) Low viscosity, liquid-like thin film, PB, at temperature of T_g + 125K

(2) PS/PN bilayers, measured at temperature close to T_g in order to study the capillary waves of PS thin films strongly suppressed by a glassy PN layer.

(3) PS thin films anchored to the substrate of gold by thiol group to enhance the confinement from the substrate to suppress the capillary waves to figure out the possible motion modes of polymer chains at the thin film surface.

In the first part of my thesis, I measured capillary waves of the PB thin films in different wave vectors and thicknesses. A three layer model to explain the dynamics of polymer thin films changing with thickness was introduced to explain the findings. I also showed that the effective length scale of the confinement from the substrate is a fixed distance of about 20-25 nm not related to the $3R_g$ postulated in literature before.

The three layer model proposed is composed by: a less mobile layer compared to the mobility in the same bulk polymer adjacent to the substrate, a more mobile layer at the polymer/air surface, and the remaining bulk part. The viscosity of polymer thin film at different thickness is determined by the ratio of less mobile, more mobile, and bulk layer. The three layer model means the polymer thin film is heterogeneous and shows a distribution of dynamics which is

qualitatively in agreement to a prediction by de Gennes[1]. The influence of less mobile and more mobile layers makes the dynamics of polymer thin film different from the bulk as seen by most experiments observing the film as a whole as e.g. dielectric spectroscopy.

In the second part of my thesis, a glassy PN layer was polymerized on the top of PS thin film directly by plasma polymerization to suppress capillary waves by this capping. I found that the thermal behavior of capillary waves is changing from a non-Arrhenius behavior to Arrhenius behavior. When we put PN layers with thickness over 20 nm on the top of the PS thin film, capillary waves are strongly suppressed by this solid, glassy PN layer. The amplitude of capillary waves is lowered because of this strong suppression. But, we found that the T_g and the α-relaxation of our polymer thin films are not affected by the PN layer and are similar to the bulk.

This lowered amplitude is what makes it possible to observe a local motion which relaxation time is shorter than the capillary wave at the surface of polymer thin film. This local motion is faster than the α-relaxation and is also not affected by the confinement from the substrate or the thickness of PN layer.

In the third part of my thesis, I anchored the PS thin film to Au by thiol group. Through this enhanced confinement from the substrate, the thickness of the less mobile layer is enlarged and suppresses the capillary wave via a change in the viscoelastic behavior. If we do not change the interaction between the substrate and polymer to enhance or weaken the confinement from the substrate, the thickness of the less mobile layer at a temperature of T_g + 125K should be limited to a fixed distance not related to the $3R_g$. But, the substrate modified by the anchor molecules enhances the confinement and enlarges the effective length scale of the less mobile layer and increases the viscosity of polymer thin film. Hence, the dynamics of polymer thin film can be tuned by modifying the substrate.

The confinement from the substrate will induce a more dense layer of a few nm adjacent to the substrate[32,33] and thus this region has smaller free volume as reported in a combination of

molecular dynamic simulation and PALS[35]. This more dense layer of a few nm probably induces changes in the mobility and leads to the less mobile layer of 20-25 nm mentioned in the three layer model. But the connection of the more dense layer and the less mobile layer is still an open question.

Based on the above results and discussions, there are some unsolved questions of glass transition in nanoscale which need to be answered in the future.

First, polymer thin films show heterogeneous dynamics along the different depth rather than a simple homogeneous layer. The capillary wave model based on a homogeneous single layer is applied to get the viscosity of polymer thin film. Compared to the bulk, we get one order of magnitude lower viscosities in the PB thin films and half an order of magnitude higher viscosities in the PS-SH/PS thin films. A modification of the capillary wave model by considering the film to be composed of several layers seems to be necessary.

Second, the effective length scale of confinement from the substrate should be limited to few nm away from the substrate i.e., the thickness of dense layer is no more than 2 nm. However, the length scale of the less mobile layer is much more. Moreover, the less mobile layer affects the capillary wave of polymer thin film. What is the mechanism for the dense layer to become the less mobile layer? What is the long range relation between the capillary wave and less mobile layer?

Third, the more mobile layer is proven to exist at the surface of polymer thin films and the main reason inducing for the reported reductions of T_g with decreasing film thickness. But, what kind of motion induces the more mobile layer? What is the effective length scale of these motions contributing to the more mobile layer?

List of abbreviations

T_g	Glass transition temperature
η	Viscosity
PS	Polystyrene
h	Film thickness
AFM	Atomic force microscopy
NMR	Nuclear Magnetic resonance
M_w	Molecular weight
XPCS	X-ray photon correlation spectroscopy
R_g	Radius of gyration
PB	Polybutadiene
PI	*cis*-Polyisoprene
CRR	Co-operative rearrange region
$\xi(T)$	Temperature dependent length scale
REDLS	Resonance enhanced dynamic light scattering
PN	Polynorbornene
DLS	Dynamic light scattering
SPP	Surface plasma polariton
SPR	Surface plasma resonance spectroscopy
n_p	Refractive index of prism
n_d	Refractive index of dielectric medium
θ_c	Critical angle for total reflection
ε_p	Dielectric constant for prism
ε_d	Dielectric constant for dielectric medium

Γ	Relaxation rate
q	Scattering wave vector
n	Refractive index
λ	Wave length of incident light
k_i	Wave vector of incident light
k_s	Wave vector of scattered light
KWW	Kohlrausch-Williams-Watts equation
β	Stretching parameter
τ	Relaxation time
VFT	Vogel-Fulcher-Tammam
q_{ll}	In-plane scattering wave vector
PS-SH	Polystyrene modified by thiol group
rms	Roughness
E_a	Activation energy
m	Fragility index
V	Size of the co-operative rearrange region
γ	Surface tension
h^{eff}	Effective thickness

References

[1] P. De Gennes, The European Physical Journal E: Soft Matter and Biological Physics **2**, 201 (2000).

[2] S. Herminghaus, The European Physical Journal E: Soft Matter and Biological Physics **8**, 237 (2002).

[3] L. Yelash, P. Virnau, K. Binder, and W. Paul, Physical Review E **82**, 4, 050801 (2010).

[4] L. Yelash, P. Virnau, K. Binder, and W. Paul, Epl **98**, 5, 28006 (2012).

[5] S. Herminghaus, K. Jacobs, and R. Seemann, The European Physical Journal E **5**, 531 (2001).

[6] K. Ngai, The European Physical Journal E **8**, 225 (2002).

[7] H. Kim, A. Rühm, L. Lurio, J. Basu, J. Lal, D. Lumma, S. Mochrie, and S. Sinha, Physical Review Letters **90**, 68302 (2003).

[8] J. Keddie, R. Jones, and R. Cory, EPL (Europhysics Letters) **27**, 59 (1994).

[9] C. J. Ellison and J. M. Torkelson, Nature Materials **2**, 695 (2003).

[10] Z. Fakhraai and J. Forrest, Science **319**, 600 (2008).

[11] M. Tress *et al.*, Macromolecules **43**, 9937 (2010).

[12] K. Paeng, R. Richert, and M. Ediger, Soft Matter **8**, 819 (2012).

[13] C. M. Evans, S. Narayanan, Z. Jiang, and J. M. Torkelson, Physical Review Letters **109**, 038302 (2012).

[14] K. J. Alvine, Y. Dai, H. W. Ro, S. Narayanan, A. Sandy, C. L. Soles, and O. G. Shpyrko, Physical Review Letters **109**, 207801 (2012).

[15] Y. Chai, T. Salez, J. D. McGraw, M. Benzaquen, K. Dalnoki-Veress, E. Raphaël, and J. A. Forrest, Science **343**, 994 (2014).

[16] M. Ediger and J. Forrest, Macromolecules **47**, 471 (2013).

[17] K. Paeng, S. F. Swallen, and M. D. Ediger, Journal of the American Chemical Society (2011).

[18] J. Harden, H. Pleiner, and P. Pincus, The Journal of chemical physics **94**, 5208 (1991).

[19] J. Jackle and K. Kawasaki, Journal of Physics: condensed matter **7**, 4351 (1995).

[20] J. Jäckle, Journal of Physics: Condensed Matter **10**, 7121 (1998).

[21] J. H. Kim, J. Jang, and W.-C. Zin, Langmuir **16**, 4064 (2000).

[22] S. Kawana and R. A. Jones, Physical Review E **63**, 021501 (2001).

[23] O. Bäumchen, J. McGraw, J. Forrest, and K. Dalnoki-Veress, Physical Review Letters **109**, 55701 (2012).

[24] J. Sharp and J. Forrest, Physical Review Letters **91**, 235701 (2003).

[25] M. Y. Efremov, A. V. Kiyanova, J. Last, S. S. Soofi, C. Thode, and P. F. Nealey, Physical Review E **86**, 021501 (2012).

[26] Z. Yang, Y. Fujii, F. K. Lee, C.-H. Lam, and O. K. Tsui, Science **328**, 1676 (2010).

[27] G. Reiter, in *Glass Transition, Dynamics and Heterogeneity of Polymer Thin Films* (Springer, 2013), pp. 29.

[28] S. Herminghaus, R. Seemann, and K. Landfester, Physical review letters **93**, 017801 (2004).

[29] M. Tress, E. U. Mapesa, W. Kossack, W. K. Kipnusu, M. Reiche, and F. Kremer, Science **341**, 1371 (2013).

[30] F. Kremer, M. Tress, and E. U. Mapesa, Journal of Non-Crystalline Solids (2014).

[31] T. Koga, C. Li, M. Endoh, J. Koo, M. Rafailovich, S. Narayanan, D. Lee, L. Lurio, and S. Sinha, Physical review letters **104**, 066101 (2010).

[32] K. Johnston and V. Harmandaris, Soft Matter (2012).
[33] K. Johnston and V. Harmandaris, Macromolecules **46**, 5741 (2013).
[34] M. Solar, E. Mapesa, F. Kremer, K. Binder, and W. Paul, EPL (Europhysics Letters) **104**, 66004 (2013).
[35] H. J. Butt *et al.*, Macromolecules **47**, 8459 (2014).
[36] J. D. McCoy and J. G. Curro, The Journal of chemical physics **116**, 9154 (2002).
[37] C. Batistakis, A. V. Lyulin, and M. Michels, Macromolecules **45**, 7282 (2012).
[38] A. Papon, H. Montes, M. Hanafi, F. Lequeux, L. Guy, and K. Saalwächter, Physical review letters **108**, 065702 (2012).
[39] J. Wang, M. Tolan, O. Seeck, S. Sinha, O. Bahr, M. Rafailovich, and J. Sokolov, Physical Review Letters **83**, 564 (1999).
[40] S. Narayanan, D. R. Lee, R. S. Guico, S. K. Sinha, and J. Wang, Physical review letters **94**, 145504 (2005).
[41] Z. Jiang *et al.*, Physical Review Letters **98**, 227801 (2007).
[42] R. S. Guico, S. Narayanan, J. Wang, and K. R. Shull, Macromolecules **37**, 8357 (2004).
[43] D. Qi, Z. Fakhraai, and J. Forrest, Physical Review Letters **101**, 096101 (2008).
[44] D. Long and F. Lequeux, The European Physical Journal E **4**, 371 (2001).
[45] F. Varnik, J. Baschnagel, and K. Binder, Physical Review E **65**, 021507 (2002).
[46] A. Semenov, Physical Review Letters **80**, 1908 (1998).
[47] S. Kim and J. M. Torkelson, Macromolecules (2011).
[48] J. E. Pye and C. B. Roth, Physical Review Letters **107**, 235701 (2011).
[49] K. Paeng and M. Ediger, Macromolecules **44**, 7034 (2011).
[50] D. Qi, M. Ilton, and J. Forrest, The European Physical Journal E: Soft Matter and Biological Physics **34**, 1 (2011).
[51] L. Zhu, C. Brian, S. Swallen, P. Straus, M. Ediger, and L. Yu, Physical Review Letters **106**, 256103 (2011).
[52] C. R. Daley, Z. Fakhraai, M. D. Ediger, and J. A. Forrest, Soft Matter **8**, 2206 (2012).
[53] S. Mirigian and K. S. Schweizer, The Journal of chemical physics **141**, 161103 (2014).
[54] M. A. Plum, S. D. B. Vianna, A. Unger, R. F. Roskamp, H. J. Butt, B. Menges, and W. Steffen, Soft Matter **7**, 1501 (2011).
[55] M. A. Plum, B. Menges, G. Fytas, H.-J. Butt, and W. Steffen, Review of Scientific Instruments **82**, 015102 (2011).
[56] M. A. Plum, W. Steffen, G. Fytas, W. Knoll, and B. Menges, Optics Express **17**, 10364 (2009).
[57] S. D. B. Vianna, Ph.D. Thesis (2012).
[58] R. D. Priestley, D. Cangialosi, and S. Napolitano, Journal of Non-Crystalline Solids **407**, 288 (2015).
[59] H. Vogel, Phys. Z **22**, 645 (1921).
[60] G. S. Fulcher, Journal of the American Ceramic Society **8**, 339 (1925).
[61] G. Tammann and W. Hesse, Z. Anorg. Allg. Chem **156**, 245 (1926).
[62] C. Angell, MRS bulletin **33**, 544 (2008).
[63] A. J. Kovacs, in *Fortschritte der Hochpolymeren-Forschung* (Springer, 1964), pp. 394.
[64] F. Kremer and A. Schönhals, *Broadband dielectric spectroscopy* (Springer, 2003).
[65] G. Adam and J. H. Gibbs, The Journal of chemical physics **43**, 139 (1965).
[66] A. Saiter, E. Dargent, J. Saiter, and J. Grenet, Journal of non-crystalline solids **354**, 345 (2008).
[67] D. J. Plazek and K. L. Ngai, Macromolecules **24**, 1222 (1991).
[68] C. A. Solunov, European polymer journal **35**, 1543 (1999).
[69] C. Angell, Journal of Physics and Chemistry of Solids **49**, 863 (1988).
[70] H. Tanaka, The Journal of chemical physics **105**, 9375 (1996).
[71] J. A. Forrest and K. Dalnoki-Veress, ACS Macro Letters **3**, 310 (2014).

[72] J. A. Forrest, The Journal of Chemical Physics **139** (2013).
[73] J. D. van der Waals, J Stat Phys **20**, 200 (1979).
[74] M. Smoluchowski, Annalen der Physik **330**, 205 (1908).
[75] L. Mandelstam, Annalen der Physik **346**, 609 (1913).
[76] V. Levich and V. Krylov, Annual Review of Fluid Mechanics **1**, 293 (1969).
[77] F. Buff, R. Lovett, and F. Stillinger, Physical Review Letters **15**, 621 (1965).
[78] L. P. Kadanoff and P. C. Martin, Annals of Physics **24**, 419 (1963).
[79] A. Braslau, M. Deutsch, P. Pershan, A. Weiss, J. Als-Nielsen, and J. Bohr, Physical Review Letters **54**, 114 (1985).
[80] M. Sanyal, S. Sinha, K. Huang, and B. Ocko, Physical Review Letters **66**, 628 (1991).
[81] B. Ocko, X. Wu, E. Sirota, S. Sinha, and M. Deutsch, Physical Review Letters **72**, 242 (1994).
[82] T. Seydel, M. Tolan, B. Ocko, O. Seeck, R. Weber, E. DiMasi, and W. Press, Physical Review B **65**, 184207 (2002).
[83] S. K. Sinha, E. Sirota, S. Garoff, and H. Stanley, Physical Review B **38**, 2297 (1988).
[84] T. Seydel, A. Madsen, M. Tolan, G. Grübel, and W. Press, Physical Review B **63**, 073409 (2001).
[85] A. Madsen, J. Als-Nielsen, and G. Grübel, Physical Review Letters **90**, 085701 (2003).
[86] T. Seydel, A. Madsen, M. Sprung, M. Tolan, G. Grübel, and W. Press, Review of Scientific Instruments **74**, 4033 (2003).
[87] C. Gutt, T. Ghaderi, V. Chamard, A. Madsen, T. Seydel, M. Tolan, M. Sprung, G. Grübel, and S. Sinha, Physical Review Letters **91**, 179902 (2003).
[88] C. Gutt, T. Ghaderi, V. Chamard, A. Madsen, T. Seydel, M. Tolan, M. Sprung, G. Grübel, and S. Sinha, Physical Review Letters **91**, 76104 (2003).
[89] V. G. Levich, *Physicochemical hydrodynamics* (Prentice-Hall Englewood Cliffs, NJ, 1962), Vol. 689.
[90] G. R. Strobl, *The physics of polymers: concepts for understanding their structures and behavior* (Springer, 2007).
[91] N. Fatkullin, R. Kimmich, and M. Kroutieva, Journal of Experimental and Theoretical Physics **91**, 150 (2000).
[92] L. D. Landau and E. Lifshitz, Course of Theoretical Physics **3** (1986).
[93] L. Landau and E. Lifshitz, Course of Theoretical Physics, 227 (1987).
[94] F. Brochard-Wyart, P.-G. De Gennes, H. Hervert, and C. Redon, Langmuir **10**, 1566 (1994).
[95] A. Madsen, T. Seydel, M. Sprung, C. Gutt, M. Tolan, and G. Grübel, Physical Review Letters **92**, 96104 (2004).
[96] B. J. Berne and R. Pecora, *Dynamic light scattering: with applications to chemistry, biology, and physics* (Courier Dover Publications, 2000).
[97] L. Novotny and B. Hecht, *Principles of nano-optics* (Cambridge university press, 2012).
[98] H. Raether, *Surface plasmons on smooth surfaces* (Springer, 1988).
[99] W. Knoll, Annual Review of Physical Chemistry **49**, 569 (1998).
[100] E. Kretschmann and H. Raether, Zeitschrift Fuer Naturforschung, Teil A **23**, 2135 (1968).
[101] N. Bunjes, E. Schmidt, A. Jonczyk, F. Rippmann, D. Beyer, H. Ringsdorf, P. Gräber, W. Knoll, and R. Naumann, Langmuir **13**, 6188 (1997).
[102] A. Otto, Zeitschrift für Physik **216**, 398 (1968).
[103] I. Pockrand, Surface Science **72**, 577 (1978).
[104] E. T. Hoppe, I. Hopp, M. Port, B. Menges, and C. M. Papadakis, Colloid and Polymer Science **290**, 1731 (2012).
[105] J. C. Seferis, Polymer Handbook **4**, 571 (1999).
[106] L. Fetters, N. Hadjichristidis, J. Lindner, and J. Mays, Journal of physical and chemical reference data **23**, 619 (1994).

[107] N. Sultanova, S. Kasarova, and I. Nikolov, Acta Physica Polonica-Series A General Physics **19**, 585 (2009).
[108] T. Kaule *et al.*, ACS nano **7**, 748 (2012).
[109] Y. Zhang, J. Arfsten, S. A. Pihan, T. Kaule, R. Förch, and R. Berger, Journal of colloid and interface science **351**, 532 (2010).
[110] L.-Q. Chu, W. Knoll, and R. Förch, Langmuir **22**, 5548 (2006).
[111] M. A. Plum, Ph.D. Thesis (2010).
[112] F. Arecchi, M. Corti, V. Degiorgio, and S. Donati, Optics Communications **3**, 284 (1971).
[113] D. E. Koppel, The Journal of Chemical Physics **57**, 4814 (1972).
[114] C. Lindsey and G. Patterson, The Journal of Chemical Physics **73**, 3348 (1980).
[115] S. W. Provencher, Die Makromolekulare Chemie **180**, 201 (1979).
[116] S. W. Provencher, Computer Physics Communications **27**, 213 (1982).
[117] R. Kohlrausch, Annalen der Physik **167**, 179 (1854).
[118] G. Williams and D. C. Watts, Trans. Faraday Soc. **66**, 80 (1970).
[119] W. Brown, *Dynamic light scattering: the method and some applications* (Oxford University Press, USA, 1993), Vol. 49.
[120] D. W. Van Krevelen and K. Te Nijenhuis, *Properties of polymers: their correlation with chemical structure; their numerical estimation and prediction from additive group contributions* (Access Online via Elsevier, 2009).
[121] J. Gruver and G. Kraus, Journal of Polymer Science Part A: General Papers **2**, 797 (1964).
[122] A. Hofmann, A. Alegria, J. Colmenero, L. Willner, E. Buscaglia, and N. Hadjichristidis, Macromolecules **29**, 129 (1996).
[123] F.-Y. Lin and W. Steffen, The Journal of Chemical Physics **141**, 104903 (2014).
[124] M. J. Struglinski and W. W. Graessley, Macromolecules **18**, 2630 (1985).
[125] H. K. Nguyen, D. Wang, T. P. Russell, and K. Nakajima, Soft Matter (2014).
[126] G. Vinogradov, Y. G. Yanovskii, E. Borisenkova, B. Yarlykov, and G. Berezhnaya, Journal of Polymer Science Part A-2: Polymer Physics **10**, 1061 (1972).
[127] W. Rochefort, G. Smith, H. Rachapudy, V. Raju, and W. Graessley, Journal of Polymer Science: Polymer Physics Edition **17**, 1197 (1979).
[128] F. Stickel, E. W. Fischer, and R. Richert, The Journal of Chemical Physics **104**, 2043 (1996).
[129] J. N. Israelachvili, *Intermolecular and surface forces: revised third edition* (Academic press, 2011).
[130] P. S. Stephanou, C. Baig, G. Tsolou, V. G. Mavrantzas, and M. Kroeger, Journal of Chemical Physics **132**, 124904 (2010).
[131] C. D. Han and T. C. Yu, Journal of Applied Polymer Science **15**, 1163 (1971).
[132] P. J. Cole, R. F. Cook, and C. W. Macosko, Macromolecules **36**, 2808 (2003).
[133] R. Zhao and C. W. Macosko, Journal of Rheology (1978-present) **46**, 145 (2002).
[134] X. Hu, Z. Jiang, S. Narayanan, X. Jiao, A. R. Sandy, S. K. Sinha, L. B. Lurio, and J. Lal, Physical Review E **74**, 010602 (2006).
[135] C.-P. Klages, A. Dietz, T. Höing, R. Thyen, A. Weber, and P. Willich, Surface and Coatings Technology **80**, 121 (1996).
[136] H. Sirringhaus, T. Kawase, R. Friend, T. Shimoda, M. Inbasekaran, W. Wu, and E. Woo, Science **290**, 2123 (2000).
[137] J. Zhang, C. M. Li, M. B. Chan-Park, Q. Zhou, Y. Gan, F. Qin, B. Ong, and T. Chen, Applied physics letters **90**, 243502 (2007).
[138] M. F. Weber, C. A. Stover, L. R. Gilbert, T. J. Nevitt, and A. J. Ouderkirk, Science **287**, 2451 (2000).

[139] M. Ibanescu, Y. Fink, S. Fan, E. L. Thomas, and J. D. Joannopoulos, Science **289**, 415 (2000).
[140] H. Duran, A. Gitsas, G. Floudas, M. Mondeshki, M. Steinhart, and W. Knoll, Macromolecules **42**, 2881 (2009).
[141] H. Lee, A. Jamieson, and R. Simha, Macromolecules **12**, 329 (1979).
[142] J. Cavaille, C. Jourdan, J. Perez, L. Monnerie, and G. Johari, Journal of Polymer Science Part B: Polymer Physics **25**, 1235 (1987).
[143] Y. Suzuki, H. Duran, W. Akram, M. Steinhart, G. Floudas, and H.-J. Butt, Soft Matter **9**, 9189 (2013).
[144] C. B. Roth, K. L. McNerny, W. F. Jager, and J. M. Torkelson, Macromolecules **40**, 2568 (2007).
[145] N. Alves, G. Ribelles, G. Tejedor, and J. Mano, Macromolecules **37**, 3735 (2004).
[146] Z. Fakhraai and J. A. Forrest, Physical Review Letters **95**, 25701 (2005).
[147] M. Haghighi, M. A. Plum, G. Gantzounis, H.-J. Butt, W. Steffen, and G. Fytas, The Journal of Physical Chemistry C **117**, 8411 (2013).
[148] R. Böhmer, K. Ngai, C. Angell, and D. Plazek, The Journal of chemical physics **99**, 4201 (1993).
[149] M. L. Henle and A. J. Levine, Physical Review E **75**, 021604 (2007).
[150] J. R. Apel, An atlas of oceanic internal solitary waves (2002).
[151] C. Garrett and W. Munk, Annual Review of Fluid Mechanics **11**, 339 (1979).
[152] E. Hempel, G. Hempel, A. Hensel, C. Schick, and E. Donth, The Journal of Physical Chemistry B **104**, 2460 (2000).
[153] C. J. Ellison, M. K. Mundra, and J. M. Torkelson, Macromolecules **38**, 1767 (2005).
[154] E. U. Mapesa, M. Tress, G. Schulz, H. Huth, C. Schick, M. Reiche, and F. Kremer, Soft Matter **9**, 10592 (2013).
[155] P. M. Chaikin and T. C. Lubensky, *Principles of condensed matter physics* (Cambridge Univ Press, 2000), Vol. 1.
[156] Z. Nie, D. Fava, E. Kumacheva, S. Zou, G. C. Walker, and M. Rubinstein, Nature materials **6**, 609 (2007).
[157] C. J. Murphy, T. K. Sau, A. M. Gole, C. J. Orendorff, J. Gao, L. Gou, S. E. Hunyadi, and T. Li, The Journal of Physical Chemistry B **109**, 13857 (2005).
[158] K. Caswell, J. N. Wilson, U. H. Bunz, and C. J. Murphy, Journal of the American Chemical Society **125**, 13914 (2003).